NEWCASTLE UNIVERSITY

DOCTORAL THESIS

Computational Molecular Dynamics Study of Organic light Emitting Diodes

---

Author:
Yang CAO

Supervisor:
Dr. Thomas PENFOLD

A thesis submitted in fulfillment of the requirements for the degree of Doctor of Philosophy

on the

October 18, 2023

Declaration of Authorship

I, Yang CAO, declare that this thesis titled, "Computational Molecular Dynamics Study of Organic light Emitting Diodes" and the work presented in it are my own. I confirm that:

- This work was done wholly or mainly while in candidature for a research degree at this University.
- Where any part of this thesis has previously been submitted for a degree or any other qualification at this University or any other institution, this has been clearly stated.
- Where I have consulted the published work of others, this is always clearly attributed.
- Where I have quoted from the work of others, the source is always given. With the exception of such quotations, this thesis is entirely my own work.
- I have acknowledged all main sources of help.
- Where the thesis is based on work done by myself jointly with others, I have made clear exactly what was done by others and what I have contributed myself.

Signed:

Date:

NEWCASTLE UNIVERSITY

Abstract

Chemistry
School of Natural and Environmental Sciences

Doctor of Philosophy

Computational Molecular Dynamics Study of Organic light Emitting Diodes

by Yang CAO

Organic Light Emitting Diodes (OLEDs) have been the subject of an intense research effort aimed at improvement their performance resulting in the emergence as a key component in the lighting and display market. Indeed, in display field, OLEDs have registered 23.2% of the market share. Increasing demand for global OLEDs display market impels continued development and improvement to OLEDs performance and sustainability. This means higher efficiency, cheaper production and brighter materials with longer lifetimes are required. This makes the research about OLEDs important in both experimental and theoretical.

In the context of OLEDs, Thermally Activated delayed fluorescent (TADF) has emerged as a highly appealing mechanism for delivering highly-efficient third generation OLEDs. First generation OLEDs were based on the fluorescent molecules, which could not harvest non-radiative triplet states and therefore only achieve low internal quantum efficiency (IQE < 25%). The second generation OLEDs has overcome this using phosphorescence through intersystem crossing making it possible to achieve 100% IQE using heavy metals. But these are often rare and expensive.

In this thesis, a theoretical study of molecules exhibiting TADF via excited-state intramolecular proton transfer (ESIPT) is performed using quantum chemistry, quantum dynamics and molecular dynamics to understand the fundamental mechanism of triplet harvesting. Chapter 1 introduces the basic definitions and principal knowledge about OLEDs, TADF and ESIPT. Chapter 2 talked about he background theory and theoretical methods have been used in study, especially density functional theory and molecular dynamics. Chapter 3 discussed the ESIPT dynamics in OLEDs, resulted how the triplet harvesting plays the important role in OLEDs. Chapter 4 illustrates the examination of quantum tunneling and the impact of polarity on energy barriers. In Chapter 5, the role of excitation generation is also discussed.

Acknowledgements

I would like to thank Prof. Thomas Penfold for the opportunity of doing a Ph.D. in his brilliant group: Dr. Julien Eng, Dr Thomas Northey, Dr. Yveline Giret, Dr. Conor Rakine, Dr Stewart Thompson, Dr Jamie Gibson Josh Littlefair, Beth Laidlaw, Emanuele Falbo, Marwah Madkahli, Miriam Fsadni and Shawana Ahmad. Also, I am appreciate the examiners, Dr. Fabio Cucinotta and Dr. Rachel Crespo-Orero for their time.
Besides, I would like to thank my family to support me for this long journey, especially my wife, Di Ma.

Contents

List of Figures

List of Tables

List of Abbreviations

BOA	**B**onn **O**ppenheimer **A**pproximation
BLYP	**B**ecke **L**ee **Y**ang **P**arr
B3LYP	**B**ecke **3**-parameter **L**ee **Y**ang **P**arr
CFL	**C**ompact **F**luorescent **L**amp
CT	**C**harge **T**ransfer
ChElPG	**Ch**arges from **El**ectrostatic **P**otentials using a **G**rid-based
D-A	**D**onor-**A**cceptor
D-A-D	**D**onor-**A**cceptor-**D**onor
DF	**D**elayed **F**luorescence
DFT	**D**ensity **F**unctional **T**heory
ESIPT	**E**xcited **S**tate **I**ntramolecular **P**roton **T**ransfer
EXC	**EXC**itation
EQE	**E**xternal **Q**uantum **E**fficiency
EL	**E**lectro**L**uminescence
FGR	**F**ermi's **G**olden **R**ule
Full-CI	**Full** **C**onfiguration **I**nteraction
FWHM	**F**ull **W**idth **H**alf **M**aximum
GS	**G**round **S**tate
GSIPT	**G**round **S**tate **I**ntramolecular **P**roton **T**ransfer
GGA	**G**eneralised **G**radient **A**pproximation
HOMO	**H**ighest **O**ccupied **M**olecule **O**rbital
HF	**H**artree **F**ock
IQE	**I**nternal **Q**uantum **E**fficiency
ISC	**I**nter**S**ystem**C**rossing
IC	**I**nternal **C**onversion
LED	**L**ight **E**mitting **D**iodes
LUMO	**L**owest **U**noccupied **M**olecule **O**rbital
LDA	**L**ocal **D**ensity **A**pproximation
LR-TDDFT	**L**inear **R**esponse **T**ime **D**ependent **D**ensity **F**unctional **T**heory
MCTDH	**M**ulti **C**onfiguration **T**ime **D**ependent **H**artree
MD	**M**olecular **D**ynamics
MOM	**M**aximum **O**verlap **M**ethom
OLED	**O**rganic **L**ight **E**mitting **D**iodes
PLQY	**P**hoto **L**uminescence **Q**uantum **Y**ield
PBE	**P**erdew **B**urke **E**rnzerhof
PCM	**P**olarizable **C**ontinuum **M**odel
QM	**Q**uantum **M**echanics
rISC	**r**everse **I**nter**S**ystem**C**rossing
rIC	**r**everse **I**nternal **C**onversion
RG	**R**unge **G**ross

SPFs	**S**ingle **P**article **F**unctions
SS-PCM	**S**tate **S**pecific **P**olarizable **C**ontinuum **M**odel
SOCME	**S**pin **O**rbit **C**oupling **M**atrix **E**lements
TADF	**T**hermally **A**ctivated **D**elayed **f**fluorescent
TDSE	**T**ime **D**ependent **S**chrodinger **E**quation
TISE	**T**ime **I**ndependent **S**chrodinger **E**quation
TDDFT	**T**ime **D**ependent **D**ensity **F**unctional **T**heory
TDA	**T**amm **D**ancoff **A**pproximation
TTA	**T**riplet **T**riplet **A**nnihilation

Chapter 1

Introduction

The ability to generate and utilise light sits at the heart modern society. Everyday approximately 200Wm^{-2} of radiant energy in the form of natural light arrives from the sun, while artificial lighting and displays consume >20% of the electricity used worldwide. Converting light to energy, as performed by photovoltaics, is a major focus in our attempts to reduce reliance on unsustainable fuel sources, while the ability to generate light and display information is a hallmark of a developed society.[1]

In terms of the generation of light, history has witnessed significant development in artificial light sources (figure 1.1), including the development of the incandescent bulb, fluorescent lamps, halogen lights and light emitting diodes (LEDs) [2]. The incandescent light bulb has been used for more than hundred years as the main source of artificial lighting due to its low cost and continuous spectrum, arising because the source of the light is a metal filament (wire). Despite its advantages, its efficiency is only about 15%, as a significant amount of the energy used is lost as heat leading to a huge waste in energy[3]. The development of halogen light bulbs led to a significant reduction in energy consumption. Halogen bulbs work in a similar way to old-fashioned incandescent light bulbs, using a filament enclosed in halogen gas to produce light and like incandescent bulbs, they give off a warm, bright light and illuminate to full brightness as soon as the switch is turned on.

More recently, LEDs have replaced these aforementioned light source as they exhibit enhanced efficiency, durability and reliability[6]. In contrast to other bulbs, an LED bulb produces light by passing the electric current through a semiconducting material, the diode, which then emits photons (light) through the principle of electroluminescence [7]. LEDs consume 75% less power and last 25% longer than traditional bulbs[8, 9]. However, despite these advantages, there remain a number of limitations, including high costs associated with the sophisticated fabrication required due to the use of crystalline materials.

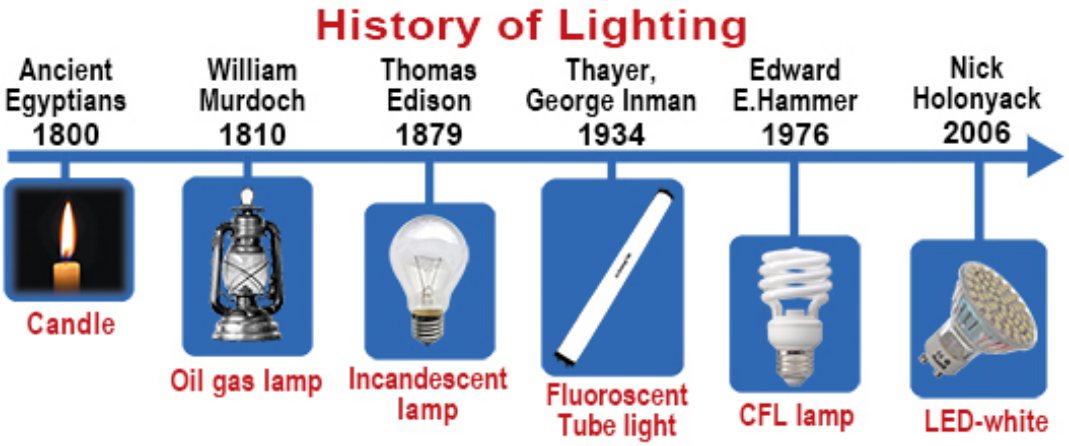

FIGURE 1.1: Brief history of lighting: Candle light by burning animal fat on reed had been used as the main light resource since 30BC in ancient Egypt, until 1810s, gas lighting was attributed to British inventor, William Murdoch; In 1840s, British scientist Warren De La Rue created the first electric light bulb, then it has been developed by Thomas Edison for commercial use in 1879; Fluorescent lamp was invented by George E. Inman and Richard N. Thayer in 1934. Edward E. Hammer has improved the fluorescent lighting to compact fluorescent lamp(CFL) in 1976, and it has taken up a huge share in daily lighting market until the white LED has been well-developed. Nick Holonyak, J. W. Allen and R. J. Cherry has established a complete fundamental for further LED development since 1962.[4, 5]

To overcome this, a significant amount of research effort has been placed on research organic light emitting diodes (OLEDs). OLEDs operate using the same concepts as LEDs (figure 1.2), but instead of being made from inorganic crystals, they are composed of flexible thin films of organic molecules. This removes the extreme conditions, such as low pressure and high temperature, required during the fabrication of LEDs, which have high energy demands. In contrast OLED fabrication uses techniques such as evaporation or solution processing, which can be done with ambient conditions.

The discovery of OLEDs can be traced back to 1963, when Martin Pope found electroluminescence in the organic material, anthracene[11]. But the first practical OLED device was achieved by Ching Wan Tang and Steven Van Slyke at Eastman Kodak in 1987 [12]. They used a two-layer structure with separated hole and electron transport layers to allow recombination in the organic emission layer with a low voltages and ideal efficiency. A key challenge in OLEDs is that the communication between the singlet and triplet manifolds is weak, usually making the conversion between the singlet and triplet states in organic materials slow. This is crucial in an operating OLED device because in contrast to the selection rules associated with photoexcitation, the process of exciton generation on the emitter in OLEDS (electrical

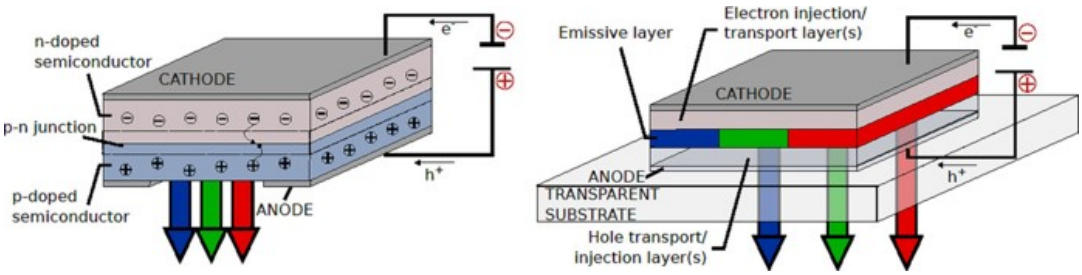

FIGURE 1.2: LED(left) and OLED(right) could be briefly represented as this figure. LED devices light is from the P-N junction after the hole pass through the P-doped semiconductor and electrons through the N-doped semiconductor. Different with LED, OLEDs emit because the hole-electron recombined in the emissive layer, and different organic molecules could be used to make the device perform better. Figure taken from reference [10]

excitation) leads to a 25:75 singlet to triplet population ratio due to spin statistics of charge recombination. Consequently when adopting a typical organic molecule, as in the case of first generation fluorescent OLEDs, only 25% of the generated excited states will be harvested.

After 1987, Kodak initially focused on fluorescence materials for OLED devices, but this has limited the efficiency, as the triplet excitons are lost non-radiatively to heat. Ten years later, the first phosphorescence OLED device were introduced by Thompson, Forrest and et al.[13], which made it possible to harvest all of the excitons generated leading to higher efficiencies($\geq$90%). In 2012, pure organic OLEDs based upon thermally activated delayed fluorescence were designed by the Adachi group at Kyushu university.[14] In the following sections the harvesting mechanism of OLEDs will be discussed in more detail.

OLEDs operate by electroluminescence, which is the phenomenon of light emission through the application of an electric current. It occurs when electrons and holes (*i.e.*, positive charge carriers) are injected into a material, and the energy from the electric current excites the electrons to a higher energy level. When the electrons relax back to their original energy levels, they emit light as a result. [15] The internal quantum efficiency (IQE) of and OLED, *i.e.* ignoring losses associated with extracting light from the device, is defined:

$$IQE = \gamma \times \eta_{ST} \times \phi_{PL} \tag{1.1}$$

Here γ is the charge balance factor, or the fraction of injected carriers that

form excitons, η_{ST} is the fraction of spin-allowed excitons, ϕ_{PL} is the photoluminescence quantum yield (PLQY).

In a well-optimised device with perfectly matched electron and hole currents, γ can reach near unity. It is also possible to desgin molecules close to unity PLQY. However, η_{ST} can vary depending on the type of emitter used in the device, as shown in figure1.3. In the first generation, OLEDs were based upon fluorescent emitters. In this case, only the singlet states are harvested, while the triplet excitons are lost nonradiatively as heat. This limits the IQE to 25%, and although triplet-triplet annihilation (TTA) is used in OLEDs to improve their efficiency by harvesting some of the otherwise unused triplet excitons and converting them into singlet excitons that can emit light. This process allows for more efficient use of energy in these devices, leading to brighter and more energy-efficient displays and lighting. But TTA can be exploited to increase this to $\sim$60%, this still remains some distance from 100%.

The 2^{nd} generation of OLEDs were based upon phosphorescent emitters. While these exploit heavy elements to activate spin-orbit coupling enabling the triplet states to become radiative, it is only the very heavy and expensive metals, such as Ir and Pt that have been shown to exhibit large enough spin-orbit coupling. Finally, thermally activated delayed fluorescence (TADF), as the 3^{rd} generation OLED, has emerged as a highly promising mechanism by harvesting triplet states and therefore has gained significant research interest for applications in OLEDs. The advantage of TADF is that by engineering the singlet and triplet states to be sufficiently close in energy, *i.e.* close to thermal energy, it is possible to harvest both singlet states and triplet states through prompt and delayed fluorescence, respectively. The latter is thermally activated as the triplet state is almost always lower than the singlet state. In this case the IQE will be able to close to 100%.[16, 17, 18]

The requirement to engineer a small energy gap (ΔE_{ST}) between the lowest singlet (S_1) and triplet (T_1) states is the most essential condition for highly efficient TADF molecules. This is because the rate of TADF can be approximated as:

$$k_{TADF} = \frac{1}{3} k_F \exp \frac{-\Delta E_{ST}}{k_B T} \tag{1.2}$$

where k_F is the rate of fluorescence. To obtain a small ΔE_{ST}, most works have focused upon a Donor-Acceptor (D-A) or Donor-Acceptor-Donor (D-A-D) systems such as those in Figure 1.4 [20], as the CT character of the excited state minimise the exchange splitting between the singlet and triplet states. However, more recently the excited state intra-molecular Proton Transfer

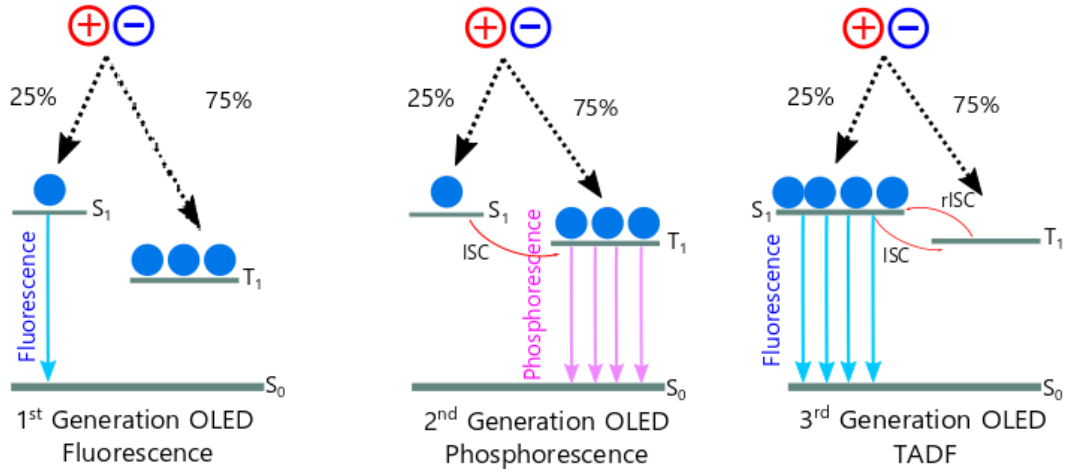

FIGURE 1.3: The operating principle of 1, 2 and 3 generation of OLEDs [19]

(ESIPT) mechanism has been used to separate the frontier orbitals and minimise ΔE_{ST} to achieve TADF. This is one of the key focuses of the present thesis.

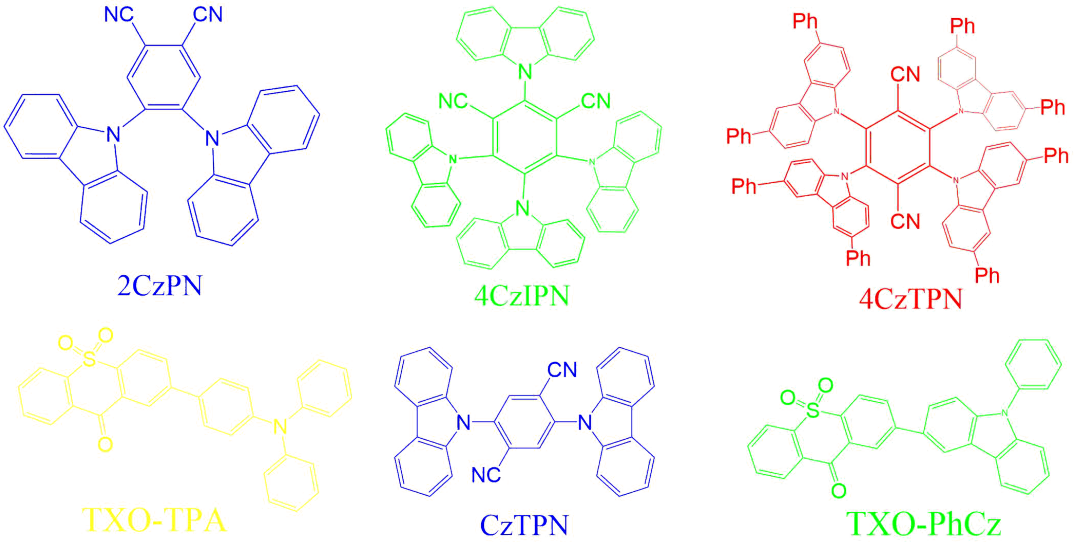

FIGURE 1.4: Molecular Structures of typical TADF based red, green, blue and yellow OLEDs[20]

To understand and design materials operating in excited states, we need to obtain a detail understanding of all of the competing processes. Processes occurring in electronically excited states are often very different to those in ground states because excited states tend to be highly non-equilibrium. This thesis will focus on trying to understand the excited state processes during TADF especially for ESIPT emitters.

1.1 Excited State Processes

When a molecule in its electronic ground state absorbs a photon, it can become promoted into an electronically excited state. Crucially, this often generates a highly non-equilibrium state and understanding the proceeding relaxation pathways is complicated by the often fast dynamics and many competing processes, which includes radiative decay such as fluorescence and phosphorescence, and non-radiative processes such internal conversion and intersystem crossings. Deeply understanding all of these processes will help us understand excited state mechanisms and develop new high performing materials.

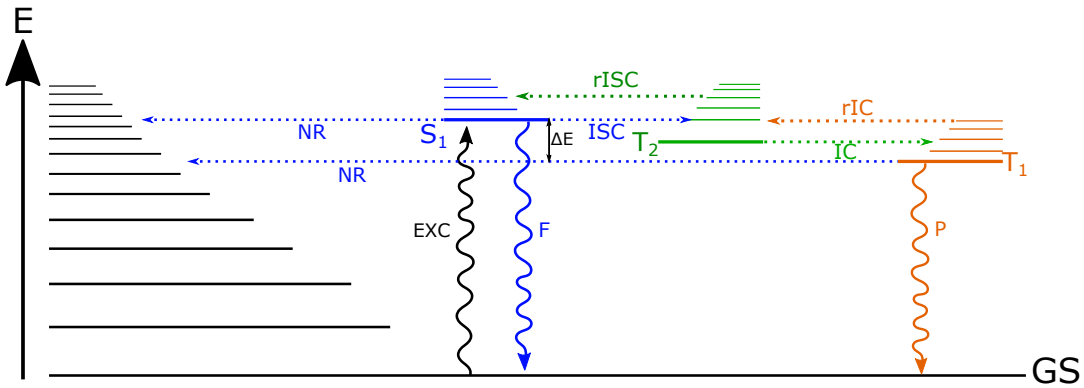

FIGURE 1.5: Jablonski Diagram for the photoexciation(EXC), ground state(GS), the first singlet state(S_1), the first triplet state(T_1), the second triplet state(T_2) with their vibrational states and the excitaion and relaxation process (Fluorescence(F), Phosphorescence(P)) and non-radiative processes: Intersystem Crossing(ISC), Internal Conversion(IC), Reverse ISC(rISC) and Reverse IC(rIC).

Figure1.5 shows the simplest representation of the excited state processes, a Jablonski diagram, with the aforementioned processes labelled. Radiative processes (Fluorescence and phosphorescence) and non-radiative processes (ISC,rISC, IC, rIC) are presented by the wavy arrows and dash arrows, respectively.

While the Jablonski diagram represents a convenient schematic for excited state processes, its major limitations is that it completely ignores the effect of structure on the the energy of the states. After excitation, the molecule will exhibit a new electronic structure. This will often drive geometry changes in the molecule and result in different ordering of the energy states shown in Figure1.5. This can be captured using potential energy curves along the most important degrees of freedom, *i.e.* those which are expected to show the

largest change in the electronically excited states of interest. These can give a more detailed perspective of how excited state processes are likely to evolve, but in cases where there are many competing excited state processes in multiple degrees of freedom, potential energy curves will give an incomplete or maybe even biased perspective.

Rates of competing excited state processes can be used to provide a more complete insight into the nature of the excited state processes. These can be computed using a Fermi's golden rule (FGR) approach[21] or by incorporating dynamics by providing a solution to the time-dependent schrödinger equation (TDSE)[22] or related approximations of it[23]. Both of these approaches, which are described in detail in the theory chapter will be used in this thesis.

1.2 Thermally activated delayed fluorescence

TADF has been one of the most useful methods to harvest triplet states in non-metal organic materials for design in OLED in recent decades. Molecular fluorescence is a two-step process which starting from absorption and generation of electronically excited state. By ignoring all other possible pathways, decays radiatively into the electronic ground state. This has been defined as prompt fluorescence. Conversely, fluorescence may be involved through a complex path involving competing excited state processes and the triplet manifold.. In this situation, intersystem crossing (ISC) makes the singlet excited state decay into triplet states. If the phosphorescence and non-radiative decay of the triplet state is slow and the energy gap (ΔE) is small enough (normally Δ E < 0.2 Ev), then rISC will allow it relax back to singlet then emission, [24] which is known as delayed fluorescence (DF). [25] Non-radiative decay is a process by which an excited state of a system relaxes to a lower energy state without emitting a photon. In LED, it determines the efficiency of devices that rely on radiative processes and it could be decreased by using the high-quality materials with low defect densities. [26]

The first reported the DF was by Perrin et al.[27] in solid uranyl salts in 1929 and in 1941 Lewis et al.[28] has found more details in rigid media . In later 1961, Parker et al. [29] had researched the DF by using Eosin. It had been named as E-type DF until 2012, Adachi and his co-workers [14] exploited the rISC of DF and name it as thermally activated delayed fluorescence (TADF), to harvest the triplet state energy from electric excited OLED molecule and

firstly indicate the organic molecules could produce high efficiency electroluminescence. This work has helped lots of researchers to understand and develop the photophysics of TADF.[30, 31, 32]

The thermal equilibrium between singlet and triplet state is used to describe the TADF accordingly. Parkr et al. [29]have proposed this firstly, and Kirchhoff et al. [33] reinforced this in $Cu(I)$ systems in 1983. The rate of TADF can be described as equation 1.2.

TADF processed by rISC from triplet to singlet state and followed by fluorescence from signlet excited state to ground state. As the ISC and rISC processes are in the thermal equilibrium, so this ratio could be replaced by the ΔE with temperature (T), where the k_B is the Boltzmann's constant and the $(1/3)$ pre-exponential is the density ratio of states between singlet and triplet. Parker's work has assumed that the $k_F \ll k_{rISC}$ and based on this, there are two ways to allow higher efficiency TADF by 1) smaller ΔE and 2) making the molecule rigid to decrease nonradiactive decay [24].

Within this thermal equilibrium model, the focus is upon minimising the energy gap between the lowest singlet and triplet states. For this there are three components considered during calculating the lowest energy of singlet (E_{S_1})and triplet excited states (E_{T_1}): (I) the orbital energy (E_O), (II) the electron repulsion energy (K), (III) the exchange energy (J). According the different spin arrangement of singlet and triplet excited states, the singlet excited states energy (E_{S_1}), the triplet excited states energy (E_{T_1}) and the energy gap between them are shown as:[34, 35]

$$E_{S_1} = E_O + K + J \tag{1.3}$$

$$E_{T_1} = E_O + K - J \tag{1.4}$$

$$\Delta E_{ST} = E_{S_1} - E_{T_1} = 2J \tag{1.5}$$

Based on equation 1.5, it is clear that to minimize the energy gap demands to minimize the exchange energy J, which is calculated by:

$$J = \iint \phi(r_1)\psi(r_2)\left(\frac{e^2}{r_1 - r_2}\right)\phi(r_2)\psi(r_1)dr_1dr_2 \tag{1.6}$$

Here, ϕ and ψ represent the electron densities at the positions r_1 and r_2, and $r_1 - r_2$ is the distance between the two points. It should also be stressed that the above analysis is only valid for states of the same character. e is

the electron charge. According to equation 1.6, the J value could be minimized by decreasing the overlap between highest occupied molecular orbital (HOMO) and lowest unoccupied molecular orbital(LUMO), [34] which is achieved using charge-transfer type molecules.

It should be stress that the thermal equilibrium picture for TADF assume the rate of intersystem crossing is much greater than the fluorescence rate. However this often needs to be broken to develop high performance emitters. There is a huge literature on new TADF emitters which have largely focused upon large-scale synthetic programs aimed at developing and then exploiting structure–property relationships.

The other thing could help us understand the excitation process is the El-Sayed rule. In the rule, organic molecules that have an even number of electrons in their ground state (a closed-shell configuration) are more likely to undergo an excitation to a singlet state (S1) upon absorbing light. Singlet states have paired electrons with opposite spins, or organic molecules that have an odd number of electrons in their ground state (an open-shell or diradical configuration) are more likely to undergo an excitation to a triplet state (T1) upon absorbing light. Triplet states have unpaired electrons with the same spin. The El-Sayed rule is a useful tool in understanding the electronic transitions and helpful to predict the excited states is singlet or triplet state based on the molecular characteristics.

Early studies into TADF assumed that it was between ^{1}CT and ^{3}CT states where the TADF occurred, however, this is not a complete picture. First of all, because of any spin changes must be accompanied by a corresponding change in angular momentum to allow a conserved total angular momentum, so the SOC between two states of the same characteristic is prohibited.[36] If the state has the same characteristics, it cannot meet the requirements of angular momentum changing. [37] Secondly, they cannot have the same character as the environment can singly tune the states in TADF, which has been indicated by Monkman and co-workers[38, 39]. Later Ward et al. [40] found that different D-A-D molecules with similar ΔE exhibit large variations in k_{rISC} and the emission can be changed from TADF to phosphorescence by locking the D and A group's motion. Their work has indicated TADF relies on molecular vibrations and is dynamic in nature.

1.3 Excited States Intra-molecular Proton Transfer

The excited-state intramolecular proton transfer (ESIPT) phenomenon is nowadays widely acknowledged to play a crucial role in many photobiological and photochemical processes. The first observation of ESIPT was found by Weller in 1950s on salicylic acid study.[41] In 1974, Frolov has been the first one to report that there were two intense fluorescence bands (400nm and 500nm) for the 3-hydroxyflavone in ethanol at 77K arising from the enol and keto forms.[42]

ESIPT occurs during the photoexcitation of a two-part molecular system, one side is connected by intramolecular hydrogen bonds, and the other side is connected to a network of electronic conjugated covalent bonds, as shown in Figure 1.6. The reaction occurs in an excited state, usually characterized by the distance between the proton donor (D) atom (most commonly oxygen or nitrogen[43, 44, 45]) and the transferred proton. The proton acceptor (A) part is composed of another negatively charged center, usually composed of a carbonyl group or imine group[46, 47], and the hydrogen atom in the one of amine group hydrogen bonded to the neighboring oxygen in the ketone group. Photoexcitation drives the hydrogen atom to the oxygen atom becoming as hydroxy group, then hydrogen bonded to the nitrogen atom in the imine group. For the ESIPT process to be effective, the excited state should exhibit greater basicity than the proton donor. After the proton transfer, the system will undergo further electronic relaxation, essentially radiative or non-radiative. In the former case, the strong red-shifted fluorescence characteristic is now considered as a sign of ESIPT. The latter case requires the existence of independent non-radiative inactivated channels, for example caused by cis/trans isomerization reactions.[48] Although the ultrafast ESIPT process is often reported to have ballistic properties, it may also involve non-adiabatic transitions/inter-system crossing energy barriers or involving different electronic states. Similarly, after relaxing to the basically electronic state, the system may reach a local PT minimum, or it may spontaneously undergo a reverse transfer to the initial D-H bond isomer. This closure of the final reaction cycle is sometimes referred to as ground state intramolecular proton transfer (GSIPT).[49]

Molecules with ESIPT have been used in many applications, including the optical storage, switches[50], laser dyes[51] and florescence probes.[52, 53]. However, recently Mamada et al. [54] have recently investigated the possibility for triplet harvesting by ESIPT. Here the transfer of the proton

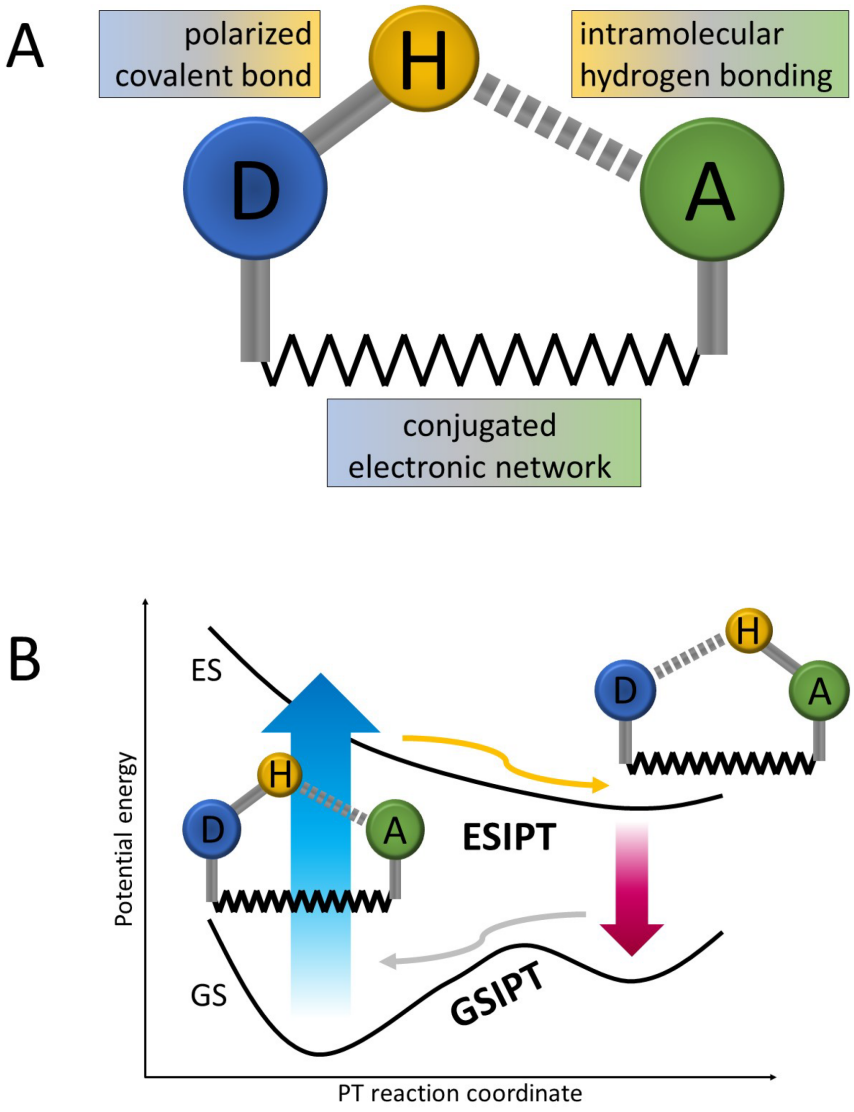

FIGURE 1.6: ESIPT mechanism: A) initial ESIPT system atom arrangement, B) classic potential energy landscape with ESIPT. (D: Proton Donor; A: Proton Acceptor; GS: Ground state; ES: Excited State; Blue arrow: Initial photoabsorption; Red Arrow: Stokes-Shifted Fluorescence)[49]

(carrying by a hydrogen atom) covalently bonded to one heteroatom to a second on the same molecule leads to another tautomerization from keto to enol, and in enol form, the molecule has less overlap between the HOMO and LUMO, which reduces the energy gap between the low lying excited states.

This effect of ESIPT is well documented,[55] and the solvatochromism, indicative of a state of CT characteristics, in the emission of such materials has widely been reported.[56, 57] Indeed, TADF from ESIPT materials in solution has previously been reported by Park et al.[58] However, importantly in this case the large amplitude motions of the molecules were required to enable ESIPT and therefore TADF. While this does not affect the solution phase measurements of Park et al.,[58] it represents a severe limitation for triplet harvesting in OLEDs, which exist in the solid state,[59] therefore constraining larger amplitude motions required. Importantly, the molecule, triquinolonobenzene (TQB,3.1) developed by Mamada et al. demonstrated ESIPT for a rigid structure, and demonstrated it was able to harvest a large contribution of the triplets states by achieve up to 14% external quantum efficiency (EQE) when integrated into an OLED.

1.4 Generation of the Excited State and the Importance of Initial Conditions

In recent years, a lot of important research has focused on the understanding of the complex photophysics of TADF materials[32], which has required a large number of different spectroscopic techniques to characterize the triplet harvesting mechanism and determine the photophysical parameters. However, due to the different excitation mechanism, under the electrical excitation of the OLED, the properties of the strong delayed fluorescence observed in the photophysical characterization are not necessarily the same.

In addition, after absorbing light, the molecule will be transferred to an electronically excited state, which depends on the intensity and length of the excitation.[60, 61] It is generally assumed that this transition is vertical to the ground state nuclear configuration. The molecule and the transition probability are controlled by the strength of the transition dipole moment.

Although the probability of forming an excited state under photoexcitation can be understood from the relative intensity of the state transition dipole moment within the excitation pulse energy window, it is different for the electrical excitation of OLEDs, as shown in the figure1.3. Except for the

ratio of spin states formed by charge recombination spin statistics[62], there isn't too much known about the properties of the excited states formed, such as geometry and contributions of higher lying singlet, triplet states. Most importantly the Franck-Condon principle is no longer valid in the case of charge recombination.[10]

To understand the mechanism, we assumed two different scenarios, and designed related simulations to verify the process. The results and simulations will reveal in this thesis.

1.5 Thesis outline

The primary goal of this thesis is to comprehend the excited state processes involved in TADF and their impact on the performance of OLEDs. This work is comprised of five chapters, including this introduction. The following chapter 2 explores the background and methodology used in the research. Chapter 3 presents results on the study of triplet harvesting dynamics and the mechanisms behind it. The results of the quantum tunnelling examination are presented in Chapter 4. Chapter 5 delves into the analysis of exciton generation in OLEDs, examining both the first and second charge transfers during TADF OLED molecule formation through molecular dynamics results. Through these chapters, the mechanism of TADF and ESIPT, as well as the exciton formation process, can be understood.

Chapter 2

Background Theory and Methodology

2.1 Time-dependent Schrödinger Equation

The time-dependent Schrödinger equation (TDSE) is a differential equation that describes the time-evolution of a non-relativistic quantum system, taking into account the wave-particle duality behaviour of matter. The central equation is an eigenvalue problem using a Hamiltonian, which described the total energy of a quantum system, including kinetic (T) and potential (V) energy terms. Schrödinger Equation (1926) was developed by Austrian physicist Erwin Schrödinger (1887 - 1961) [63] and can be written:

$$i\hbar\frac{\partial\Psi(r,t)}{\partial t} = \hat{H}\Psi(r,t) \tag{2.1}$$

Here the wavefunction, Ψ is propagated under the influence of Hamiltonian operator given by:

$$\hat{H} = -\frac{\hbar^2}{2m}\nabla^2 + V(r) \tag{2.2}$$

m is the particle's mass, and V is the potential of the environment in which it resides and $\hbar$ (the decreased Planck constant) ($\hbar = \frac{h}{2\pi}$). The solution of the TDSE is a superposition of eigenstates, called a wavepacket which will evolve with time over the potential energy (V). The potential, V, which is generally time-independent is calculated and modelled using quantum chemistry calculations and solutions to the time-independent Schrödinger equation, which focuses upon the electronic problem. But the TDS is only applicable under the following conditions: 1). Non-relativistic particle motion; 2). The system's Hamiltonian is time-dependent; 3). The potential energy V is well defined and continuous in space; 4). The wavefunction is single valued and normalizable.

One method of addressing the TDSE is to simplify it using the separation of the variables approach. This is done by expressing the total wavefunction as a product of spatial (r) and temporal (t) components:

$$\Psi(r,t) = \psi(r)T(t) \tag{2.3}$$

Inserting this into the TDSE and dividing through by the overall wavefunction leads to two equations:

$$i\hbar\frac{\partial T(t)}{\partial t} = \hat{H}T(t) \tag{2.4}$$

$$\hat{H}\psi(r) = E\psi(r) \tag{2.5}$$

The latter is the time-independent Schrödinger equation (TISE), which can be used to calculate the potential energy of the system. The former equation can be used to develop the solution of the time-evolution in the form:

$$T(t) = T_0 \exp -iEt/\hbar \tag{2.6}$$

T_0 is the initial wavefunction.

2.2 Born-Oppenheimer Approximation

For a molecular system, the Hamiltonian containing kinetic and potential terms for the electrons and nuclei and is expressed as:

$$H = T_e + T_N + V_e + V_N + V_{eN} \tag{2.7}$$

Expanding each term, this equation becomes:

$$H = \sum_i \frac{-\hbar^2}{2m}\nabla_i^2 + \sum_i \frac{-\hbar^2}{2M}\nabla_i^2 + \sum_{j>i}\frac{e^2}{|r_i - r_j|} + \sum_{j>i}\frac{Z_i Z_j e^2}{|R_i - R_j|} - \sum_{ij}\frac{Z_j e^2}{|r_i - R_j|} \tag{2.8}$$

T_e and T_N are the kinetic energies of the electrons and nuclei, V_e and V_N are the potential energies of the electrons and nuclei and V_{eN} is the electronic-nuclear interaction. The above shows that even for relatively small systems, the number of terms required becomes quickly very large and therefore approximations need to be made.

The Born-Oppenheimer approximation (BOA), which is the cornerstone of quantum chemistry, is used to separate the electronic and nuclear degrees

of freedom into two problems meaning each one can be treated separately. This is achieved by recognising that the nucleus has a substantially more mass than an electron (more than 1000 times). As a result of this disparity, the nuclei travel at a significantly slower rate than the electrons, which means we can consider that the positions of the electrons to adapt immediately to any changes in nuclear geometry.

The generation of the BOA can be shown by writing the full wavefunction as the product of the electronic and nuclear wavefunctions:

$$\Psi(\mathbf{r}) = \sum_{i}^{\infty} \psi(\mathbf{r};\mathbf{R})\chi_i(\mathbf{R},t) \tag{2.9}$$

where the $\psi(\mathbf{r};\mathbf{R})$ stands for the adiabatic electronic wavefunctions and $\chi_i(\mathbf{R},t)$ stands for the nuclear states, where, the r and R stand for the electron and nuclei position. This is often referred to as the Born-Huang representation. Importantly, the Born-Huang *ansatz* supports the creation of a picture of a time-dependent nuclear wavepacket evolving over an excited-state potential energy surface generated by the electrons. By substituting this expression in into the TDSE and multiplying through by ψ^*, one can obtain an expression for the time-dependent nuclear wavefunction in an arbitrary electronic state, j:

$$i\hbar\frac{\partial\chi_j(\mathbf{R},t)}{\partial t} = \left[-\sum_{\gamma}\hbar^2 2M_\gamma + E_j^{el}\right]\chi_j(\mathbf{R},t) + \sum_{i}^{\infty}\mathcal{F}_{ij}(\mathbf{R})\chi_i(\mathbf{R},t) \tag{2.10}$$

$\mathcal{F}_{ij}$ is the only term which prevents separation of nuclear and electronic degrees of freedom and therefore neglecting it corresponds to the Born-Oppenheimer approximation. Physically, $\mathcal{F}_{ij}$ allows excited-state population to transfer between different excited states, and is written:

$$\begin{aligned}\mathcal{F}_{ij}(\mathbf{R}) &= \int d\mathbf{r}\psi_j^*(\mathbf{r};\mathbf{R})\left[-\textstyle\sum_\gamma \frac{\hbar^2}{2M_\gamma}\right]\psi_i(\mathbf{r};\mathbf{R}) \\ &+ \textstyle\sum_\gamma 1M_\gamma\left\{\int d\mathbf{r}\psi_j^*(\mathbf{r};\mathbf{R})[-i\hbar\nabla]\psi_i(\mathbf{r};\mathbf{R})\right\}[-i\hbar\nabla]\end{aligned} \tag{2.11}$$

Where i and j are electronically excited states and γ are the different nuclei. While the Born-Oppenheimer approximation is fundamental in many areas of chemistry, in cases where rapid nuclear motion is expect - such as highly non-equilibrium situations, this breaks down, making it impossible to neglect the coupling between the electronic and nuclear degrees of freedom.

2.3 Adiabatic and Diabatic Representations

Quantum chemistry within the Born-Oppenheimer approximation are the default for most simulations. Here, the nuclei are assumed to be at rest and fixed in a certain configuration, eliminating the need for nuclear kinetic energy. Solving the electronic Schrödinger equation for excited states at this configuration yields a series of energy and repeating this over and over again yields electronic energies as a function of the nuclear coordinates. This kind of potential energy surface for different molecular geometries is known as an adiabatic potential energy. In these cases the character of the state depends on the nuclear coordinates and all coupling between different states is neglected.

However, if the kinetic energy of the nuclei is large, the non-adiabatic coupling , the coupling between different electronic states of a molecule, cannot be neglected. The non-adiabatic couplings describe the transition between electronic states that are not adiabatic, meaning that the electronic wavefunction is not an eigenstate of the Hamiltonian. The magnitude of the non-adiabatic couplings determines the likelihood of transitions between electronic states, and is a key quantity in the description of electronic processes in molecules. These terms can be added to correct the potential energy surfaces, but this gives rise to another challenge, which is clear if the first-order nonadiabatic coupling operators are written as expressed:

$$\begin{aligned} \mathcal{F}_{ij} &= \langle \psi_i | \nabla \psi_j \rangle \\ &= \frac{\langle \psi_i | \nabla \hat{\mathcal{H}}_0 | \psi_j \rangle}{E_j - E_i} \end{aligned} \tag{2.12}$$

where ψ_i are the electronic basis functions that are solutions of the time-independent electronic Schrödinger equation and E_i the corresponding energies. Here it is clear that within the adiabatic basis used by quantum chemistry methods, the nonadiabatic coupling diverges near intersections of the two coupled states, as the nonadiabatic coupling clearly exhibits an inverse dependence on the energy gap between surfaces. As this gap narrows, the coupling increases, but, if two surfaces become degenerate, the coupling becomes infinite. This creates a significant challenge for computational methods seeking to study the nonadiabatic dynamics.

To avoid this problem it is desirable to transform the adiabatic states

into the so-called (quasi)-diabatic representation. By construction, the adiabatic representation (See Figure 2.1) shows a set of energy-ordered potentials and non-local couplings elements via nuclear momentum-like operators. In contrast, in the diabatic representation potentials are connected to electronic configuration and the couplings are provided by local multiplicative Q-dependent potential-like operators. Importantly, the surfaces in the diabatic picture are smooth, as the nuclear kinetic energy coupling terms are minimized via translation from the adiabatic to diabatic representation.

Diabatic states and adiabatic states are two ways of representing the electronic states of a molecule in quantum mechanics. Diabatic states are a representation of electronic states where the wavefunction is not an eigenstate of the Hamiltonian, meaning that the wavefunction changes as the nuclei in the molecule move. Adiabatic states are a representation of electronic states where the wavefunction is an eigenstate of the Hamiltonian, meaning that the wavefunction does not change as the nuclei in the molecule move. Instead, the electronic energy changes as the nuclei move. Due to the fact that,

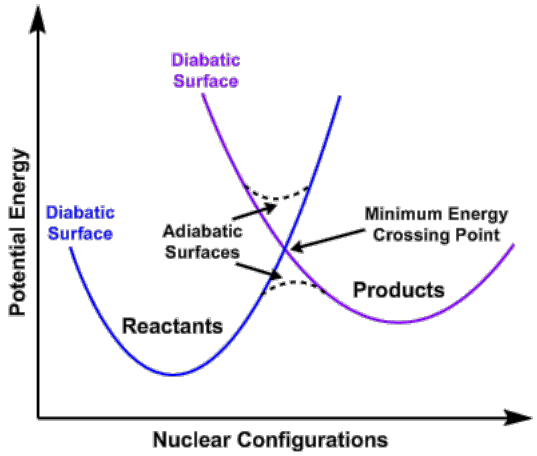

FIGURE 2.1: Schematic of adiabatic and diabatic potential surfaces.

in general, there is no general diabatic transformation, the kinetic couplings terms cannot be reduced to completely to zero, hence the use of the (quasi)-diabatic expression. This is why it is often difficult to get the correct diabatic potentials and approximations have to be made. For a given set of adiabatic potential energy surfaces, diabatisation can be broadly classified into three groups: property-based, by *ansatz* and wave-function based. [64, 65, 66]. Property based methods[67, 68, 69, 70, 71] approximate the diabatic states using observables such as transition dipole moment and change in molecular dipole moment. By *ansatz* methods, which we adopt and will be described in

the next section, define the diabatic states at a certain geometry, $\mathbf{Q_0}$, the non-adiabatic coupling matrix and then perform a Taylor expansion around this point. The expansion is parameterised through fitting which is inexpensive, however the disadvantage is that in the absence of high molecular symmetry there might be some ambiguity in the diabatisation because only adiabatic electronic energies are used and no information about the electronic wave-functions is utilised. Finally, wavefunction methods explicitly calculate the coupling elements and then transform them into states which minimise the coupling and preserve the character of the diabats.

2.4 Vibronic Coupling Hamiltonian

For a molecular system including the vibronic coupling, it's important to describe the system with the appropriate Hamiltonian, and as discussed above we will adopt a diabatic Hamiltonian. To effectively describe an accurate model, we will adopt the so called vibronic coupling Hamiltonian pioneers by Domcke and co-workers [72]

The starting point with this Hamiltonian is with a sum of the zeroth order Hamiltonian ($\mathbf{H^{(0)}}$) which is then expanded as a Taylor series around $\mathbf{Q_0}$, usually the Franck-Condon geometry :

$$\mathbf{H} = \mathbf{H^{(0)}} + \mathbf{W^{(0)}} + \mathbf{W^{(1)}} + ... \tag{2.13}$$

The zeroth order term could be explained as the harmonic oscillator approximation of ground state:

$$H^{(0)} = \sum_{\alpha} \frac{\omega_\alpha}{2} (\frac{\partial^2}{\partial Q_\alpha^2} + Q_\alpha^2) \tag{2.14}$$

where, the ω_α is the vibrational frequencies. The adiabatic state energies at Q_0 has been contained in the zeroth order coupling matrix. The adiabatic potential surfaces and the diabatic surfaces at this point are equal, so $\mathbf{W^{(0)}}$ is diagonal and could be expressed as:

$$W_{ij}^0 = \sum_{\alpha} \langle \Phi_i(\mathbf{Q_0}) | \hat{H}_{el} | \Phi_j(\mathbf{Q_0}) \rangle \tag{2.15}$$

where, the $\hat{H}_{el}$ is the standard clamped nucleus electronic Hamiltonian and Φ is the diabatic electronic functions. Then, the first order linear of coupling

matrix elements:

$$W_{ij}^{1} = \sum_{\alpha} \langle \Phi_i(\mathbf{Q_0}) | \frac{\partial \hat{H}_{el}}{\partial Q_\alpha} | \Phi_j(\mathbf{Q_0}) \rangle Q_\alpha \tag{2.16}$$

where, the on-diagonal and off-diagonal terms could be written as:

$$W_{ii}^{1} = \sum_{\alpha} \kappa_\alpha^{(i)} Q_\alpha \tag{2.17}$$

$$W_{ij}^{1} = \sum_{\alpha} \lambda_\alpha^{(i,j)} Q_\alpha \tag{2.18}$$

where, the κ and λ stand for the expansion coefficients corresponding to the on- and off- diagonal matrix elements. Comparing with the ground state. the on-diagonal elements are electronic surface forces and responsible to the excited state potentials' structural changes. Differently, off-diagonal elements are responsible for the non-adiabatic couplings for transferring wave packet population between different excited states.[73, 74, 75] Molecular symmetry helps obtaining the vibronic coupling Hamiltonian and many parameters could be considered as zero due to the symmetry, however a linear vibronic coupling matrix element will only be non-zero if the molecule vibrational mode symmetry and that of the states is written as:

$$\Gamma_i \otimes \Gamma_j \otimes \Gamma_\alpha \supset A \tag{2.19}$$

where, the Γ_i and Γ_j are symmetries of the two states and Γ_α is the symmetry of the mode. Therefore, if the states are given a particular symmetry mode, the off-diagonal elements are only non-zero. For fully symmetry mode, the diagonal elements can only be non-zero. While an accurate Hamiltonian could still be established in low-symmetry molecules, but these rules sued to simplify the process and many coupling terms in the Hamiltonian can be excluded since they were known to be zero. [76]

To obtain the model Hamiltonian and parameters, we adopted the approach shown in Figure 2.2, which provides an illustration, up to second order, of the step wise fitting procedure often used. The first two steps involve defining $H^{(0)}$ and $W^{(0)}$, using the frequency of the normal modes and excited state energies at $\mathbf{Q}_0$, respectively and obtained from quantum chemistry calculations. Subsequently, the linear model is refined (κ, λ), while the remaining parameters are set to zero. Lower order terms, i.e. $H^{(0)}$ and $W^{(0)}$ are fixed to the value determined during the previous step. Higher order, such as second and fourth order terms can also be obtained and follow a

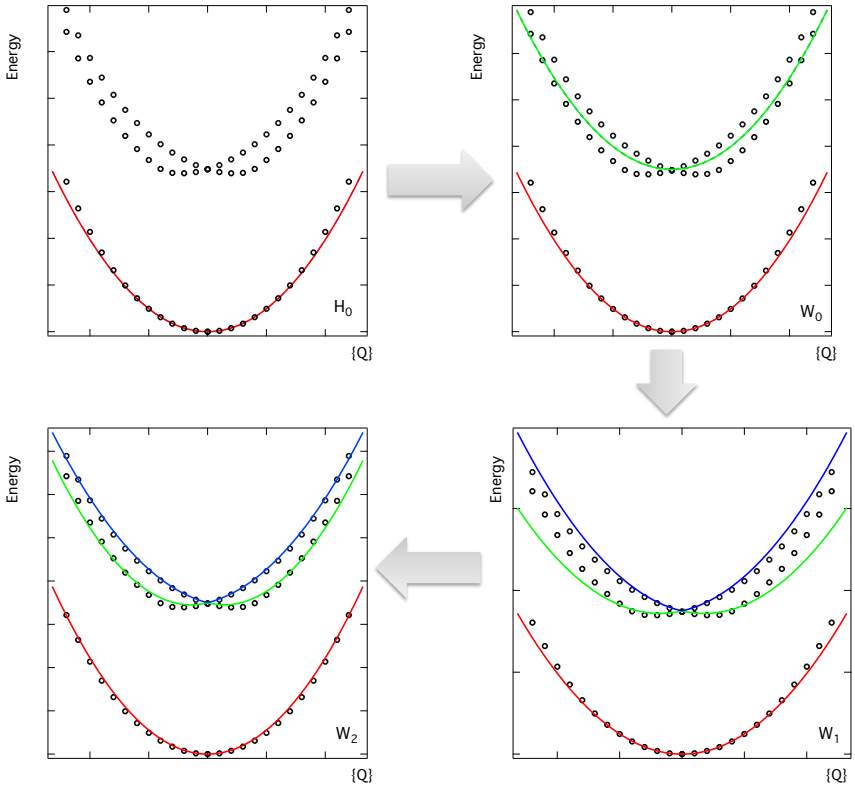

FIGURE 2.2: Schematic show the step wise fitting procedure used to obtain the Vibronic Coupling Hamiltonian. Initially, $H^{(0)}$ and $W^{(0)}$ are defined using a frequency and excited state calculation at $\mathbf{Q}_0$. Subsequently, the linear model and the quadratic terms are fit. This is done in a step wise manner always keeping parameters at lower orders fixed. It is noted that all states, (red, green and blue lines) are present in all of the fits but may not be observed as they overlap.

similar pattern.

Finally, it is important to note that these models are generally reduced coordinated, i.e. they don't include all of the normal modes due to the computational expense. It is therefore crucial that the most important modes to the dynamics are identified. Indeed, it is often possible to identify a subset of important vibrational degrees of freedom in any excited state dynamics process. However such models will not capture accurately effects such as vibrational relaxation and intramolecular vibrational redistribution. Therefore simulations longer that a few picoseconds must carefully consider the influence of this effect on the interpretation of the dynamics.

2.5 Density Functional Theory

As described above, obtaining an expression for the potential energy surface is crucial to performing quantum dynamics and here the choice of electronic structure method is vital. Throughout this thesis, due to the favourable balance between computational expense and accuracy, Density Functional Theory (DFT) has been adopted. In the following we describe the underlying theory of both DFT and its time-dependent variant, TDDFT.

2.5.1 First Hohenberg-Kohn Theory

The foundations of DFT were derived by Hohenberg and Kohn, whose theorems relate to any system consisting of electrons moving under the influence of an external potential, developed by Walter Kohn and Pierre Hohenberg in 1964 while working at the University of California at Los Angeles.[77, 78] Prior to their work, the electronic structure of an atom or molecule was predicted using atomic orbitals. These methods could be inaccurate as they did not take into account electron-electron correlation. In addition, the dimensionality issue related to the atomic orbitals made them computationally challenging.[79] However, Kohn and Hohenberg correctly theorized that all electrons should be described in terms of electron density in order to predict ground state energy of an atom or molecule.

Hohenberg–Kohn's first theorem asserts that n(r) is a unique function of electron density in every system with interacting many particles and an interparticle interaction that is known (Hohenberg and Kohn, 1964).[77] As a result, the ground state wave function may be written as a distinct functional of the ground state electron density, $\Psi_0 = \Psi[n_0]$, by inverting the equation

below. For example, the ground state energy E may be expressed in terms of ground-state density, as indicated in the equation below:

$$E[\Psi[n_0]] = \langle \Psi[n_0] | (\hat{T} + \hat{V} + \hat{U}) | \Psi[n_0] \rangle \tag{2.20}$$

The first Hohenberg–Kohn theorem establishes that a functional of the electron density $E[n_0]$ exists, although the theorem says nothing about the functional's actual shape. Functionals may be described by the second Hohenberg–Kohn theorems, one of which claims that "the electron density that minimizes total energy is real electron density corresponding to all possible complete solutions of the Schrödinger equation". [80] In order to discover the ground-state electron density, one may attempt to reduce the energy by altering the electron density. All attributes may be determined if the ground-state electron density is known.

2.5.2 Second Hohenberg-Kohn Theory

The density may be used to construct a universal function for the energy $E[n]$. This functional's global minimum value is the precise ground state energy. Since the density defines the external potential, and the potential determines the ground state wave function (unless in degenerate conditions), all other observable of the system are unique. It is possible to express energy as a density-dependent function. This often calls for a detailed explanation of how to transform the overall energy representation from wave function representation to density representation.[77, 78]

$$E[n] = T[n] + E_{int}[n] + \int V_{ext}(\vec{r}) n(\vec{r}) + E \equiv F[n] \int V_{ext}(\vec{r}) n(\vec{r}) + E \tag{2.21}$$

Where, using the universal functional F, kinetic and internal potential energy are treated identically in all systems. In the ground state, the distinct destiny $n(1 \sim r)$ defines the energy,

$$E^{(1)} = E[n^{(1)}] = \langle \Psi^{(1)} | \hat{H}^{(1)} | \Psi^{(1)} \rangle < \langle \Psi^{(2)} | \hat{H}^{(1)} | \Psi^{(2)} \rangle = E^{(2)} \tag{2.22}$$

If one minimizes with regard to $n(r)$, one may determine the total energy of the system represented as a functional of $n(r)$. The ground state density is thus the optimal density for minimizing energy consumption. The surprising allegation that there is a one-to-one match between densities and external potentials was raised by the Hohenberg and Kohn theorems, despite their

seeming simplicity. [81] According to Hohenberg and Kohn, these two theorems may be used in particular situations. The good news is that we don't have to worry about these issues since the density of atomic systems does follow these rules in reality.

2.5.3 Kohn-Sham theorem

The Hohenberg-Kohn theorems establish the framework for density functional theory, but they do not permit it to implemented as a usable technique. This is achieved using the Kohn-Sham appraoch. [78, 77]

This casts the system into a fictitious set of noninteracting electrons with the same ground-state density as the real Hamiltonian. This is solved self-consistently as:

$$\left[-\frac{\nabla^2}{2} + v_s[n](\mathbf{r})\right]\phi_i(\mathbf{r}) = \epsilon_i\phi_i(\mathbf{r}) \tag{2.23}$$

where $\phi_i(\mathbf{r})$ is KS orbital i with eigenvalue ϵ_i and:

$$v_s[n](\mathbf{r}) = v_{ext}(\mathbf{r}) + \int d\mathbf{r}^3 n(\mathbf{r}')|\mathbf{r} - \mathbf{r}'| + v_{xc}[n](\mathbf{r}) \tag{2.24}$$

and the exchange-correlation potential,

$$v_{xc}[n](\mathbf{r}) = \frac{\delta E_{xc}[n]}{\delta n(\mathbf{r})} \tag{2.25}$$

In all practical calculations, some form of density functional approximation is used. This means that the density obtained during minimisation will be approximate, $\tilde{n}(\mathbf{r})$.

The performance of Kohn-Sham Density Functional Theory is determined by the unknown kinetic and electron-electron interaction energies, which are described using the exchange and correlation energy functional (E_{xc}).[82] Despite the exact form of E_{xc} being unknown, remarkably simple approximations to it have provided an unrivalled accuracy to cost ratio. Both physically and empirically motivated approaches for developing E_{xc} are used, but nearly all have focused upon improving calculated energies.

2.5.4 Exchange-correlation functionals

DFT is a formally exact theory but requires the exact form of the unknown exact exchange and correlation energy, E_{xc}. As mentioned, remarkably simple

approximations to E_{xc} can be used, and yield surprisingly good computational results. Each functional reaches different levels of accuracy depending on the level of approximation made, this can be described in the context of Jacobs ladder.[83]. The common functionals are outlined in the following subsections.

The Local Density Approximation

The first approximation is the local density approximation (LDA) which is exact only for the homogeneous electron gas. For molecular systems is a crude approximation and therefore is very rarely used. LDA assumes that the electronic properties of a system can be described by the local electron density. This means that the electron density is approximated as a homogeneous and locally constant value within a small region around each atom. This works for systems which can be considered to have a constant external potential, i.e. a metal, because it will locally appear to have a constant density. The exchange correlation energy for the LDA can be written as:

$$E_{xc}[n] = \int n(r)\epsilon_{xc}(n(r))\, d(r) \tag{2.26}$$

where $\epsilon_{xc}(n(r))$ is the energy per electron at the point r in space that only depends on the density at that point. Splitting the exchange correlation energy into its constituent energy densities gives:

$$\epsilon_{xc}(n(r)) = \underbrace{\epsilon_x(n(r))}_{\text{exchange energy density}} + \underbrace{\epsilon_c(n(r))}_{\text{correlation energy density}} \tag{2.27}$$

and applying HF theory to calculate the exchange energy density gives,

$$\epsilon_x(n(r)) = \frac{3}{4}(\frac{3}{\pi})^{1/3} \int n(r)^{4/3}\, dr. \tag{2.28}$$

The exchange potential for the LDA is simply,

$$V_x(r) = (\frac{3}{\pi})^{1/3}\ n^{1/3}(r). \tag{2.29}$$

Therefore, the LDA provides a reasonable solution to the exchange correlation term that scales linearly with system size. However, it does underestimate the Kohn-Sham energy eigenvalues due to self-interaction errors, making it unsuitable for many chemical systems.

Generalised-Gradient Approximation

To improve the LDA, which operates under the assumption that the density changes very slowly, the gradients of the electron density are added to the exchange correlation. This is known as the generalised-gradient approximation (GGA),

$$E_{xc}^{GGA} = \int f(n(r)\nabla n(r)\ d(r). \tag{2.30}$$

The GGA provides a computationally inexpensive route to more accurate DFT calculations, specifically accurate descriptions of structures. Some popular GGA functionals include PBE[84] and BLYP[85, 86].

Hybrid Functionals

GGA functionals, however, often fail to accurately describe non-local properties, such as CT states and van der Waals bonding. Such failings can be attributed to the GGA functionals poor description of long range electron-electron interactions, as well as the poor description of the rapid decay of the exchange and correlation potentials.[87] These inaccuracies are in part due to the self-interaction error in DFT. Unlike in DFT, Hartree-Fock theory exactly cancels the interaction of an electron with itself by the exchange term. However, in DFT, this exchange term is approximated and so does not exactly cancel the self-interaction, resulting in surplus self-interaction. Therefore, hybrid functionals were developed, built using a portion of exact exchange from HF mixed with a portion of exchange from DFT. This produces functionals of the form:

$$E_{xc}^{hybrid} = aE_x^{HF} + (1-a)E_x^{DFT} + (1-a)E_c^{DFT}. \tag{2.31}$$

The implication of a hybrid functional can improve the accuracy of many properties, such as, bond lengths, vibration frequencies and the description of excited states,where the a is the mixing parameter(usually set between 0.2 to 0.5), xc means exchange-correlation, x means exchange and c means electronic. Although there are several limitations of typical hybrid functionals, for example, the computational expensive, underestimation of band gap, and spin contamination. Examples of commonly used hybrid functionals are B3LYP[86, 88, 89] and PBE0[90].

2.6 Time Dependent Density Functional Theory

2.6.1 The Runge-Gross Theorem

Among quantum chemistry computations and the study of condensed matter systems, DFT is a popular technique. For many physical scientists, this approach serves as a means of theoretically proving the validity of an experimental finding. However, although this does not always entail providing the most accurate outcomes, it frequently offers an optimal trade-off between efficiency (computing time for a given CPU power) and the quality of outcomes.

However, DFT is only applicable for electronic ground states. To address properties beyond their ground or equilibrium state, we can use TDDFT. The framework of TDDFT is based upon describing the dynamical response of a system, which can use time-dependent Schrödinger equation. Non-relativistic interactions between N electrons, each with an explicit time dependency V, may be considered. The Runge-Gross (RG) theorem does not apply to all potentials,[79] and we'll discuss this in more depth later. For the time being, let's assume that it has the potential to be a real-world function. This is the complete Hamiltonian for the N-electron system:[91]

$$\hat{H}(t) = \hat{T} + \hat{V}(t) + \hat{W} \tag{2.32}$$

where, the terms in the Hamiltonian are given by,

$$\hat{T} = \sum_{j=1}^{N} -\frac{\nabla_j^2}{2}; \hat{V}(t) = \sum_{j=1}^{N} v(r_j, t); \hat{W} = \sum_{j \leq k}^{N} \frac{1}{|r_j - r_k|} \tag{2.33}$$

where, the $\hat{T}$ is the kinetic energy, $\hat{V}(t)$ is the potential energy, and $\hat{W}$ is the electron repulsion. The time-evolution of the N-electron quantum system is given by the time-dependent Schrödinger equation:

$$i\frac{\partial}{\partial t}\Psi(r_1, r_2, ..., r_N) = \hat{H}\Psi(r_1, r_2, ..., r_N) \tag{2.34}$$

To put it another way, the equation 2.27 may be seen as a way to propagate an initial state A=B from an initial time t_0 to the future time t_1. Assuming that the system is in its staring condition, the time-dependent potential may be expressed as:

$$v(r, t) = v_0(r) + v_1(r, t)\theta(t - t_0) \tag{2.35}$$

where, the θ is the Heaviside step function.

2.6.2 Time-dependent Kohn-Sham equation

All many-particles observations may be obtained from a single particle density, which is the target of DFT. A fictitious set of N orbitals $\{\phi_j, j = 1, ..., N\}$ may be used to compute the density, we suppose:

$$n(\vec{r}, t) = \sum_{j=1}^{N} |\phi_j|^2. \tag{2.36}$$

First assumption proposes that the orbitals satisfy a Schrödinger equation of the type:

$$i\partial_t \phi_j(\vec{r}, t) = (\frac{-\nabla^2}{2} + \nu_{KS}(\vec{r}, t))\phi_j(\vec{r}, t), j = 1, ..., N \tag{2.37}$$

which assumes that the single-particle potential ν_{KS} exists. Runge-Gross theory ensures that if this potential exists, there is only one single-particle potential up to an additive time-dependent function,[79] which in combination with the time-dependent Kohn-Sham equations yields the correct one-particle density n. The Kohn-Sham equations in essence offer a precise mapping of the N-electron issue into a series of single-particle problem. It's critical to keep in mind, however, that the Kohn-Sham potential is not known directly. However, there are several general features of the Kohn-Sham potential that may be established: Hartree-Fock theory's exchange term in non-local in space, although the Kohn-Sham potential is unique functional of the precise density for every given starting state Ψ_0 and Kohn-Sham determinant $\Phi_0 = det(\phi_1, ..\phi_N)/\sqrt{(N!)}$, as shown by Runge-Gross theorem. [92] If we assume that the time-dependent electronic system develops from a non-degenerate ground state of the originally undisturbed system, which, through stationary DFT, is entirely specified by its corresponding density $n_0(\vec{r})$, the latter requirement may be greatly simplified. For example, Kohn-Sham potential is a unique function of density in this situation:

$$\nu_{KS}[n, \Psi_0, \Phi_0] = \nu_{KS}[n](\vec{r}, t). \tag{2.38}$$

The Hartree potential, which contains the screening of the external potential ν_H owing to electrons, and an actual quantum portion ν_{xc} of the exchange-correlation potential are the two classical parts of the Kohn-Sham potential

that are often divided based on experience with single-particle images:

$$v_{KS}[n](\vec{r},t) = v(\vec{r},t) + v_H[n](\vec{r},t) + v_{xc}[n](\vec{r},t) \tag{2.39}$$

$$v_H[n](\vec{r},t) = \int d^3r' \frac{n(\vec{r},t)}{|\vec{r}-\vec{r}'|} \tag{2.40}$$

Time-dependent Kohn-Sham has made the motion of electrons visually, also could convert the response to usual frequency dependent spectra by Fourier transform. Kohn-Sham equation has advantages in some points, but it can be time-expensive in computational calculations.

2.6.3 Linear-Response Time-Dependent Density Functional Theory

Kohn-Sham equation has shown a clear way to calculate the time-dependent system, computationally, but it can be time-expensive for some molecules. To reduce the amount of computation associated with resolving the effects of external fields on the quantum system, the interaction can be approximated as a linear response. By considering the perturbation to the system by the time-dependent field is small, with this approximation, the response to the interaction can be written as a Taylor expansion:

$$\rho(r,t) - \rho_0(r,t) = \rho_1(r,t) + \rho_2 r,t + \rho_3(r,t) \tag{2.41}$$

where, $\rho_0(r,t)$ is the initial density and zeroth order of the external perturbation. In the meantime, the first order response $\rho_1(r,t)$ writes as:

$$\rho_1(r,t) = \iint \chi(r,t,r',t) v_1(r',t) d^3r dt \tag{2.42}$$

where, χ is the density response of the interacting system. For a non-interacting system, the density response as shown for the kohn-Ssham system is used and it's related to the new density response , χ. Obviously, virtual system can be used to relate with the real relevant interacting system. So the deriving the effective potential from Kohn-Sham system to real system is feasible. When Linear-Response TDDFT(LR-TDDFT) is implemented into codes, a set of electron orbital transitions are used to describe the density response. To describe the external perturbations during excitation and de-excitation processes, the Casida formalism used Kohn-Sham orbitals,[93] equation shows

as:

$$\begin{pmatrix} A & B \\ B & A \end{pmatrix} \begin{pmatrix} X \\ Y \end{pmatrix} = \omega \begin{pmatrix} 1 & 0 \\ 0 & -1 \end{pmatrix} \begin{pmatrix} X \\ Y \end{pmatrix} \tag{2.43}$$

where, X describes excitions and Y for de-excitations, ω is the excited states energy, A and B defined as:

$$A_{ia,jb}(\omega) = \delta_{ij}\delta_{ab}(\epsilon_a - \epsilon_i) + (ia|f_H + f_{xc}|jb) \tag{2.44}$$

$$B_{ia,ib}(\omega) = (ia|f_H + f_{xc}|jb) \tag{2.45}$$

where, i,j stands for Kohn-Sham orbitals in ground states, and a,b for excited states, ϵ is the Kohn-Sham orbitals' energies. Tamm-Dancoff Approximation (TDA) [94] has been used to solve the equation 2.43, which the de-excitation components are neglected, so equation 2.43 can be rewrote to:

$$AX = \omega X \tag{2.46}$$

TDA is commonly used to solve LR-TDDFT.

2.7 Marcus Theory

In chemistry reactions, electron transfer processes play a vital role. All of respiration and photosynthesis depend on electron transfer processes between co-factors in proteins, which is the most important aspect of how energy is acquired from food and oxygen. Nano-scale electrical devices, in a molecular sense, are essentially performing the work of moving electrons and protons around to change the form of energy. It's also a good idea to study electron transfer since it's a very basic chemical process that can help us comprehend different types of chemistry and biology.

Using the rate constant k as a starting point, Rudy Marcus came up with the idea to create two parabolas for an electron transfer process. The reactant's energy was represented by the one parabola, whereas the product's energy was represented by another parabola. In other words, if the nuclei were linked by springs, the graph would look like a parabola. Stretching or compressing the springs from their equilibrium points does not affect the energy since it is proportional to the square of the distance traveled. Because the charge on the atoms or molecules involved in electron transfer varies and thus the attraction or rejection of the items being held by the springs changes.

The reactant and the product have different equilibrium nuclear locations (x-axis values).[95]

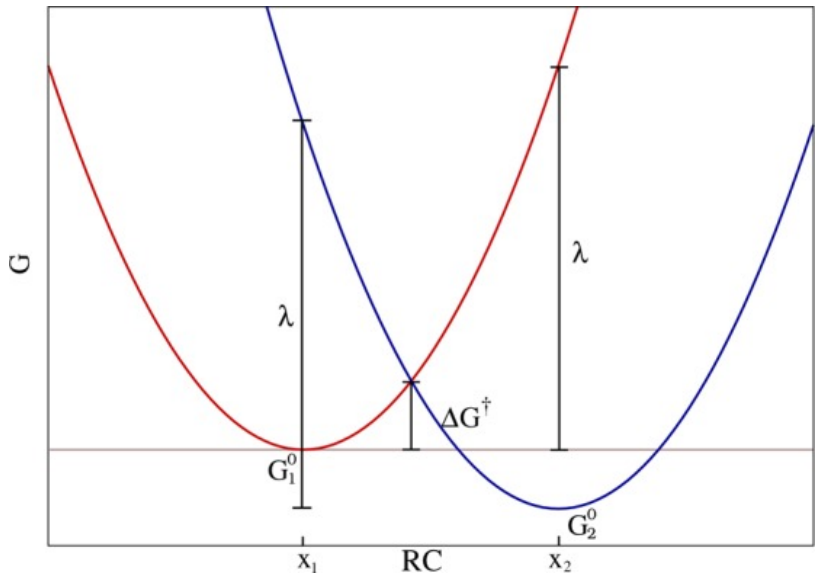

FIGURE 2.3: Marcus theory used two parabolas to explain electron transfer reactions. And red parabola stands for the reactant, blue for product. The activation energy, the free energy change of the reaction and the reorganization energy are $\Delta G^{\dagger}$, ΔG_1^0 and λ. x_1 and x_2 are the equilibrium states for reactant and product nuclei coordinates.

Reactant(red) and product energies(blue) are shown in figure 2.3, which includes a free energy change (G_1^0), reorganization energy (λ) and activation energy ($\Delta G^{\dagger}$). λ is the the energy forcing the reactant to have same nuclear configuration as product without any electrons transferred. G_1^0 is the free energy change between the reactant and product, and the expression: [96]

$$G^{\dagger} = \frac{\lambda}{4}(1 + \frac{\Delta G_1^0}{\lambda})^2 \tag{2.47}$$

Besides, Marcus also brought forward the electron transfer rate equation based on the free energy and reorganization energy:

$$k = \frac{2\pi}{\hbar}|H^2|\frac{1}{\sqrt{4\pi\lambda K_B T}}e^{-\frac{(\lambda+\Delta G)^2}{4\lambda K_B T}} \tag{2.48}$$

where, the K_B is Boltzmann constant, T is the room temperature, 298K and the coupling Hamiltonian H.

2.8 Quantum Dynamics

The proper modeling of many-body quantum processes for sophisticated systems is a major problem in theoretical physical chemistry. Chemical reaction dynamics are a particularly difficult problem since the system is always out of balance, and many quantum states are involved in the overall process. Using a brute-force technique, the overall wave function may be enlarged in static basis processes that fully cover the Hilbert space of the issue (complete in the sense of numerical convergence). For minor gas-phase reactions. In the previous several decades, there has been a significant increase in the number of degrees of freedom that can be calculated, from 2–4 degrees of freedom in the 1980s to 10–12 degrees of freedom now. Some approaches established in this context aren't immediately transferable to bigger systems. Conventional, full-configurational techniques have a significant challenge because of the fast expansion of the number of basis functions compared to the system's size. Not only does this "curse of dimensionality" occur in high-dimensional spaces when data are studied and arranged, but it also happens in other domains, such as numeric analysis and data mining. To get beyond a few degrees of freedom, a practical strategy must take a different path. The essence of the issue has been overlooked in standard quantum wave packet approaches. There is no difference in the technique used to set out the basic functions, whether they are highly linked or weakly coupled, classical or quantum. There is a lot of potential here, but it seems like a waste if one considers how frequently specific versions of the Hamiltonian appear in physics and chemistry and how effectively they can be approximated. There are two broad groups of reaction dynamics studies now under development: approximation and numerically accurate.

2.8.1 Multi-Configuration Time-Dependent Hartree

The easiest way to solve the TDSE is to expand the nuclear wavefunction into a time-independent product basis set with time-dependent coefficients:

$$\Psi(x_1, x_2, ..., x_f, t) = \sum_{j_1=1}^{n_1} ... \sum_{j_f=1}^{n_f} C_{j_1 ... j_f}(t) \prod_{k=1}^{f} \chi_{j_k}^{(k)}(x_k) \tag{2.49}$$

where, the orthonormal basis and nuclear coordinate are χ_j and x_k. Although it described the nuclear wavepacket like another method in electronic structure theory, full configuration interaction (Full- CI), it faces the serious scaling problem. In fact, it's related with the number of degrees of freedom, so an approximate methods are required. One of the solutions is the Multi-Configuration Time-Dependent Hartree (MCTDH) method. In this method, the nuclear wavefunction ansatz described as:

$$\Psi(Q_1, Q_2, ..., Q_f, t) = \sum_{j_1=1}^{n_1} ... \sum_{j_f=1}^{n_f} A_{j_1 ... j_f}(t) \prod_{k=1}^{f} \phi_{j_k}^{(k)}(Q_k, t) \tag{2.50}$$

where, the Q_1,...,Q_f are the nuclear coordinates, MCTDH expansion coefficients are written as $A_{j_1 ... j_f}$ and $\phi_{jk}^{(k)}$ stands for the n_k expansion functions for each degree of freedom k known as single particle functions (SPFs). In form, the ansatz for MCTDH wavefunction is similar to standard wavepacket approach. But importantly, the basis functions are time-dependent, which means fewer basis functions are needed to be converge during the calculation.

The SPFs used in MCTDH have two advantages: (1) fewer are required as they are variationally determined (2) the functions can be multi-dimensional particles containing more than one degree of freedom thus reducing the effective number of degrees of freedom. The wavepacket simulation describes the evolution of a certain, well defined, initial state. However for a system at finite temperature, important in the context of the simulations addressing the rISC rate, there obviously exists a mixture of different thermally excited states.

Importantly the SPF reduces the effective number of degrees of freedom for the purpose of the simulations. The memory required by the standard method is proportional to N^f, where N is the number of grid points for each f degree of freedom. In contrast, the memory needed by the MCTDH method scales as:

$$memory = fnN + n^f \tag{2.51}$$

where the first term is due to the (single-mode) single-particle function (SPF) representation, and the second term the wavefunction coefficient vector A. As $n < N$, often by a factor of five or more, the MCTDH method needs much less memory than the standard method, so allowing larger systems to be treated. Indeed the standard implementation of MCTDH can treat, depending on the exact details of the calculations, $\sim$50 nuclear degrees of

freedom.

2.9 Molecular Dynamics

Molecular dynamics (MD) simulation has been widely used in the computational research field to describe complex system and show macroscopic information from atom/molecules level. Molecular dynamics are delivered in a variety of different methods, namely: i) *ab initio*, ii) QM/MM and iii) classical. In all cases the motion of the nuclei is described classically, *i.e.* evolves according to Newtons equations of motion. The difference between them is description of the potential.

The molecular dynamics equations of motion are written as:

$$m_i \ddot{\mathbf{r}}_i = f_i \tag{2.52}$$

$$f_i = -\frac{\delta}{\delta r_i} U. \tag{2.53}$$

Where m_i is the mass of the particle and r_i is the position. The forces f_i acting on the atoms can be derived from the potential energy $U(r^N)$. Where $r^N = (r_1, r_2, \cdots r_N)$ represents the complete set of $3N$ atomic coordinates. These $3N$ equations are solved for each particle at each time step. Different algorithms to solve these equations of motion can be applied in MD simulations. However, each algorithm is expected to maintain three properties: Firstly, that the equations of motion are reversible in time. Once the trajectory of a system is solved, it should be possible to trace back its dynamics by reversing the sign of the position and momentum. Secondly, the spacial derivative of the potential determines the motion of the particles, that is to say, if the same system is acted on by two different potentials it will produce two different trajectories.

Finally, the algorithm must be symplectic, i.e., preserve the energy of the system throughout the simulation. A common approach to ensure this is the Verlet algorithm[97]. Here the user choices a sufficiently small time step δt (normally $\delta t \leq 0.4$ fs) and specific boundary conditions, and algorithm returns the position and the velocities at each successive time $(t + \delta t)$.

The potential energy that is used to describe the system is crucial to the accuracy of the calculations. Throughout this work we have use the QM/MM framework which is described in the following subsection. Finally, within the

framework of MD thermostats or barostats can be used to control temperature or pressure, respectively. Thermostats control the temperature through the kinetic energy of the nuclei, whilst barostats control pressure by adjusting the volume of the calculated system.

2.9.1 QM/MM

The quantum mechanics/molecular mechanics (QM/MM) method is a computational approach for studying the interactions between quantum mechanical and classical mechanical degrees of freedom in chemical and biological systems. The method combines the quantum mechanical treatment of small regions of a system, typically those that exhibit quantum mechanical behavior, with the classical mechanical treatment of the remaining regions, which are typically treated as a passive environment.[98]

The QM/MM method was first introduced in the 1970s and has since become a widely used tool in the study of chemical and biological systems, including enzymes, chemical reactions, and large protein-ligand complexes. The method has been particularly useful in the study of enzymatic reactions, where it has been used to provide insight into the mechanism of enzyme catalysis, the energetics of substrate binding, and the role of protein-ligand interactions[99].

In a typical QM/MM simulation, the quantum mechanical region of the system is treated using quantum chemical methods, such as Hartree-Fock or density functional theory, while the classical mechanical region is treated using molecular mechanics methods, such as the Amber or CHARMM force fields. The interactions between the quantum mechanical and classical mechanical regions are treated through a boundary condition known as the QM/MM boundary, which defines the interface between the two regions.

The QM/MM method offers a powerful tool for understanding the complex interactions between quantum mechanical and classical mechanical degrees of freedom in chemical and biological systems, and has been widely used in the study of chemical reactions, enzymes, and protein-ligand interactions.The hybrid QM/MM methodology, which combines the qualities of ab initio QM calculations (accuracy) and MM procedures (speed) is a highly appealing procedure for simulations. Here efficiency and accuracy for larger systems is achieved by using a quantum mechanical (QM) approach to a small portion of system understudy - the most important active site.[100, 101] At the same time, molecular mechanics is used in handling the rest of

the system. This approach is unique in that it includes the entire system, in contrast to the alternative QM-cluster approach, which excludes most of the system. This reduces the risk of bias and allows for a detailed study of how the surrounding environment affects the properties in question. The full energy associated to the QM/MM Hamiltonian is then expressed as:

$$E = E_{QM} + E_{MM} + E_{QM/MM} = \langle \psi | \hat{H}_{QM} + \hat{H}_{MM} + \hat{H}_{QM/MM} | \psi \rangle \quad (2.54)$$

where the first term accounts for the energy from the QM part, the second term represents the energy from the classical MM region, while the third one is the energy due to the interaction between the QM and MM particles. In a QM/MM scheme, the energy of QM region is extracted from any quantum mechanical theory, like HF, semi-empirical or DFT method, while the energy of MM region is described by the force field. The new element in this theory is then the last term of the Eq. 2.54 and its evaluation gives rise to the so-called different *embedding* schemes, which are currently the main challenge relative to the QM/MM field.

Chapter 3

Excited State Intramolecular Proton Transfer Dynamics for Triplet harvesting in Organic Molecules

3.1 Introduction

Thermally activated harvesting of low-lying non-emissive triplet excited states is an active area of research with potential applications across organic electronics, including light emitting diodes[102, 14], lasers[103, 104], and photovoltaics.[105, 106] This interest is driven by the fact that for organic systems, the weak coupling between triplet and singlet states means that triplets often act as low energy trapping sites, ultimately leading unwanted processes which are detrimental to device performance.

To date, the most successful design strategy for organic triplet harvesters have been based upon intra-/intermolecular donor-acceptor (D-A) systems exhibiting charge-transfer (CT) transitions.[107] This minimises the exchange energy between singlet and triplet states of the same character providing a small energy gap to permit thermal activation of harvesting.[108] In the context of organic light emitting diodes (OLEDs), while these D-A molecules are able to achieve 100% internal quantum efficiency[38], the use of CT states means that the radiative rate is usually low[109] which leads to long excited state lifetimes and consequently instability and reduced device performance associated with excited state quenching mechanisms.[110] In addition, the electroluminescence (EL) from these molecules is inherently broad emission, with a typical full-width at half-maximum (FWHM) 70-120 nm. This width reduces colour purity, making them difficult to use in displays, which require a FWHM <30 nm. Consequently, commercial OLED displays employ lossy colour filters and/or expensive, difficult to fabricate optical microcavity

structures to achieve sufficiently narrow line widths to satisfy the colour requirements. This filtering of the original electroluminescence (EL) emission significantly reduces the external quantum efficiency (EQE) of the display, increases power consumption and shortens operational lifetime because the pixels need to run at higher brightness to compensate for this loss.

To overcome this, Hatakeyama et al.[111] have developed an approach that reduces the energy gap between the singlet and triplet states by exploiting the opposite resonance effect of nitrogen and boron atoms in a para-substitution arrangement. This can separate the highest occupied molecular orbital (HOMO) and lowest unoccupied molecular orbital (LUMO) without the need to introduce donor or acceptor groups. This makes it possible to design rigid molecules that exhibit a very narrow FWHM. There are researches indicated that rigidity or flexibility of the molecule in OLEDs can have a significant impact on the process of triple harvesting. Triplet excitons are typically more challenging to convert into electricity than singlet excitons. [112] Triplet excitons are often produced through a process called intersystem crossing, where a singlet exciton undergoes a spin-flip to become a triplet exciton. The rate of intersystem crossing is influenced by the energy gap between singlet and triplet states. In rigid molecules, the energy gap between singlet and triplet states is often larger, making intersystem crossing less efficient. This means that less energy is available in the form of triplet excitons for harvesting.[113] However, the rigidity of the molecule restricts the triplet harvesting [114]severely limiting device performance, especially at normal brightness levels where a large roll-off in the efficiency is observed.[111] This is consistent with the spin-vibronic mechanism[115] for efficient triplet harvesting, which shows that the small mixing between singlet and triplet states due to spin-orbit coupling can be enhanced by coupling to multiple excited states driven by specific molecular vibrations.[116][37][117] However, in the case of rigid molecules, the role of vibrations is obviously reduced quenching the triplet harvesting rate.

To diversify molecular design approaches for thermally activated delayed fluorescence(TADF) materials which are required to overcome some of the aforementioned limitations, Mamada et al.[54] have recently investigated the possibility for triplet harvesting based upon excited state intramolecular proton transfer (ESIPT). In this case, photoexcitation drives the transfer of a hydrogen atom covalently bonded to one atom to a second on the same molecule. This changes the electronic structure causing separation of the HOMO and LUMO orbitals reducing the energy gap between the low lying

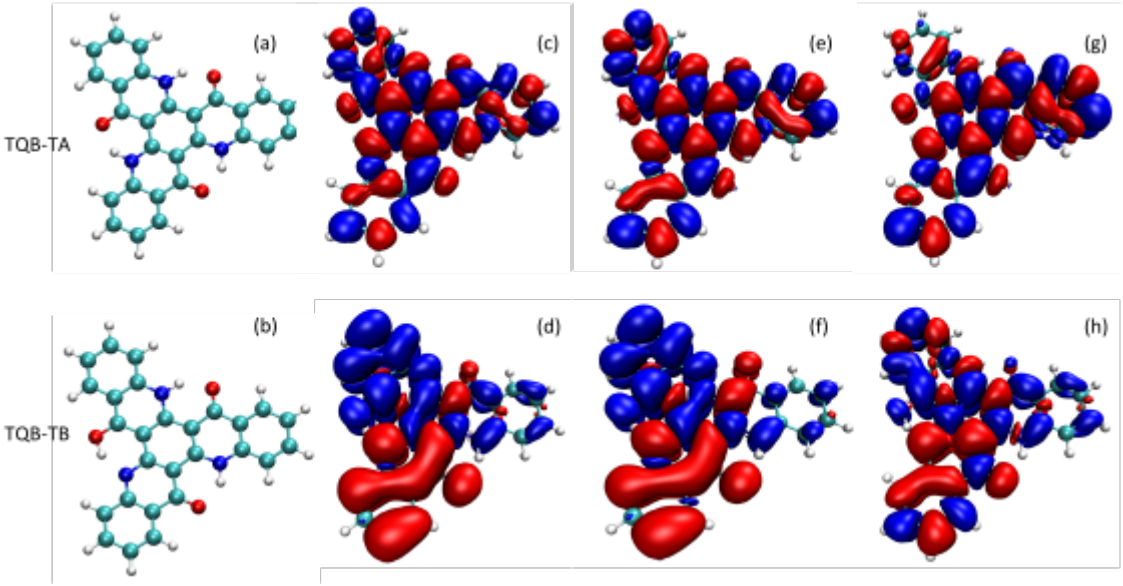

FIGURE 3.1: The structure of TQB-TA (a) and TQB-TB (b) optimised using DFT/TDDFT(PBE0) and a Def2-SVP basis set. The density differences ($\delta\rho = \rho_{S_1} - \rho_{S_0}$) for the S1 state at the TQB-TA (c) and TQB-TB (d) geometries, the T1 state at the TQBTA (e) and TQB-TB (f) geometries and the T2 state at the TQB-TA (e) and TQB-TB (f) geometries.

excited states. This effect of ESIPT is well documented,[55] and the solvatochromism, indicative of a state of CT characteristics, in the emission of such materials has widely been reported.[56][57] Indeed, TADF from ESIPT materials in solution has previously been reported by Park et al.[58] However, importantly in this case the large amplitude motions of the molecules were required to enable ESIPT and therefore TADF. While this does not affect the solution phase measurements of Park et al.,[56] it represents a severe limitation for triplet harvesting in OLEDs, which exist in the solid state,[59] therefore constraining larger amplitude motions required. Importantly, the molecule, triquinolonobenzene (TQB,3.1) developed by Mamada et al. demonstrated ESIPT for a rigid structure, and demonstrated it was able to harvest a large contribution of the triplets states by achieve up to 14% external quantum efficiency (EQE) when integrated into an OLED.

This high EQE of TQB is encouraging for a new emitter design. However the close to unity triplet harvesting efficiency required to achieve this is somewhat unexplained, especially given the comparatively large singlet-triplet energy gap and the weak delayed fluorescence exhibited upon photoexcitation in both solution and the solid state. In this paper we combine quantum chemistry, molecular and quantum dynamics to study the excited

state processes and triplet harvesting mechanism in TQB. We show that despite the proton transfer forming TQB-TB in the singlet excited state occurring on a timescale much faster than intersystem crossing (ISC), it plays a crucial role in the triplet harvesting mechanism. This arises due to multiple low-lying triplet states that are strongly coupled along the proton transfer coordinate and tend to favour the structure without proton transfer (TQB-TA). A model Hamiltonian is developed and used to simulate absorption spectrum and corresponding excited state dynamics. We find an intersystem crossing rate which is in good agreement with that reported experimentally and show a splitting of the wavepacket between the TQB-TA and proton transferred TQB-TB forms. Using this and the relative energy gaps of the two structures to the emissive singlet excited state, we propose that the high device performance arises from a combination of TADF and triplet-triplet annihilation (TTA) occurring from the TQB-TA and TQB-TB, respectively. This can explain both the high EQE's and the importance of the host material used to achieve them.

3.2 Methods

3.2.1 Quantum Chemistry

The geometry of TQB in its ground and relevant excited states were calculated using density functional theory (DFT) and linear response time-dependent density functional theory (LR-TDDFT) within the Tamm-Damcoff approximation[118] and the PBE0 exchange and correlation functional[119][120] as implemented within the Q-Chem quantum chemistry package.[121] A Def2-SVP[122] basis set was used throughout and the solvent was described using conductor-like polarizable continuum model[123] using the dielectric constant of toluene. Emission energies, calculated using the S_1 optimised geometries, included a state-specific polarizable continuum model (SS-PCM).[124] For the SS-PCM, the energy of both the S_1 and ground state were calculated within an S_1 optimised solvation structure, yielding the vertical emission energy.

3.2.2 Ab initio Molecular Dynamics

Ab initio molecular dynamics (MD) of TQB in its electronic ground and excited singlet (S_1) state were performed using the Terachem package.[125, 126]

The potential energy and forces was calculated using DFT(PBE0) and a 3-21g* basis set. The effect of the environment was included using a conductor-like polarizable continuum model[123] using the dielectric constant of toluene. The MD was performed using a microcanonical (NVE) ensemble using initial velocities sampled at random from Boltzmann distribution of velocities at 300K. 20 configurations selected at random from 10 ps of ground MD were used to compute the excited state dynamics in the S_1 state, with a particular focus upon the first 100 fs and the proton transfer. 20 configurations from the ground state MD were used to simulate the absorption spectrum, while excited state geometries were used to simulate the emission spectrum. The total emission spectrum was generated by summing the contributions of each spectrum for which the oscillator strength had been broadened by a Gaussian function of full width half maximum of 0.05 eV.

3.2.3 Quantum Dynamics

The nonadiabatic excited state quantum dynamics of TQB were investigated using a model Hamiltonian operator based upon the Spin-Vibronic Coupling Hamiltonian[115] (H^{SO-vib}). This Hamiltonian is the sum of a non-relativistic vibronic coupling Hamiltonian matrix (H^{vib}), and spin-orbit, (H^{SO}) Hamiltonian matrices:

$$H^{so-vib} = H^{vib} + H^{SO} \tag{3.1}$$

H^{SO} is comprised of off-diagonal spin-orbit coupling terms, which can either be Q-dependent[127] or Q-independent[128]. Where Q represents the dimensionless (mass-frequency scaled) normal mode coordinates. In this present work, the spin-orbit coupling terms are Q-dependent[127] along the proton transfer mode as described in the supporting information. The vibronic coupling Hamiltonian matrix is expressed:

$$H^{vib} = (T_N + V_0)1 + W \tag{3.2}$$

T_N is the kinetic energy operator. In the absence of large-amplitude motions as in the case here for a rigid molecule, a model potential in terms of a subset of the ground state normal modes can be determined. In the present case, the normal modes are evaluated at the midpoint of the proton transfer geometry. This choice of coordinates simplifies the construction of the Hamiltonian as the kinetic energy operator has a simple separable form.[129]

V_0 is the ground state potential and defined as a harmonic oscillator with vibrational frequencies ω_i corresponding to dimensionless normal coordinate Q_i. W is the diabatic coupling matrix which is expanded as a Taylor series up to order in the present work.[130, 131] This matrix contains both on and off-diagonal elements. The on-diagonal elements are the forces acting within an electronic surface and are responsible for structural changes of excited-state potentials compared to the ground state. The off-diagonal elements are the nonadiabatic couplings responsible for transferring wavepacket population between different excited states. The parameters for these matrix are obtained from a fit to quantum chemistry chemistry points calculated along and diagonally between the normal modes displacements. The parameters obtained from this fit and a description of the model Hamiltonian can be found in the supporting information.

	Modes	N_i,N_j,N_k	n_i,n_j,n_k,n_l
Singlet	ν_1	61	4,4,4,4,4,4,4,4,4,4,4,4,10
	ν_{124}	61	4,4,4,4,4,4,4,4,4,4,4,4,10
	ν_{63}, ν_{88}	21,21	4,4,4,4,4,4,4,4,4,4,4,4,10
Triplet	ν_1	61	8,8,8,8,8,8,8,8,8,8,8,8,4
	ν_{124}	61	8,8,8,8,8,8,8,8,8,8,8,8,4
	ν_{63}, ν_{88}	21,21	8,8,8,8,8,8,8,8,8,8,8,8,4

TABLE 3.1: Computational details for the MCTDH simulations of the TQB model. N_i,N_j,N_k refers to the number of primitive harmonic oscillator discrete variable representation (DVR) basis functions used to describe each mode. n_i, n_j, n_k and n_l are the number of single-particle functions used to describe the wavepacket on each state.

All dynamics were performed using the multi-configuration time-dependent Hartree (MCTDH) method as implemented in the Quantics quantum dynamics package. [132, 133] The calculation details are provided in table3.1 for the case where the singlet state was initially excited (singlet) or where the triplet state was initially excited (triplet). The latter, as discussed below was used to simulate electrical excitation. In the case of dynamics in the S_1 state, simulating photoexcitation, the initial wave function in the ground state, built using one-dimensional harmonic oscillator functions with zero initial momentum, was project onto the S_1 state at the Franck-Condon geometry. For the dynamics simulating the effect of electrical excitation, the wavepacket was projected vertically from the minimum of the cationic and anionic potential energy surface as described in the text below.

The absorption spectrum of TQB using the model Hamiltonian was simulated using the Fourier transform of the autocorrelation function written:

$$I(\omega) \sim \int_{-\infty}^{\infty} C(t) exp^{-i\omega t} t, \tag{3.3}$$

where $C(t)$ is the autocorrelation function. Before the autocorrelation function is transformed it is modified slightly. Artefacts are unable to stop during the analysis, because they are sourced from the unwanted features or distortions in the resulting frequency domain representation of signal. These artefacts can emerge for many reasons and can affect the accuracy and interpretation of the transformed data. For example, when a signal contains sharp discontinuities or step functions,the Gibbs phenomenon occurred. Window function also could lead some artefacts, and aliasing occurs when the sampling rate is insufficient to capture high-frequency components in the signal. To reduce artefacts associated with the finite propagation time (temporal truncation) which causes ringing artefacts in the spectrum, due to taking the Fourier transform only over a finite time interval (Gibbs phenomenon), the autocorrelation function is multiplied by $\cos^2(n\pi t = 2T)$, where n = 1, 2,... and T denotes the final time plus one time step of the autocorrelation function. The autocorrelation function is calculated as:

$$C(t) = \langle \psi_i(0) | \psi_f(t) \rangle, \tag{3.4}$$

where $\psi_i(0)$ is the initial wavefunction in the ground state and $\psi_f(t)$ is the time-dependent wavefunction in the excited state.

The total spectrum is a sum of spectra generated in this way with weighting of $exp(-t/\tau)$, where τ is the damping function applied to the autocorrelation function, in this case 20 fs.

3.3 Results

In the following sections we present a characterisation of the ground and excited state structures of TQB (Figure3.1), followed by its excited state properties. Subsequently, using molecular and quantum dynamics we study its photophysics. Finally, we present a perspective of how this behaviour alters in the case of electrical excitation compared to optical excitation and how this influences the triplet harvesting properties of TQB present in OLEDs.

3.3.1 Ground and excited state structures

TQB can exist in two major tautomers, TQB-TA (Figure 3.1 a) and TQB-TB (Figure 3.1 b). Although Mamada et al.[54] also reported structures involving multiple sequential proton transfers, these are much higher in energy and therefore considered unlikely. In addition, they do not change the gap between the low lying singlet and triplet states and are therefore would not significantly alter the triplet harvesting rate. Table 3.1 shows the optimised structures of each form. As expected, the structure is planar in all cases. In the electronic ground state (S_0) the main structural parameters around the proton transfer site in good agreement with X-ray diffraction reported in ref[54]. The one exception is the hydrogen bond parameters, however, the assignment of the position of this proton is complicated by crystal disorder, and the challenge of identifying hydrogen atoms using X-rays. The geometry of TQB in the present work is in good agreement with calculations presented in ref[54].

Upon excitation into the S_1 state, a stable form of TQB-TA can be optimised and exhibits similar properties as the ground state. However, the lowest energy geometry of the S_1 state is the TQB-TB tautomer, with the proton transferred from the nitrogen to the the oxygen. This structure indicates a compression of the $O-H$ distance by ~ 0.68 Å, elongation of the $C-O$ bond and a slight change in the bond angles involved. Given the small structural changes, which are highly localised around the motion of the proton, and the large energy difference between the two conformers, the proton transfer is excited to be very fast as discussed in the following section. The lowest triplet excited state (T_1), like the singlet state, exhibits stable minima in the TQB-TA and TQB-TB tautomers, but again the lowest energy conformer is TQB-TB. However, in this case there is a change in state character along the proton transfer creating a barrier, which is absent in the singlet states.

Importantly, Table 3.2 shows that despite the large Stokes shift in the emission[54], initiated by the ESIPT process, the structural changes of the TQB in the excited state are small and almost completely localised to the hydrogen bond lengths and angles. This is important in the context of developing a reduced coordinated model Hamiltonian as shown below.

3.3.2 Excited State Properties

Table 3.3 shows the excited state energies of the important low lying states of TQB-TA and TQB-TB at the ground (S_0) and excited singlet (S_1) and triplet

		S_0	T_1		S_1	
	TQB-TA	TQB-TA	TQB-TA	TQB-TB	TQB-TA	TQB-TB
N-H (Å)	0.88	1.04	1.04	1.66	1.04	1.66
O-H (Å)	1.91	1.68	1.68	1.00	1.69	1.00
C-O (Å)	1.25	1.24	1.25	1.33	1.25	1.33
C-C (Å)	1.44	1.44	1.43	1.42	1.42	1.44
C-N-H (°)	116.0	113.5	112.8	102.2	112.9	103.0
C-O-H (°)	102.3	103.0	103.4	106.2	103.6	105.9

TABLE 3.2: Main structural parameters of optimised geometries of stable TQB-TA and TQB-TB tautomers in the ground (S_0) and excited singlet (S_1) and triplet (T_1) states. The molecular structure TQB-TB is not stable in the ground state and thus we could not find the stationary point of its S_0 form. The structure of TQB-TA from ref([54]) corresponds to the one obtained using X-ray Diffraction of the crystal structure.

(T_1) states identified in Table 3.2. At the TQB-TA ground state geometry, the lowest singlet states is at 3.57 eV, and as shown in Figure 3.1 corresponds an excitation that is delocalised over the whole molecule. However, despite the apparent overlap between the HOMO and LUMO orbitals seen in the density difference plot, the oscillator strength (f_{S_1}) for this transition is zero.

	S_0	T_1		S_1	
	TQB-TA	TQB-TA	TQB-TB	TQB-TA	TQB-TB
E_{T_1} (eV)	3.03	2.93	2.14	2.94	2.25
E_{T_2} (eV)	3.16	3.07	2.66	3.08	2.67
E_{T_3} (eV)	3.16	3.07	2.77	3.09	2.81
E_{T_4} (eV)	3.28	3.20	2.95	3.18	2.95
E_{S_1} (eV)	3.57	3.48	2.57	3.47	2.59
E_{S_2} (eV)	3.75	3.67	3.23	3.65	3.28
f_{S_1}	0.00	0.00	0.25	0.00	0.20
$\Delta E_{S_1-T_1}$	0.54	0.55	0.43	0.53	0.34
$\Delta E_{S_1-T_2}$	0.41	0.41	-0.08	0.39	-0.08

TABLE 3.3: Calculated vertical excitation energies at the stable TQB-TA and TQB-TB tautomers in the ground (S_0) and excited singlet (S_1) and triplet (T_1) states.

The zero oscillator strength of the S_1 at the Franck-Condon geometry means that the the lowest band in the absorption spectrum must gains intensity through vibronic mixing, indeed such vibronic structure is clearly observed in figure 3.2 show the absorption and emission spectrum calculated by sampling configurations using molecular dynamics. The calculated absorption spectrum shows very good agreement with the experimental spectrum. The vibronic transitions, like the experimental spectrum are separated by 0.14 eV, which corresponds to a timescale of $\sim$ 30 fs and originates

from motion associated with the proton transfer. Indeed, while the oscillator strength of the S_1 is zero at the TQB-TA geometry, as shown in Table 3.3, proton transfer, forming TQB-TB significantly increases this oscillator strength and therefore is this motion is responsible for making this transition allowed. It is interesting to note that this is unique among most TADF materials, as in many cases, the excited state motion making the S1 state reducing the energy gap between the singlet and triplet states, which makes the radiative rate smaller.

The emission spectrum also in very good agreement with the experimental spectrum recorded in toluene.[54] Interestingly, despite the rigidity of the molecule, the emission spectrum is rather broad, and this is because of the large effect the proton transfer has on modulating the gap between the ground and excited states. The calculated FWHM is 0.35 eV, which is close to the experimental value of 0.40 eV.

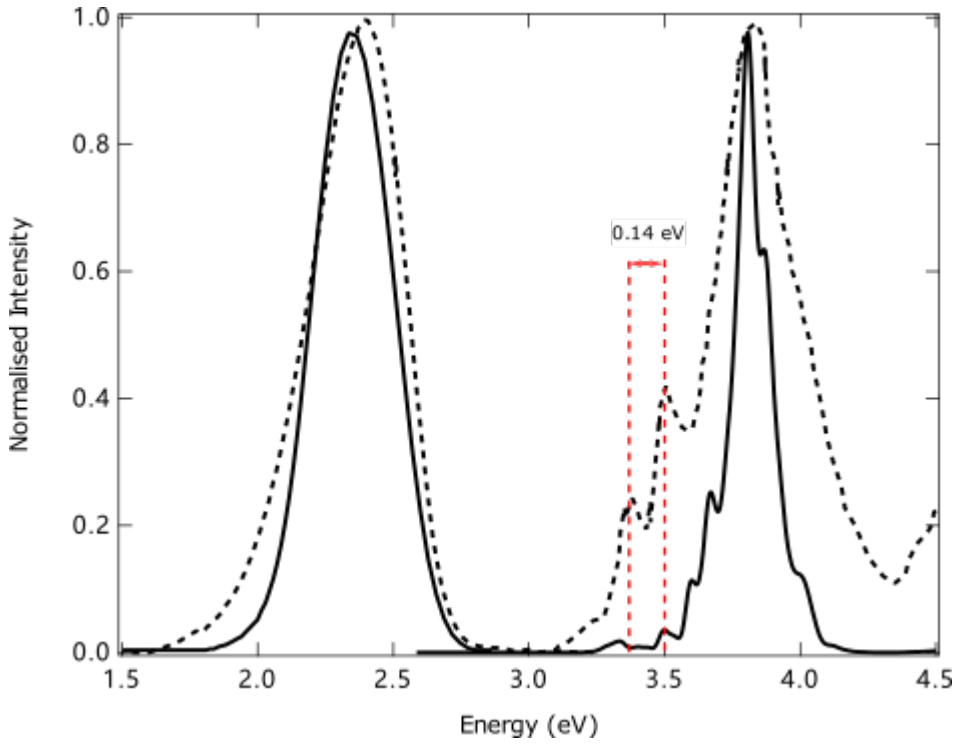

FIGURE 3.2: The experimental absorption and emission spectra (dashed)[54] compared to those calculated (solid) by sampling configurations using molecular dynamics simulations as described in the method section. The absorption spectrum has been shifted down by 0.1 eV overlap the main absorption peak and facilitate the comparison between the experimental and calculated spectra.

This calculated emission spectrum includes a state-specific PCM (SS-PCM) model. Here, both the S_1 and ground state were calculated within an S_1 optimised solvation structure, yielding the vertical emission energy including

the effect of slow solvation dynamics adjusting to the new dipole ($\sim 5D$) of the S_1 state. When the dielectric constant is changed to THF, and DMF as shown in ref [54] a stabilisation of the S_1 excited state by 0.06 and 0.12 eV, respectively, is observed. This is also in agreement with those observed experimentally.[54] Importantly, in the solid state, no shift in the emission is observed even for high polar hosts such as DPEPO. This is consistent with the amorphous guest-host film expected and the concepts of solid state solvation.[134]

Finally Table 3.4 shows the spin-orbit coupling matrix elements (SOCME) between the lowest singlet and triplet states. This crucial for the coupling between the singlet and triplet manifolds and therefore the triplet harvesting. At the TQB-TA structure, the SOCME are all very small and can be considered negligible, with the exception of $S_1 - T_1 = 1.2\ cm^{-1}$.

		T_2	T_3	T_4	S_1
TQB-TA(S_0)	T_1	0.002	0.004	1.017	1.198
	T_2	-	1.021	0.005	0.003
	T_3	-	-	0.004	0.006
	T_4	-	-	-	0.362
TQB-TB(S_1)	T_1	0.884	0.907	0.385	0.231
	T_2	-	0.343	0.513	0.796
	T_3	-	-	0.111	0.131
	T_4	-	-	-	0.023

TABLE 3.4: Calculated spin-orbit coupling matrix elements (SOCME) in cm^{-1} between the lowest singlet and triplet states. These were calculated using TDDFT(PBE0) at the optimised ground state of TQB-TA and optimised S1 state of TQB-TB.

However, upon proton transfer there is a notable increase for the coupling between all states except $S_1 - T_1$ which decreases to 0.231 cm^{-1}. This is because as shown in Figure 3.1, the S_1 and T_1 state at the TQB-TB geometry are very similar characters and therefore the change in spin cannot be compensated by a change in orbital angular momentum, meaning SOCME are close to zero. Importantly, these small couplings are the main source for the slow ISC rate and correspondingly slow triplet harvesting.

3.3.3 Excited State Dynamics

In ESIPT molecules, a hydrogen atom is covalently bonded to one atom and hydrogen bonded to a second in the same molecule. Photo-excitation changes the electronic structure and drives the switch so that the hydrogen becomes

bonded to the second atom and hydrogen bonded to the first. An important question is therefore what role, if any, does the proton transfer play in the triplet harvesting mechanism. Figure 3.3 shows the average and standard deviation of the O-H bond distance obtained from excited state molecular dynamics in the S_1 state from 20 different starting configurations. All show ultrafast proton transfer consistent with the very smooth potential surface previously reported. Indeed, proton transfer occurs within $\sim$ 20 fs, approximately one vibrational period. Small oscillations, with a similar period, corresponding in energy to the vibronic structure observed in the absorption spectrum and subsequently observed. However, despite these smaller scale vibrations, after the first 20 fs, the hydrogen remains localised in the TQB-TB form. This ultrafast dynamics would appear to suggest that the proton transfer has little role in the triplet harvesting mechanism which occurs on the ns-μs timescale.

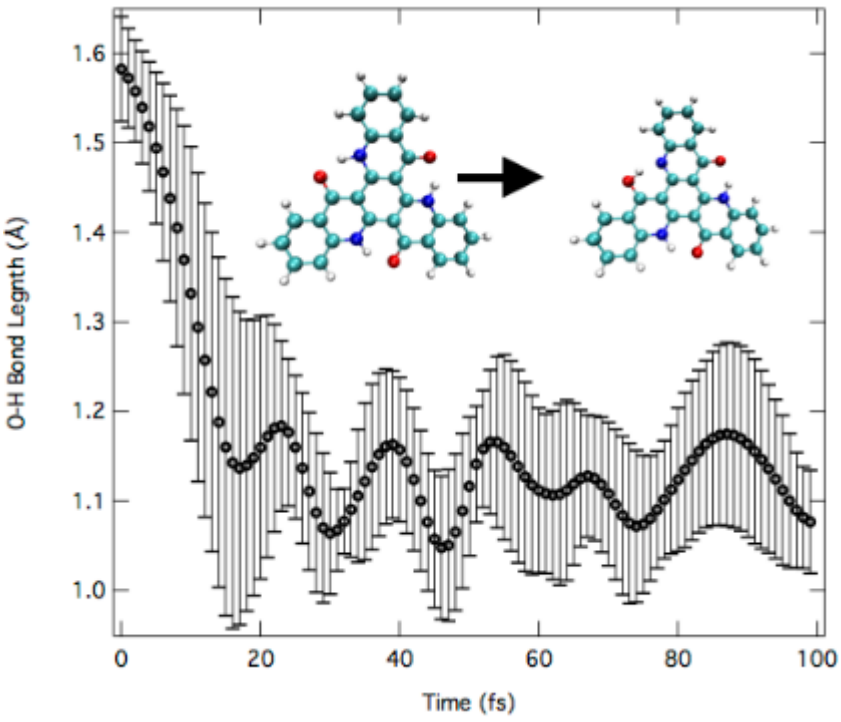

FIGURE 3.3: The average and standard deviation (error bars) of the O-H bond distance for the transferred proton obtained from 100 fs of excited state molecular dynamics in the S_1 state for 20 different starting configurations. Inset, snapshots of the structure before and after proton transfer.

However this dynamics only considers the singlet state and not the potential role of the triplets, important in the context of triplet harvesting. As shown in the previous works[116, 37, 117] multiple triplet states and the coupling between them can be important. To establish this, we develop a model

Hamiltonian to describe the dynamics in TQB. Figure 3.4 shows the 2 normal modes used for the model Hamiltonian, consistent with the changes in geometry shown in Table 3.1. The first, ν_1 corresponds to the motion of the proton between the oxygen and nitrogen atoms. The second normal mode, ν_{124} shows the angle change between the proton and the bonding atoms. Their respective ground and excited state potential energy surfaces are shown in Figure 3.5. The points are the quantum chemistry calculations and the lines are the fit of a 4^{th}-order vibronic coupling Hamiltonian to these points. It is from these fits that the parameters for the vibronic coupling Hamiltonian used in the quantum dynamics is used.

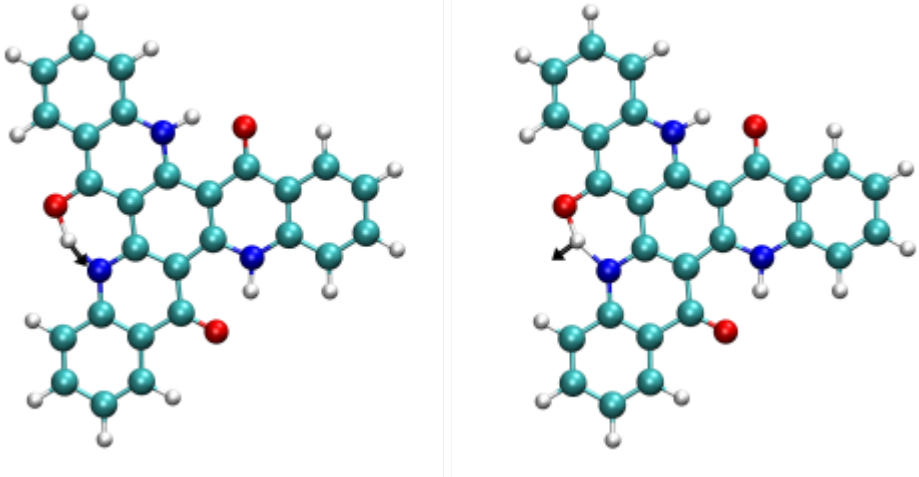

FIGURE 3.4: Schematic representations of the 2 dominant normal modes, ν_1 (left) and ν_{124} (right) used for the model Hamiltonian. The arrow represents the motion and corresponds to hydrogen motion responsible for the dominant structural changes associated with the proton transfer.

Along ν_1 the S_1 state shows a smooth transition from the TQB-TA to the TQB-TB conformer. In contrast the triplet states show a rather more complicated profile with multiple curve crossings between the lowest four triplet states. Indeed, this clearly shows a crossing between the diabatic T_1 and T_2 states which is responsible for not only the change in character of the adiabatic T_1 state along this mode, but also the barrier between the two TQB minima. This barrier is ~ 0.07 eV and is responsible for trapping some triplet population in the TQB-TA which becomes very relevant the context of triplet harvesting.

Along ν_{124}, the potential appears much simpler, with the excited state potentials slightly shifted with respect to the ground state. Consequently, upon excitation, this mode will drive a structural change leading to a decrease in the C-N-H consistent with the structural parameters reported in Table 3.1.

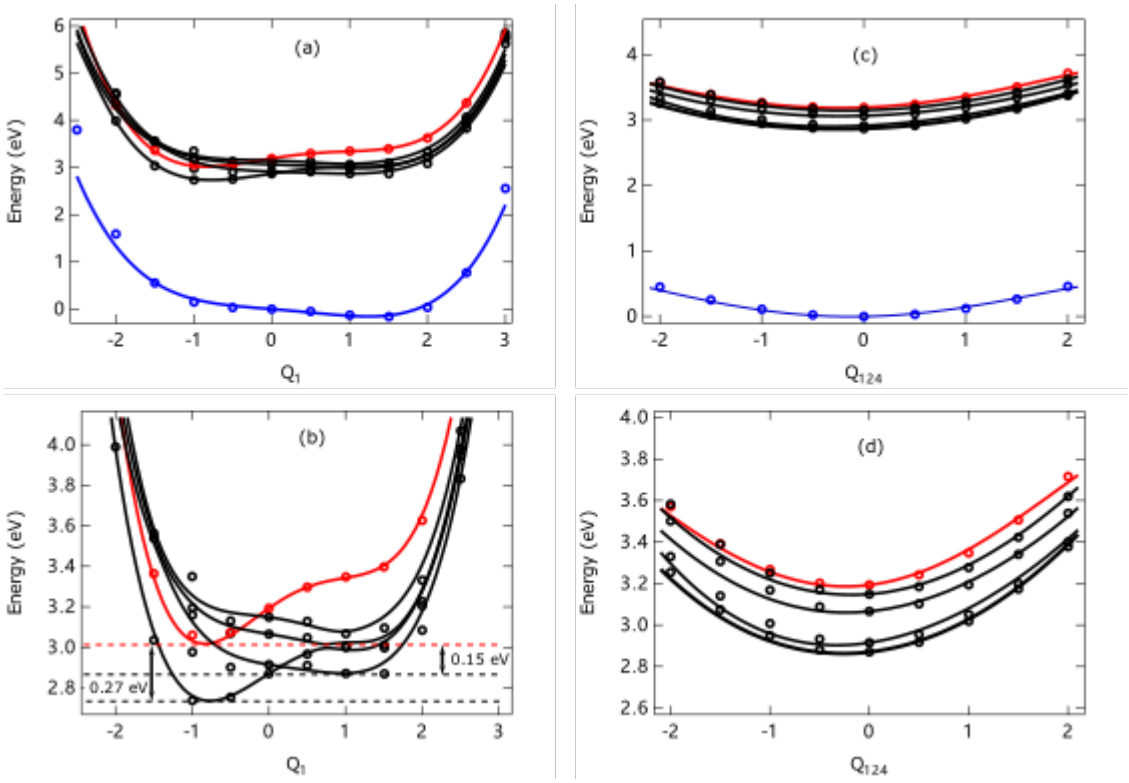

FIGURE 3.5: Cuts through the spin-free potential energy surface along (a) ν_1 and (c) ν_{124}. The dots are derived from the quantum chemistry calculations. The lines correspond to their fit from which the expansion coefficients of the diabatic vibronic coupling Hamiltonian are determined. (b) and (d) show a zoom into the excited state surfaces.

The parallel nature of the potential energy curves along this mode indicate that there is little or no non-adiabatic coupling. This mode can therefore be considered a tuning mode, in the sense that it purely changes the energy gap between the ground and excited states. ν_1 on the other hands exhibit large coupling, and is responsible for the mixing between the low lying triplet excited states.

To assess the validity of the model, in Figure 3.6 we simulate the absorption spectrum of TQB using the model Hamiltonian developed. In this case, as shown inset and described in the methods section, the spectrum is obtained by a Fourier transform of the autocorrelation function of the initial wavefunction in the ground state and the wavefunction at time, t. The resulting spectrum compares very well the spectrum recorded experimentally with the vibronic transitions, associated with the proton transfer clearly visible. Interestingly the width of the experimental spectrum is reproduced using a damping factor on the autocorrelation function of 20 fs. This is to say that after 20 fs, the excited state wavefunction does not overlap spatially with

the ground state wavefunction. This is consistent with the proton transfer dynamics observed in Figure 3.3 in which after the initial proton transfer the wavepacket in the S_1 state becomes localised in the S_1 minimum.

Having established the accuracy of the model, and figure 3.7 shows the excited state dynamics perform. Figure 3.7a shows the expectation value of the wavepacket along ν_1. The wavepacket initially starts in the TQB-TA form, and quickly decays into the TQB-TB form, which has a minimum at $Q = -0.8$ as shown in Figure 3.5. This initial proton transfer occurs in 11 fs, which is slightly faster than the 20 fs seen from the MD, which can be expected from the reduced coordinate space model represented. Oscillations with a period of 25 fs continue after this initial dynamics as the system begins to relax into the TQB-TB minimum. Complete relaxation does not occur in the present simulations as there are not many modes, again due to the reduced coordinate space model, which means energy cannot be transferred to the remaining degrees of freedom of the model.

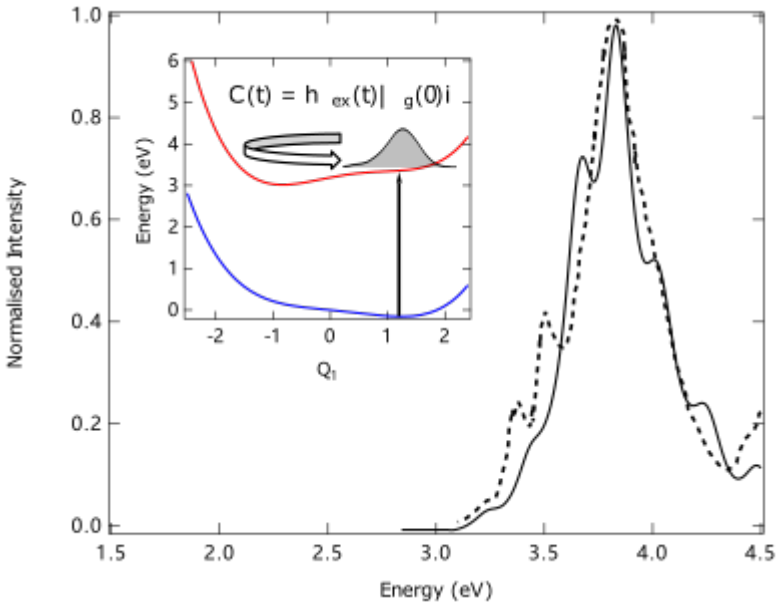

FIGURE 3.6: Experimental (dashed)[54] and theoretical (solid) absorption spectrum. The latter has been calculated using the Fourier Transform of the autocorrelation function of the initial wavefunction as described in the method section and illustrated inset.

Figure 3.7b shows the population of the triplet states during the first 3.5 ps after initial excitation. While the population remains small within this timescale, a clear consistent rise is observed and corresponds to a ISC rate of $4 \times 10^7 s^{-1}$. This is in good agreement with the rate reported experimentally[54] and consitent with the small SOCME calculated. As shown inset

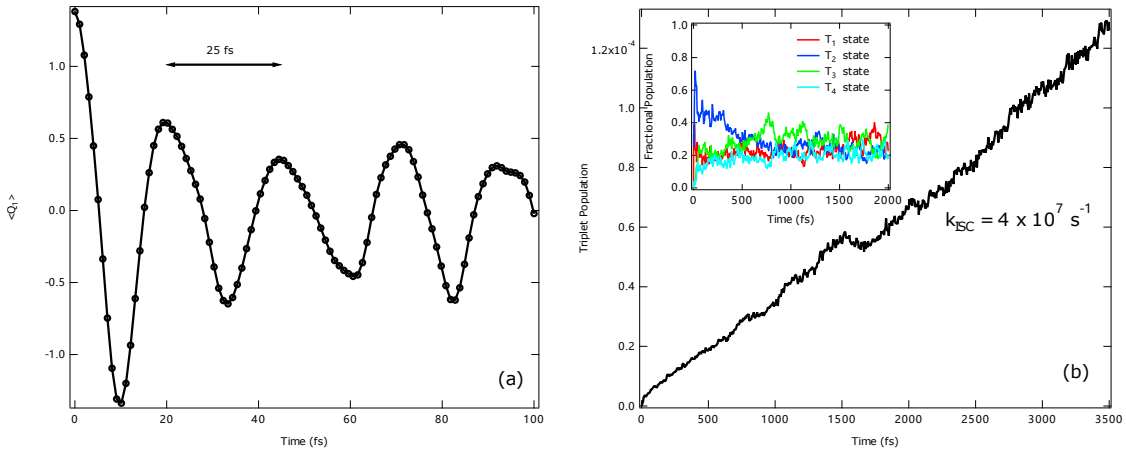

FIGURE 3.7: (a)The total fractional population of the triplet states during the first 3.0 ps after initial excitation into the minimum on the S_1 state (TQB-TB).(b)The fractional population distribution among the triplet states from the dynamics in panel a illustrating that although initially the T_2 is populated, the wave function is distributed throughout all of the triplet states within 500 fs.

from the fractional population of the triplet states, the T_2 is initially populated. This can be expected since at the TQB-TB geometry it has both the largest *SOC* to the S_1 state as is close to degenerate. After the strong coupling between the triplet states, within 500 fs, this has been distributed throughout all of the triplet states. This equilibrium will persist until vibrational cooling at longer times, as pervasively state is not captured in our model.

3.3.4 Mechanism of Triplet Harvesting

In the previous section, we have shown that the rate of intersystem crossing (ISC) is relatively slow, consistent with the experimental conclusions in ref[54] In addition the large energy gap between the singlet and triplet states means that the rate of rISC is very slow, $\sim 10^3 s^{-1}$, which similar to typical non-radiative decay rates from triplet states. Despite this the external quantum efficiencies (EQE) reported show a high degree of triplet harvesting. EQE is defined as:

$$EQE = \chi \cdot \eta_r \cdot \eta_{out} \cdot \phi \tag{3.5}$$

where χ is exciton harvesting efficiency, η_r is the recombination efficiency, assume to be 1, η_{out} is the light outcoupling assumed to be 0.3 and ϕ is the quantum yield. Given $\phi = 0.55$ for TQB in CzSi, the exciton harvesting efficiency must be $\sim$0.85 to achieve the reported EQE. Consequently, given that

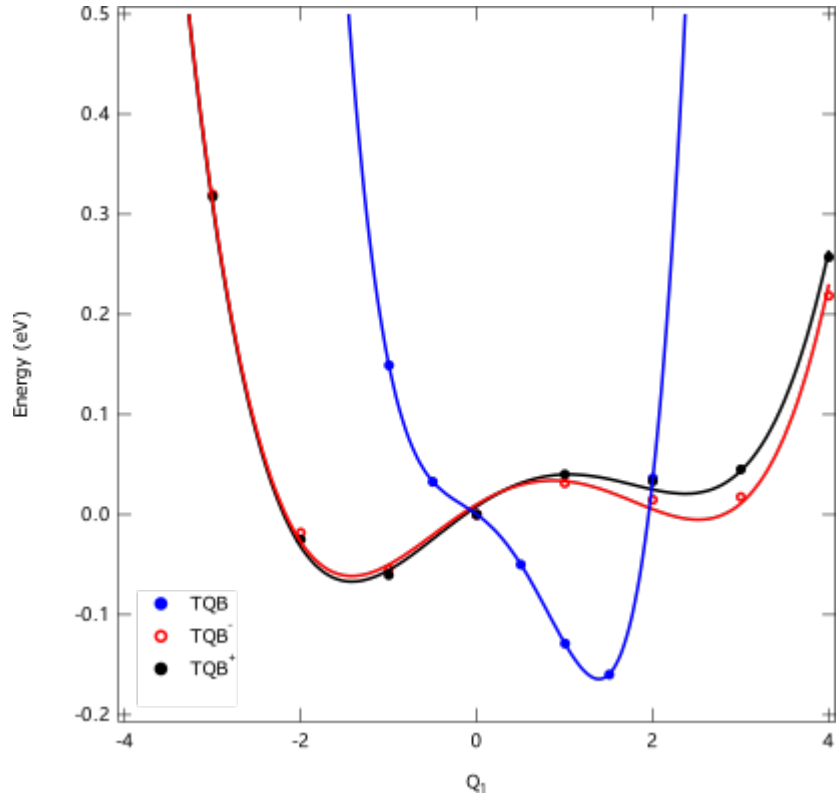

FIGURE 3.8: Ground state potential energy surface and corresponding fits along ν_1 for the neutral (blue), cationic (black) and anionic (red) states of TQB.

0.25 corresponds to singlet excitons, at least 80% of the triplet excitons must be harvested to achieve these external quantum efficiencies.

Under electrical excitation, Mamada et al.[54] assumed that the triplet excitons would be most likely to form directly on TQB-TA by charge carrier recombination. However, Figure 3.8 shows the potential energy surface along ν_1 for the neutral, cationic and anionic form of TQB. While the neutral form favours TQB-TA, the lowest energy conformer for both charged forms is TQB-TB. There is a barrier between the two forms, especially for the anionic case, however the minimum geometry of neutral TQB is close to the transition state between the two forms in the charged cases and consequently, charge trapping would provide sufficient energy to overcome this. Consequently, a significant fraction of the exciton generate can be considered to occurring in the TQB-TB form.

This would appear to favour exciton generation in the TQB-TB, which would appear unfavourable for triplet harvesting due to the large between the T_1 and S_1 states at this geometry. However, crucially the minimum of both the anion and cationic forms of TQB-TB is distorted from the the TQB-TB excited state minimum. Consequently, upon charge recombination the exciton will be generated upon a higher energy region of the excited potential

energy surface, ∼3.6 eV. This will provide sufficient energy for the excited wavepacket to traverse the proton transfer coordinate.

To assess the effect of these initial conditions on the dynamics in the triplet states, we use the previously developed model Hamiltonian. However, first of all it is important to assess how the wavefunction should be excited. A TD-DFT wavefunction for state n is written:

$$\Psi_n = \sum_{i}^{occ} \sum_{r}^{unocc} C_i^r \Phi_i^r \tag{3.6}$$

where Φ_i^r represents the electronic configuration of a single-electron excitation from occupied orbital i to vacant orbital r, and C_i^r represents the its weight in forming excited state Ψ_n. Consequently, under the assumption that charge recombination creates a $HOMO$ and $LUMO$ excitation, the weight of this transition to each Ψ_n state can be used to approximate the distribution of excited states formed upon the charge recombination. At both the anionic and cation TQB minimum energy geometries, the $HOMO \rightarrow LUMO$ transition corresponds to the character of the T_1 state and consequently the initial state is assume to be purely in the T_1 state.

Figure 3.8 shows the fraction of the wavepacket in the triplet states in the TQB-TA form obtained from quantum dynamics simulations during which the initial wavepacket was placed in the lowest triplet(T_1) state. The black trace shows the dynamics when initialised from the $TQB - TB^{+/-}$ geometry, i.e $Q_1 = -1.6$ and the red trace shows the dynamics in the $TQBTA^{+/-}$ geometry when $Q_1 = 2.1$. This shows that $\sim$ 20% of the excited state wavefunction in the triplet state exists in the TQB-TA form, while the smaller fraction, as one would expect for the higher energy state, this is a sizeable fraction and is consistent with previous work in ESIPT.[135, 136] Figure 3.9 shows the energy of the triplet states of the hosts compared to the triplet states of the TQB-TA and TQB-TB structures. The hosts which give higher device performance[137], namely CzSi or PPT host are capable of combing the triplet states in both forms, while the lower performing devices are only capable of confining the triplets in the lower energy TQB-TB form. The exception to this is DPEPO, which has a very high T_1 energy, however in ref [138] its poor performance was attributed to the poor charge carrier transport capabilities and deep HOMO and shallow $LUMO$ energy levels of $DPEPO$.

With these results, we propose the following. Given that $EQE = \chi \cdot \eta_r \cdot \eta_{out} \cdot \phi$, and taking constants $\phi = 0.55$ in CzSi and $\phi = 0.41$ in CBP and $\eta_{out} = 0.3$. For devices in CBP, only triplet states in the TQB-TB form can

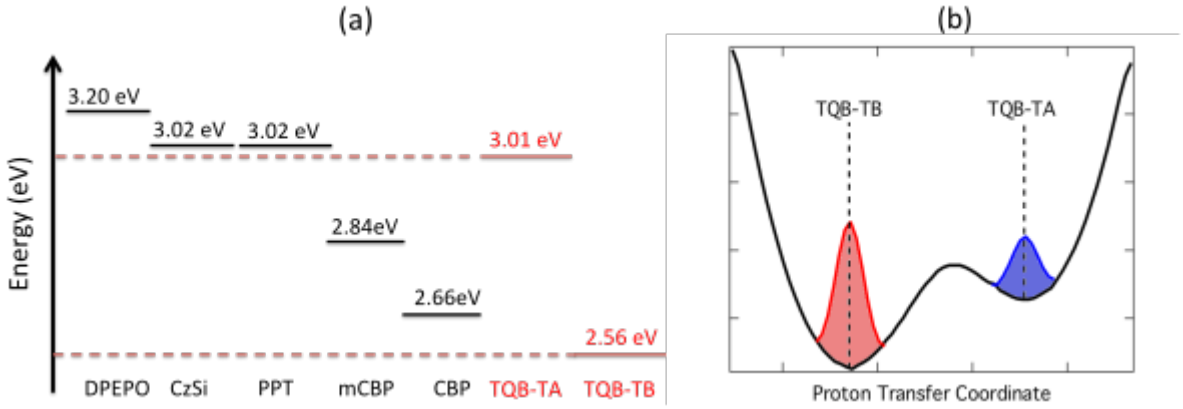

FIGURE 3.9: (a) The T_1 energies of the 5 host materials, PPT, DPEPO, CzSi, mCBP, CBP with the T_1 energy of TQB in the TQB-TA and TQB-TB forms. (b) Schematic of the trapping mechanism.

be harvested. Given the large energy gap, ∼0.27 eV, this is unlikely to be possible using TADF. Instead Mordzinski et al [139]. reported that in ESIPT molecules under high triplet-state concentrations the excited state decay is mainly governed by triplet-triplet annihilation (TTA). Although Mamada et al.[54] used laser power dependence to rule out TTA, this was for photoexcited sample and the concentration of triplet states is owing to the slow rate of ISC. Assuming 80% of the wavepacket in the TQB-TB form are only harvested through TTA, the triplet harvesting efficiency is $\sim$ 0.4, yielding an $EQE = 6.7\%$ in agreement with the device in CBP. In contrast, if the additional 0.2 of the excited triplet wavepacket is harvested by TADF, the $EQE = 12.4\%$ close to that of CzSi. While this is a qualitative analysis, it remains consistent with experiment results and provides an interpretation that can explain both the high EQE's and the importance of the host material used to achieve them.

3.4 Conclusion

Diversifying the molecular designs for achieving TADF materials is crucial not only to obtain high performance stable TADF emitters, but also for shedding more light onto the mechanism of TADF, especially the differences between photo and electrical excitation important when moving to devices. In the present work we have used quantum chemistry, molecular and quantum dynamics simulations to understanding the triplet harvesting mechanism in based upon excited state intramolecular proton transfer (ESIPT) using TQB.[54]

Our simulations have shown that proton transfer is ultrafast occurring along a barrierless potential energy surface. Interestingly, in contrast to most TADF emitters based upon D-A structures, the structural reorganisation associated with the excited state changes leads to an increase in the S_1 radiative rate, despite the generation of a state exhibiting CT character. This ultrafast nature of the proton transfer suggests it plays little role in triplet harvesting which occurs on the nano- micro-second timescale. However, the lowest triplet state changes character along the proton transfer coordinate, creating a barrier, $\sim$0.07 eV, which is able to trap the wavepacket in both the TQB-TA and TQB-TB forms. For the former, the energy gap to the singlet state of TQB-TB is $\sim$0.15 eV in agreement with the activation energy reported for TADF. However the triplet state in the TQB-TB has a large energy barrier, $\sim$0.27 eV making triplet harvesting via TADF inefficient. In this case, due to the high triplet-state concentrations in the OLED, we propose that these states are harvested through TTA, yielding an expected EQE which agrees with ref.[54] TTA is not observed in the case of photo-excitation due to the low quantum yield of triplet states which arises from the small ISC rate.

This highlights that TADF operating alongside TTA, previously also seen in other systems[140, 32, 141], can provide an efficient route for higher efficiency devices. It should be noted that for the TTA, the luminance is known to increase more than linearly with an increase in current density[142]. This is absent in ref.[54] and therefore could test the proposed mechanism.

Chapter 4

Quantum Tunnelling

4.1 Introduction

The acridone-based compound, triquinolonobenzene (TQB) discussed in the previous chapter, was designed to exploit intramolecular proton transfer to separate the highest occupied and lowest unoccupied molecular orbitals, endowing thermally activated delayed fluorescence (TADF) properties onto the emission characteristics of this rigid and planar molecule. This system has the advantage of overcoming the limits imposed by the twisted donor-acceptor structures traditionally used to achieve an effective HOMO-LUMO separation and opens up molecule design to the large variety of π-conjugated aromatics. However, the potential versatility of this molecular design still needs to be investigated more deeply to understand the all the factors affecting TADF in ESIPT molecules.

The previous chapter, published in ref [143], outlined the importance of the the proton transfer coordinate on the TADF properties. It also identified the potential for an equilibrium between low lying triplet states for achieving efficient TADF. These conclusions were recently supported by experimental work performed by Long *et al.*[144]. Here the authors concluded that after photoexcitation and rapid ESIPT, emission from S_1 is found to compete with thermally activated ISC to an upper triplet state, T_2, very close in energy to S_1 and limiting photoluminescence quantum yield. T_2 slowly decays to the lowest triplet state, T_1, via internal conversion. The measurements demonstrated that rISC in TQB occurs from T_2 to S_1 driven by thermally activated reverse internal conversion from T_1 to T_2.

Understanding whether tunneling influences the equilibrium in the context of TADF is important because it can have a significant impact on the optimization of TADF materials and devices. Firstly, in TADF-based organic

materials used in OLEDs achieving a high rate of reverse intersystem crossing (RISC) is crucial for efficient triplet-to-singlet exciton upconversion. Tunneling processes can affect the rate of RISC[145], which, in turn, influences the overall efficiency and performance of TADF devices. Secondly, Tunneling can influence the energy transfer between molecular states. Understanding its impact on the energy landscape is essential for designing materials with the desired energy levels, which is critical for TADF applications.In summary, comprehending the influence of tunneling on the equilibrium between singlet and triplet states is essential for maximizing the efficiency and performance of TADF materials and devices.[146]

However this raises a key question, *does quantum mechanical tunnelling in the triplet manifold play a crucial role in controlling the rISC probability and rate in TQB?* Indeed, the importance of the proton transfer coordinate means that tunnelling could significantly alter the rate and probability of rISC and understanding this is the focus of this present chapter.

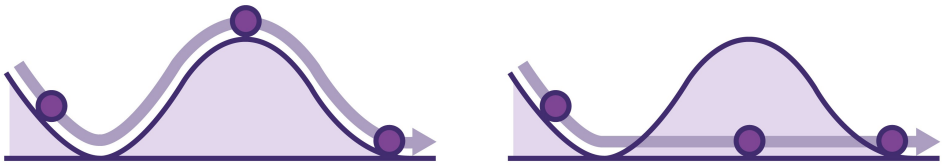

FIGURE 4.1: A schematic comparison of a classical over-the-barrier motion (left) with through the barrier motion of quantum tunnelling (right).

Figure 4.1 show a schematic comparison of a classical over-the-barrier motion (left) with through the barrier motion of quantum tunnelling (right) [147]. The classical motion of a classical particle over a potential barrier is as we would expect, *i.e.* the particle can only over the barrier if it has sufficient energy to overcome it. Tunneling is a quantum mechanical phenomenon when a particle is able to penetrate through a potential energy barrier that is higher in energy than the particle's energy. This amazing property of microscopic particles play important roles in explaining several physical phenomena including the development of Scanning Tunneling Microscope (STM) which had a profound impact on chemical, biological and material science research. In the context of the present work, we wish to understand if tunnelling influences the equilibrium that exists between the T_1 and T_2 states in TQB and therefore affects its ability to undergo rISC.

4.2 Methods

4.2.1 Quantum Dynamics Simulations

The quantum dynamics addressing the tunnelling in TQB were performed using the Heidelberg Multi Configuration Time Dependent Hartree (MCTDH) package [148, 149]. In this approach the wavefunction *ansatz* is written as a linear combination of Hartree products 2.50.

To address this we perform simulations within a density operator formalism of MCTDH [150]. Here the single particle functions are replaced with single-particle density operators. Here we adopt a closed quantum system, this is to say that no dissipative operators are included and only the core Hamiltonian described above is used. In this representation the Liouville-von Neumann equation for the system is expressed:

$$\dot{\rho}(t) = -i\hbar[H, \rho(t)] \tag{4.1}$$

For these simulations, the advantage of MCTDH comes into its own. Although the model Hamiltonian used herein is relatively small, for the density operator simulations the dimensionality of the system formally doubles [151] significantly increasing the numerical treatment of the simulations.

Throughout this chapter, the model Hamiltonian contained 2 vibrational degrees of freedom, ν_1 and ν_{124} corresponding to those used in the previous chapter. Throughout only one electronic state, the T_1 state was included in the Hamiltonian and the wavefunction along this mode was described in 5 SPFs. The potential along ν_1 is represented using a Fast Fourier Transfer (FFT) grid with 128 grid points, while ν_{124} also represented using a FFT grid with 41 grid points. In all cases this ensured convergence.

4.2.2 Quantum Chemistry and Molecular Dynamics

Ab initio molecular dynamics (MD) of TQB in its excited singlet (S_1) state and TQB-TA and TQB-TB structures of the lowest excited triplet state (T_1) were performed using the Terachem package.[125, 126] The potential energy and forces was calculated using DFT(PBE0) and a 3-21g[152, 153, 154, 155, 156, 157] basis set. The effect of the environment was included using a conductor-like polarizable continuum model[123] using the dielectric constant of toluene.

50 configurations from each MD were used to simulate the emission spectra. The total emission spectrum was generated by summing the contributions of each spectrum for which the oscillator strength had been broadened by a Gaussian function of full width half maximum of 0.05 eV. These were sampled using linear response time-dependent density functional theory (LR-TDDFT) within the Tamm-Damcoff approximation[118] and the PBE0 exchange and correlation functional[119][120] as implemented with the ADF quantum chemistry package. Spin-orbit coupling, within the ZORA approximation was also included to obtained the oscillator strengths and therefore phosphorescence rates of the triplet states.

4.3 Results

4.3.1 The Reaction Coordinate and Emission

Figure 4.2 shows the potential energy of the lowest singlet and triplet state along the proton transfer coordinate. The lowest triplet state, black line, shows the two minima associated with TQB-TA and TQB-TB which correspond to prior and after proton transfer, respectively. This plot also shows the fluorescence and phosphorescence rates calculated at the optimised quantum chemistry geometries. These are in good agreement with the rates determined experimentally [144] as are the (reverse) inter-system crossing rate which are those calculated in the previous chapter.

Here it is important to note a key element in this discussion, namely the difference between the adiabatic and diabatic representations. Figure 4.2 show the adiabatic T_1 potential along the proton transfer coordinate, but importantly the character of the state along this coordinate changes. Recently, Long *et al.* [144] identified an equilibrium between two triplet states, but this could be two different diabatic states (*i.e.* two minima of different character), not necessarily higher lying excited states than those shown in Figure 4.2. This difference in the two representations plays an important role in the remainder of this chapter.

To benchmark the theory, Figure 4.3 shows the experimental fluorescence (red dashed), phosphorescence (black dashed) compared to the corresponding calculated spectra. For the triplet state, the emission from both the TQB-TA (green) TQB-TB (black) forms are calculated. It is noted that although the former, TQB-TA, is higher in energy, its rate as shown in Figure 4.2, is also

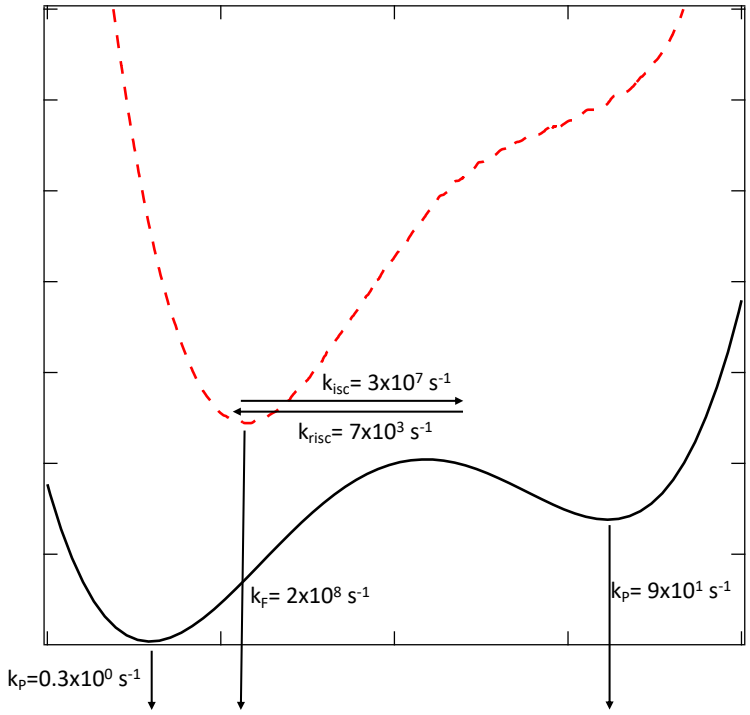

FIGURE 4.2: Lowest singlet (red) and triplet (black) potential energy and rates in different configurations followed by the coordinates has been represent in this figure. k_P stands for the rate of phosphorescence, k_F is for the rate of fluorescence, k_{ISC} and k_{rISC} are for rate of inter-system crossing and reverse inter-system crossing.

2 orders of magnitude smaller. The fluorescence and phosphorescence spectra are in excellent agreement with the experimental spectra. Experimentally, the latter (phosphorescence spectrum) could only be recorded in zeonex at 80 K as the radiative rate is very small due to the weak spin orbit coupling and large energy gap between the singlet and triplet states at this configuration. Here, there is a slight high energy tail, between 2.5-3.0 eV, which could contain contributions from the higher TQB-TA form, but the low temperature means that the majority of the system is relaxed into the low TQB-TB form. At higher temperatures no phosphorescence observed because TADF is the preferred emission route due to the small rates of phosphorescence.

While the steady state phosphorescence spectra does not show any definitive evidence of an equilibrium between the TQB-TA and TQB-TB forms in the lowest triplet state, time-resolved experiments may be able to shed this insight. Figure 4.4 shows time-resoled emission of TQB in DPEPO recorded at 300K (top) and 80K (bottom). The short time ($<10^{-7}$ s) corresponds to fluorescence at longer times ($>10^{-7}$ s) the emission is dominated by phosphorescence. Here it is clear that while a significant component occurs at short

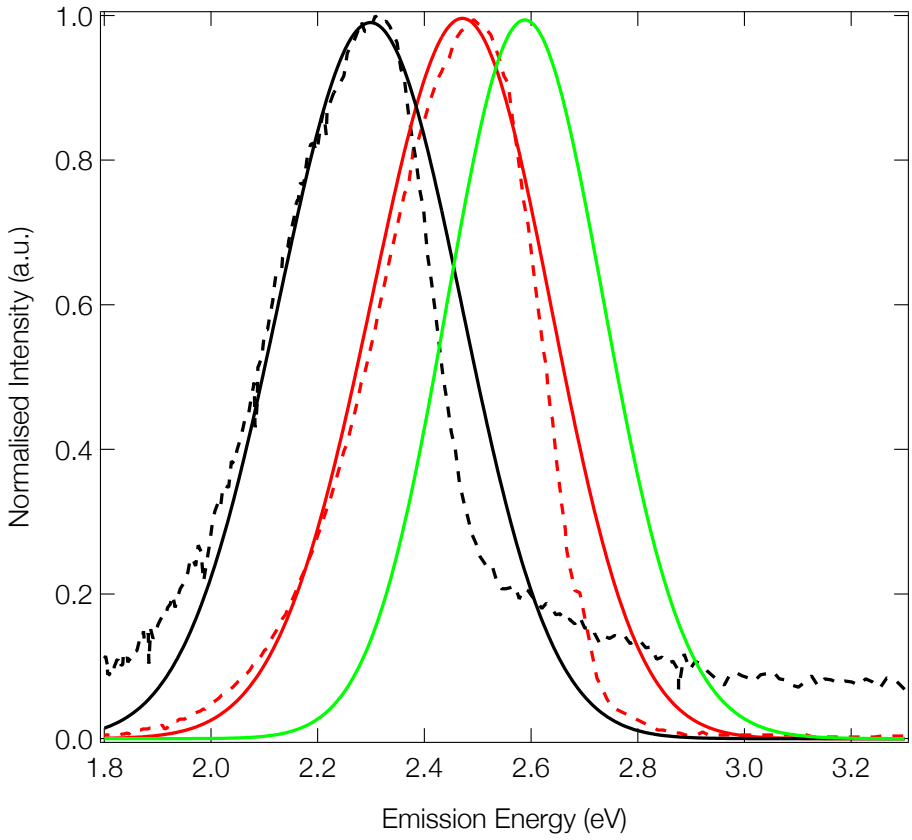

FIGURE 4.3: Experimental emission spectra shows as, fluorescence (red dashed), phosphorescence (black dashed) and calculated fluorescence spectrum for TQB-TB (red) and the phosphorescence spectra of TQB-TA (green) TQB-TB (black).

wavelengths than the fluorescence there is definitely components which appear at shorter wavelengths (high energies) consistent with emission from the TQB-TA form. This appears at around 10^{-3}s in both cases (note the different time axis for each plot in Figure 4.4). From this we estimate weak emission bands ~530 nm and 480 nm which are agreed with the peaks phosphorescence spectra of TQB-TA, 2.7 eV and TB 2.3 eV in Figure 4.3.

Finally, ref. [144] also uses transient absorption spectroscopy to understand the interplay between the excited states observed. From this the authors identified two distinct bands, labelled PA2 and PA3 occurring at 1.65 eV and 1.85 eV, respectively. The two are clearly linked as intensity is transferred between the two bands throughout the excited state dynamics. Indeed, PA2 and PA3 initially grow rapidly after photoexcitation, and at later times, PA2 continues to grow while the contribution from PA3 becomes relatively smaller. These were identified as triplet-triplet adsorptions by noting that they are rapidly quenched in the presence of oxygen. Ultimately, these bands were used to describe an equilibrium between a T_1 and T_2 state for the

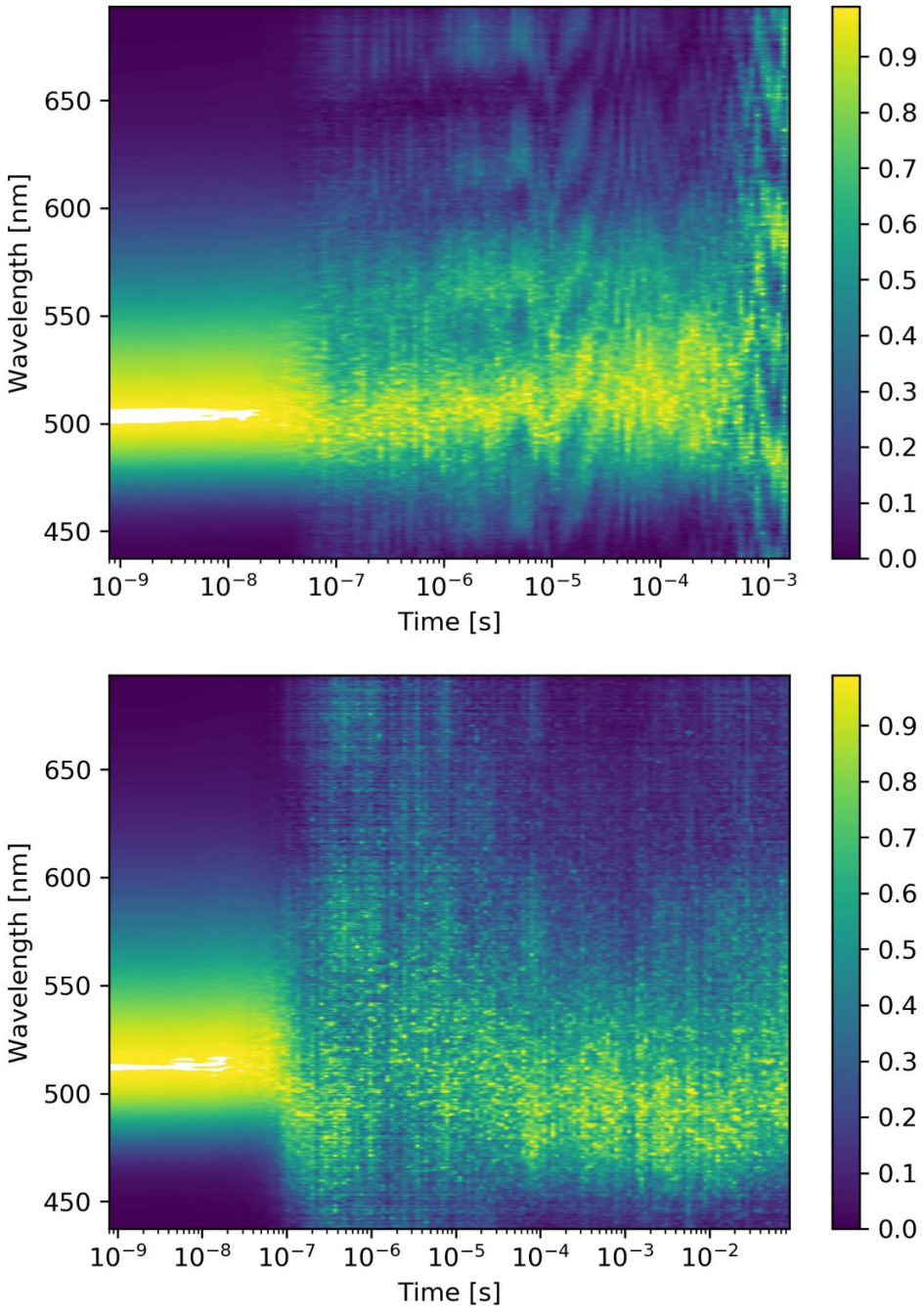

FIGURE 4.4: Normalised time-resolved emission spectra of TQB in DPEPO at 300K (top) and 80K (bottom). The emission bandshape and onset do not vary over the timescales investigated (ns-ms). Figure reproduced from ref. [144]

TADF mechanism.

To understand these, Figure 4.5 shows excited state transitions between triplet states possible in the TQB-TA and TQB-TB states. Only the dominant transition with non-zero oscillator strengths are shown and this clearly highlights transitions which closely match the PA2 and PA3 features found in the

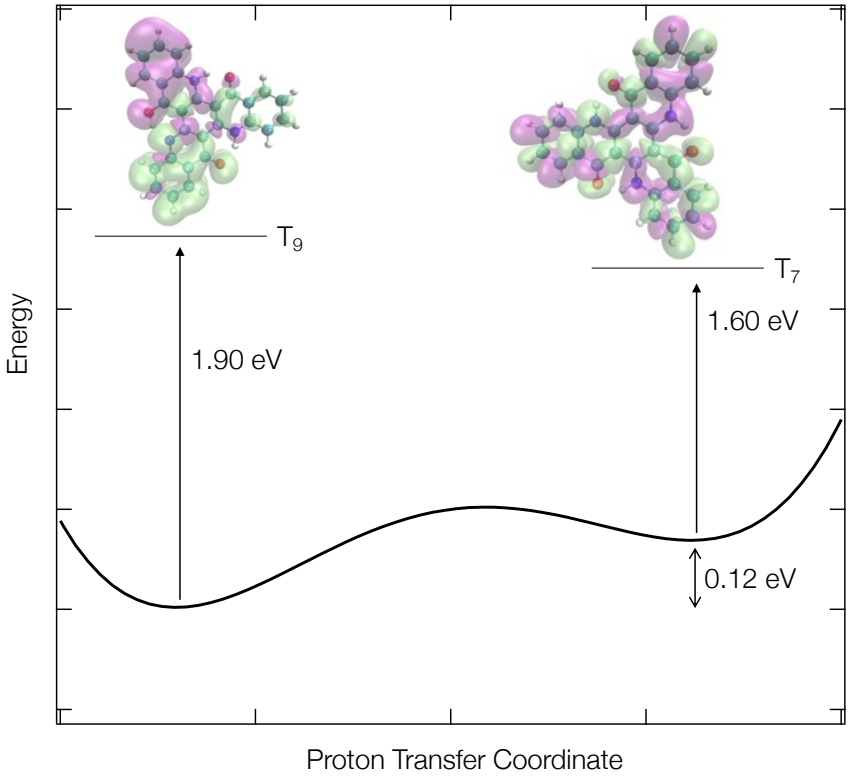

FIGURE 4.5: High lying states energies in different configuration for TQB-TB. Temperature will help overcome the barrier and those states will be the intermediate states.

transient absorption. This shows that PA3 is likely to arise from transient excitation of molecules in the TQB-TA form, while PA2 will arise from transient excitation of molecules in the TQB-TB form. This fits the kinetics that as TADF occurs, PA3 (*i.e.* TQB-TB) will eventually decay with population transferring to TQB-TA in the triplet manifold before going to the S_1 state. These experimental results combined with the simulations clearly confirm an equilibrium between the two lowest energy forms of TQB *i.e. TQB-TA and TQB-TB*. The remaining question is the role of tunnelling in controlling the position of the equilibrium.

4.3.2 Quantum Dynamics of Tunnelling

Figure 4.6 left shows the population of the triplet state along proton transfer coordinate. Here a step function has been applied at the peak of the potential to determine the fraction of the wavefunction aligning with the TQB-TA and TB formed. The population plotted corresponds to the long time limit when equilibrium has been formed between the two forms.

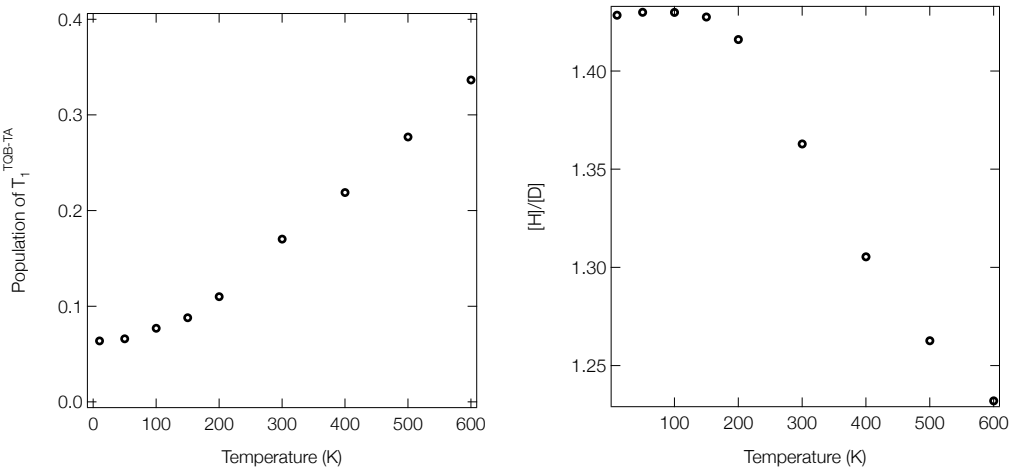

FIGURE 4.6: Left has shown that the population of lowest triplet state of TQB-TA changed following by the temperature, which indicates that the low temperature changes the equilibrium; Right shows the ratio of amount of the wavepacket for TQB-TA form when it's hydrogen and the amount when it's deuterium. Larger value indicates more hydrogen, so more possibility of tunneling there is. And it's decreasing with temperature as there is energy energy in system to overcome the barrier, so the tunneling is less important.

Figure 4.6 left shows that when the simulations are initiated in the TQB-TB form, even at very low temperature, there is a significant population transfer ($\sim$10%) into the TQB-TA form. Given the energy is not enough to overcome the barrier, this can only arise from tunnelling. As temperature increases, the population in the TQB-TA form increases as one would expect, and given the height of the barrier ($\sim$0.2 eV) a significant fraction of this must still arise from tunnelling. This is further confirmed in Figure 4.6 right shows the influence on the TQB-TA population of swapping hydrogen for deuterium, *i.e.* the kinetic isotope effect. As temperature increases, the ratio gets close to 1, indicating a reduced role of tunneling, but at low temperatures, up to about 300 K, the ratio between hydrogen and deuterium clearly shows the influence of tunnelling.

This insight of the equilibrium between the TQB-TA and TQB-TB forms can now be used to estimate the rISC rates. In previous work, k_{ISC} was calculated as 3×10^7 s^{-1}, using a ΔE_{ST}=0.18 eV reported in ref. [143] and confirmed in ref. [144] and the equation below:

$$k_{rISC} = \frac{1}{3}k_{ISC}\exp(-\Delta E_{ST}/k_BT) \tag{4.2}$$

yields k_{rISC}=7×10^3 s^{-1}. This was consistent with previous experiments in ref. [54], but does not take into account the equilibrium between the TQB-TA and TQB-TB forms and the influence this may have on k_{rISC}. Indeed, the majority of the system will relax into the TQB-TB form of the triplet state, for which ΔE_{ST}=0.30 eV at this geometry.

Consequently, beginning from the relaxed T_1 TQB-TB state a more complete description of k_{rISC} is written:

$$k_{rISC} = \frac{1}{3}Kk_{ISC}\exp(-\Delta E_{ST}/k_BT) \tag{4.3}$$

where

$$K = \frac{T_1^{TQB-TA}}{T_1^{TQB-TB}} = \exp(-\Delta E/k_BT) \tag{4.4}$$

This includes equilibrium between the TQB-TA and TQB-TB forms and assuming a Boltzmann distribution and using the energy gap between the singlet and triplet states of 0.12 eV we find:

$$K = \exp(-0.12/0.025) = 0.009 \tag{4.5}$$

which when combined with Equation 2 yields a k_{rISC}=6.3×10^1 s^{-1}, considerably different from the experimentally reported value. However, while taking into account the equilibrium between the TQB-TA and TQB-TB forms, it completely ignores tunnelling. Consequently, in contrast, if the equilibrium constant is derived from Figure 4.6 upper at 300 K, $K = 0.18/0.82 = 0.22$ and therefore the k_{rISC}=1.5×10^3 s^{-1}, close to the experimentally reported value of 3.5×10^3 s^{-1}. This above analysis, combined with the quantum dynamics and previous experiments [144] confirm the important role that tunnelling plays in generating an equilibrium between the TQB-TA and TQB-TB forms. This equilibrium supports the rISC from the triplet state of the TQB-TA form and is therefore vital for TADF.

4.4 Conclusion

This chapter builds upon previous work in Chapter 3 and experimental work outlined in ref. [144], with the key objective attempting to understand the role that tunnelling plays in controlling the TADF mechanism of TQB.

Our quantum chemistry calculations, alongside the recent experimental observations provide strong evidence for the presence of two triplet states in equilibrium. These correspond to the TQB-TA and TQB-TB forms. Given the role of the proton transfer coordinate in switching between these two forms, we have investigated the role of tunnelling in controlling this equilibrium.

Our quantum dynamics and subsequent analysis demonstrates that tunnelling plays a key role in controlling the equilibrium between the TQB-TA and TQB-TB forms, which ultimately determined the rate of rISC. This highlights that TADF operating alongside quantum tunnelling can provide an efficient route for higher efficiency devices. With this deep understanding of the mechanism of TQB obtained it is now possible to use this to design new highly efficient molecules.

Chapter 5

Towards Understanding Exciton Generation in OLEDs

5.1 Introduction

Thermally activated delayed fluorescence (TADF) can be used to enhance the efficiency of OLEDs by harvesting the non-emissive excited triplet states which are generated upon electrical excitation.The potential in these materials has led to a significant amount of research which has focused upon understanding the complex photophysics of TADF materials[32]. While this gives important insights into the nature and mechanism of TADF, it should be noted that the way excited states are formed in molecules by interaction with light or electrically, as in the case of an operating OLED, may give rise to distinctly different behaviour. Consequently, understanding how excitons are generated under electrical excitation is a crucial area of research.

To understand the mechanism, there are two ways to think. Firstly, excitons formed on the host [158, 159], then transferred to the guest through Förster[160] and Dexter[161] mechanisms. But this is not favourable, because the triplet states it generates are free to diffuse leading to a big influence from quenching effects. [162]. In the second case, the electrons and holes trapped on the emitter and generated the excited state. Upon this, electron and hole are transporting either together or separately is unclear. Crucially, which charge arrives first may make a big influence.

In Chapter 3, after understanding the excited state dynamics of the ESIPT TADF molecule, TQB, I introduced an interesting result that the triplet state in TQB-TB form has a large energy barrier, so the triplet harvesting is inefficient in high device performance and we think it could be harvested by TTA. Indeed, in their original work, under electrical excitation, Mamada *et al.* [54]

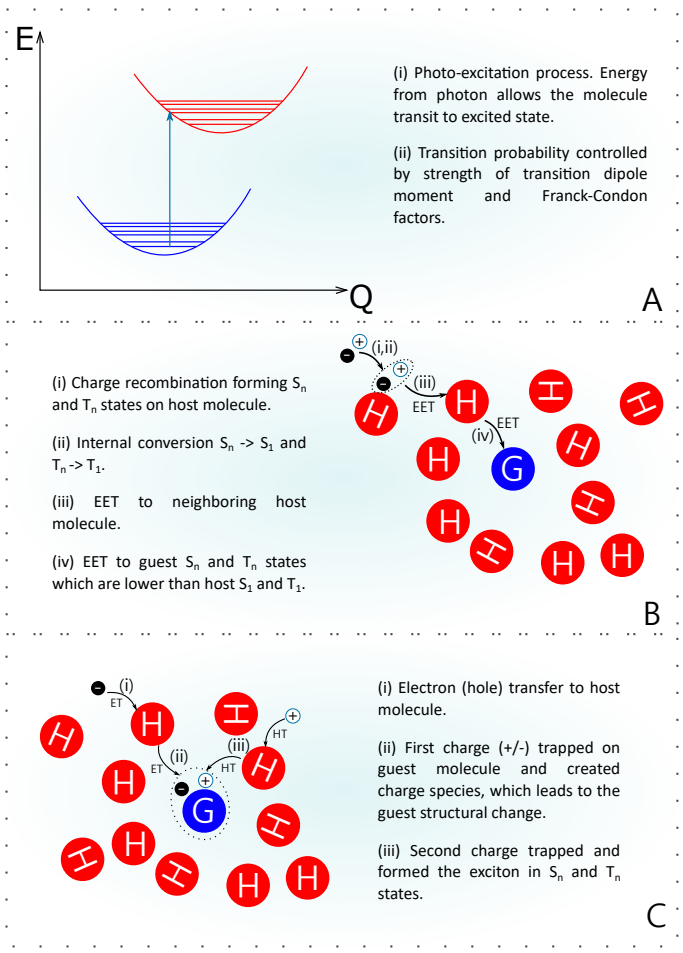

FIGURE 5.1: Schematic representing the methods of generating excited states (A) Photo-excitation process, (B) Electron-hole recombination on the host molecule and preceded by energy transfer, (C) Electron-hole recombination directly on the guest molecule[10]

assumed that the triplet excitons would be most likely to form by charge carrier recombination directly in the TQB-TA form. However, the charge trapping on TQB will lead to the formation of the TQB-TB form. Consequently, once the first charge is trapped, structural changes can significantly affect the initial conditions of the excited state generated and therefore the mechanism and probability for TADF. Understanding this in more detail is the focus of the present chapter.

5.2 Methods

In this section we outline the computational approaches used to understanding the exciton generation in OLED materials.

5.2.1 Quantum Chemistry

Optimized geometries of TQB in their ground and excited states and host molecules (mCBP and DPEPO) were calculated using DFT/TDDFT with TDA[94] as implemented within the ORCA quantum chemistry program [120], using the PBE0 exchange and correlation functional[163]. A Def2-SVP basis set [164] and the polarisable continuum model(PCM)[165, 166, 167] with the solvent toluene were used throughout. Potential energy surfaces (PES) obtained using ORCA for both the cationic and anionic geometries of TQB along the ESIPT reaction coordinate.

The Maximum overlap Method (MOM) [163] used to study the geometric changes upon charge trapping in higher excited states. The basic idea is to find the orbital (wavefunction) that has the maximum overlap with a target orbital, and then to use that orbital to generate a new set of orbitals through a linear combination of existing orbitals. This process is repeated until the desired accuracy is reached. The MOM method allows the estimation of excited states by enforcing a specific excited state orbital occupation. The MOM method prevents variational collapse of the core-hole state during iterative optimisation cycles by setting the occupancy of the orbitals such that the overlap between the occupied orbitals of the current (n^{th}) and previous ($(n-1)^{\text{th}}$) iteration is maximized, rather than setting the occupancies according to the *aufbau* principle, as is traditional. An orbital overlap matrix, $\mathbf{O}$, is obtained at each iteration *via* Eq. 5.1:

$$\mathbf{O} = \mathbf{C}_{n-1}^{\dagger}\mathbf{S}\mathbf{C}_{n} \tag{5.1}$$

from which the projection, p_j, of the i^{th} orbital for the current iteration onto the j^{th} orbital from the previous iteration is found *via* Eq. 5.2:

$$p_j = \sum_i O_{ij} \tag{5.2}$$

The occupied orbitals are then set to those with the largest projections. While highly effective in general, the performance of the MOM is notably better for low-lying, as opposed to higher-lying, core-excited states.

In this case, we changed the electron and hole's occupation from the LUMO to LUMO+7 and HOMO to HOMO-7 inside of single occupied molecular orbit (SOMO) of the charge trapped system to mimic excited charge trapped states. This is implemented within the package Qchem [168].

5.2.2 Molecular dynamics

Molecular dynamics of TQB and its hosts was done by Amber14[169] and ORCA[120]. The charges of TQB and hosts were determined by Q-CHEM[168] with Charges from Electrostatic Potentials using a Grid-based method (ChElPG) [170]. And then the force field set up as default in Amber. Once the force field has been set up, firstly, the system need to be minimized, following the default Amber setting, the energy of system we built up before will be minimized. Then the system will be heated up from 10K to a high temperature 1000K and sampling the system followed by temperatures. Finally, the simulation will be run. The system will be cooled down from 1000K to room temperature, 300K.

Quantum mechanism Molecule mechanism molecular dynamics (QMMM-MD)[171] of TQB and its hosts' single point energies in ground/excited states and charged states were performed by Amber14[169], especially, the quantum mechanism part was programmed by ORCA[120] package with PBE0 functional and Def2-SVP [122] basis set with polarizable cotinuum model (PCM) in Toluene. For each host molecules, both electron and hole transfer were simulated for 200 different configurations to calculate free energy and orbital energy.

5.2.3 Marcus Theory

To obtain the rate of charge transfer, Marcus theory shows in Figure 5.2, and the equation:

$$k = \frac{2\pi}{\hbar}|H_{DA}|^2 \frac{1}{\sqrt{4\pi\lambda K_B T}} e^{-\frac{(\lambda+\Delta G)^2}{4\lambda K_B T}} [172] \tag{5.3}$$

Charge transfer rate (k) was calculated under the electronic coupling of the charge donor/acceptor (H_{DA}), total Gibbs free energy change of the charge transition (ΔG), reorganization energy (λ), K_B is Boltzmann constant and T is the temperature 298K.

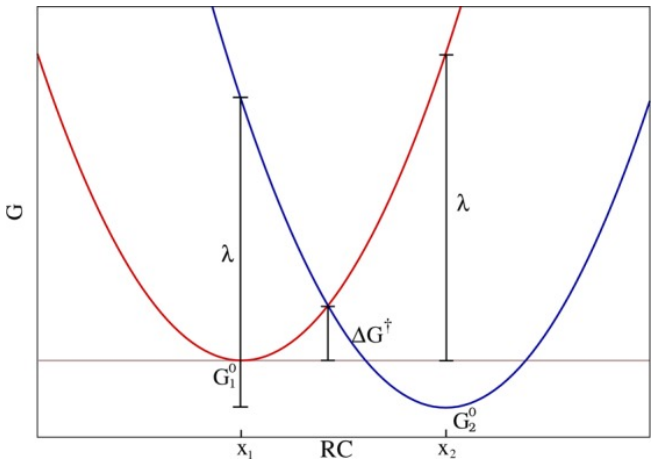

FIGURE 5.2: Marcus-Hush theory shows by Four-points model

This theory has been successfully applied to describe and predict the activation barriers and the electron-transfer rates (k) in physics, chemistry and biology field systems. [173] Following this theory, as long as the Gibbs free energy of the reactant and product, reorganization energy and the direct coupling energy could be calculated, the rate of charge transfer can be obtained. The reactant and product, in charge transferring occasion, can be understood as the host molecule before and after the charge transfer.

To fully figure out the charge transfer, it is key to calculate the charge transfer rate (k) by Marcus theory[172]. In this situation, charge transfer could be seen as a reaction and the charge transferred between host and guest molecules by following reaction:

$$Host^{+/-} + Guest^0 = Guest^{+/-} + Host^0 \tag{5.4}$$

It's simple to calculate the Gibbs free energy by Marcus theory, as long as we could obtain the lowest energies of the *Reactants* and *Products* during the charge transfer.

5.3 Results

In this section, new insights into the dynamics involved in charge recombination are obtained. This section initially focuses upon the trapping of a single first charge, be it an electron or a hole, before considering the second charge trapping which forms the exciton.

5.3.1 First charge trapping

Hole trapping

We first consider the dynamics associated with hole trapping on TQB, *i.e* the scenario where the hole arrives first on the guest molecule and we assume that there is sufficient time ($\sim$10 ps) between the first and second charge arrives for the cationic species to completely relax [174]. Figure 5.4 shows a relaxed surface scan along the proton transfer coordinate of the cationic form of TQB. This clearly shows that, in contrast to the electronic ground state of the neutral species, the TQB-TB form is preferred by $\sim$0.1 eV, with the barrier from the initial TQB-TA to TQB-TB being only 0.025 eV, comparable to kT at 300 K. This suggests that upon hole trapping, rapid relaxation of the TQB-TA form to TQB-TB is highly probable.

Figure 5.3 right assumes that the electron is removed from the HOMO, however this is not necessarily the case. Indeed, instantaneous electron addition or removal can form an electronic wavepacket, a coherent distribution of population over a range of excited states. While the coherence is likely to be short lived and play limited role, the distribution of states could play a larger role. Figure 5.4 right show the potential energy scans for electron removing from the HOMO-1 and HOMO-2 as well as the HOMO. These show a very similar potential profile and a energy energy separation, $\sim$0.2 eV meaning that the contribution of higher lying states is much less probable.

Besides the structural changes upon electron removal, the hole transfer rate between guest and host is also an important consideration for the exciton generation. Here, we estimate this rate using a semi-classical Fermi's golden rule approach. This requires the coupling, ΔG and λ, as described in the methods section. Table 5.1 shows these parameters calculated as described

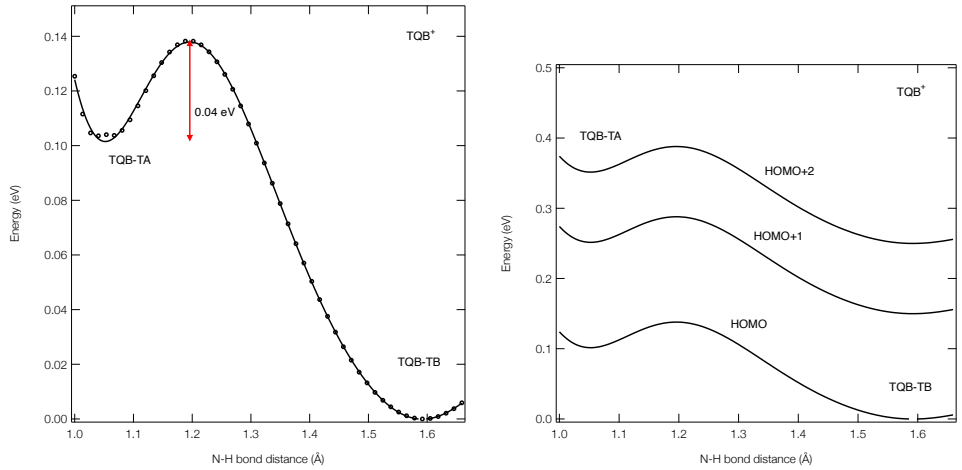

FIGURE 5.3: Relax surface soft scan along the proton transfer coordinates of TQB^+ indicates that with a low energy barrier, the TQB-TB is more favorable in cation(Left); After an electron moved from the HOMO, same surface scan has been done for TQB^+ and results are agreed with previous.

	ΔG (QM/MM) (eV)	λ (eV)	H_{DA} (cm^{-1})	$k_{HT}(\mathrm{s}_{-1})$
DPEPO	-0.90±0.21	0.30	0.003	1.99×10^{10}
mCBP	-0.14±0.18	0.15	0.032	2.07×10^{14}

TABLE 5.1: After ΔG, λ and H_{DA} were calculated, k_{HT} will be easily resulted by Marcus theory.

in the methods section. ΔG has been calculated using QM/MM as simple energy differences simulated using optimised quantum chemistry simulations are unlikely to be representative of the native solid state environment native to OLEDs. Figure 5.4 shows the probability distribution of energies for ΔG in DPEPO and mCBP, where average values of -0.90±0.21 and -0.14±0.18 eV, respectively are found. Using the approach, the hole transfer rate is found to be significantly faster for mCBP, which is discussed and compared to the electron transfer below.

Electron trapping

Having considered the hole trapping, we now move onto consider the electron trapping. Figure 5.5 shows a relaxed surface scan along the proton transfer coordinate of the anionic form of TQB. As for the cationic form, the TQB-TB form is clearly favoured, although in this case a larger barrier of 0.06 eV going from the initial TQB-TA to TQB-TB is observed. Beyond this, if we assume the electron can also enter the LUMO+1 or LUMO+2 (Figure5.5 upper)

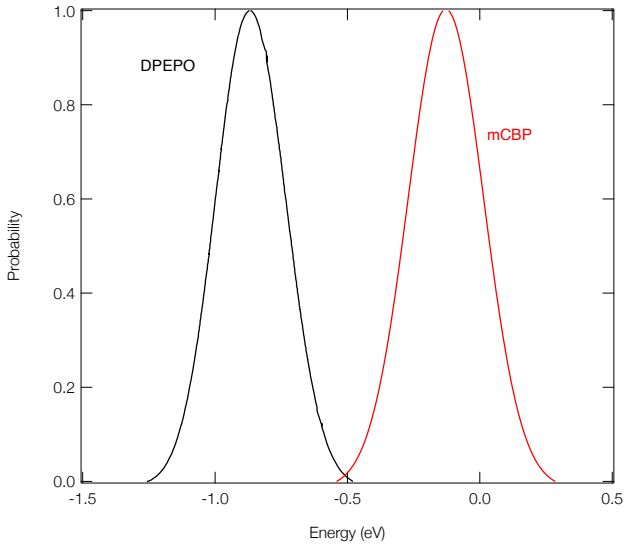

FIGURE 5.4: Normalised calculated probability distribution of ΔG for hole transfer from the host (either mCBP or DPEPO) to TQB.

a slightly different perspective appears. In this case, electron trapping in the LUMO+1 and LUMO+2 makes the TQB-TB structure unfavourable and the TQB-TA form is preferred.

We estimate the electron trapping rate using a semi-classical Fermi's golden rule approach, similar with the hole transfer. Δ, λ and H_{DA} are required. In table 5.2, all these parameters have BEEN calculated as described in the methods section. ΔG has been calculated using QM/MM as simple energy differences simulated using optimised quantum chemistry simulations are unlikely to be representative of the native solid state environment native to OLEDs. Figure 5.5 indicates the probability distribution of energies for ΔG in DPEPO and mCBP, where average values of -0.71$\pm$0.18 and -0.39$\pm$0.13 eV, respectively are found.

	ΔG (QM/MM) (eV)	λ (eV)	H_{DA} (cm^{-1})	k_{ET}(s_{-1})
DPEPO	-0.71$\pm$0.18	0.46	0.0003	3.85×10^{9}
mCBP	-0.39$\pm$0.13	0.77	0.0504	5.52×10^{13}

TABLE 5.2: Electron transfer rate (k_{ET}) could be calculated by Marcus theory with the simulation results of ΔG,λ and H_{DA}

Summary of single charge trapping mechanism

In the previous section we have examined the electron and hole transfer dynamics, which would represent the first step towards exciton formation in

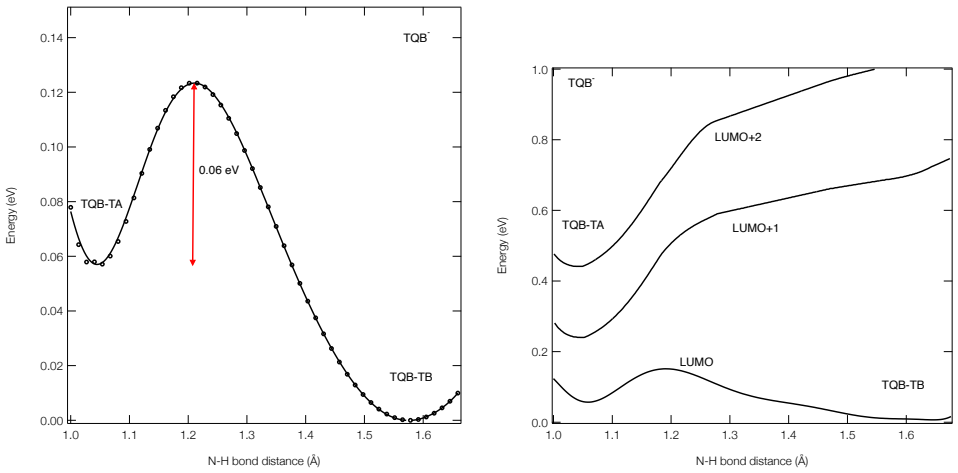

FIGURE 5.5: Relax surface scan for anion geometry along the proton transfer coordinates also indicates that TQB-TB is favorable, although there is a larger energy barrier(0.06 eV)(Left); Soft scan has done for TQB-TB assuming the trapped electron in different orbital (LUMO/LUMO+1/LUMO+2), result shows that only LUMO is possible to allow the electron locate.

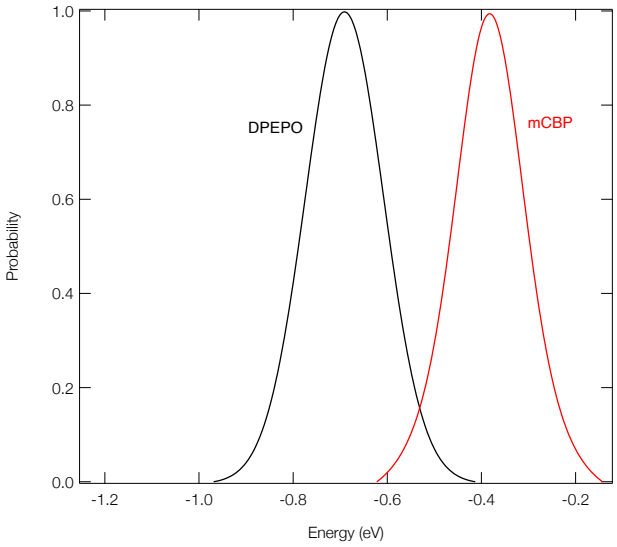

FIGURE 5.6: Based on 200 samples from ab intio molecular dynamics(AIMD), calculated the ΔG with standard deviation (σ) with different host molecules by QM/MM MD. (Dash line are calculated by ORCA in optimized geometries)

OLEDs. From this it is clear that upon charge trapping the TQB-TB structure is energetically preferred in both the anionic and cationic forms. Therefore we expect that upon charge trapping a geometric relaxation occurs forming the fully relaxed TQB-TB structure. This species will then become focus of the following section focused upon the second charge trapping and exciton formation.

In both cases, the electron and hole transfer rates in each host are similar. This means that there is likely to be no particular preference for electron or hole trapping occurring on the guest first. In both case the transfer from DPEPO to TQB is significantly slow that mCBP and this sluggish kinetics is in close agreement with the poor device performance of OLEDs with DPEPO hosts observed by Adachi *et al.* [54], which is attributed to the poor charge carrier transport capabilities. [175].

5.3.2 Exciton Formation: The trapping of the second charge

In the previous sections we considered the trapping of a charge on the guest. We now switch our focus to the trapping of the second charge forming the exciton. Despite its importance, surprisingly little is known about how charge recombination works in host-guest systems. Throughout this section, we use QM/MM molecular dynamics and sample snapshots, as described in the methods section. The most importance aspect is the energetic associated with exciton formation and this is calculated using the thermodynamic cycle shown below, which is based upon the RehmWeller approach adopted by Zhu *et al.* [176]

This thermodynamic cycle focuses upon the dissociation exciton to form separate charges on the guest and host. Here, the binding energy between the guest and host charges will affect the stabilisation between the products and change the energy barrier considerably. Consequently, we will investigate the reaction from the $G^* \cdots H$ complex to the $G^{+/-} \cdots H^{-/+}$ complex. This is achieved using 5 thermodynamic steps:

- $G^* \cdots H \rightarrow G^*$+H: The complex is dissociated into independent H and G^* by removal of the binding energy.
- G^*+H $\rightarrow G^*$+$H^{+/-}$: A charge is added to the host.
- G^*+$H^{+/-} \rightarrow$ G+$H^{+/-}$: The exciton is quenched.
- G+$H^{+/-} \rightarrow G^{+/-}$+$H^{+/-}$: A second charge is added to the guest

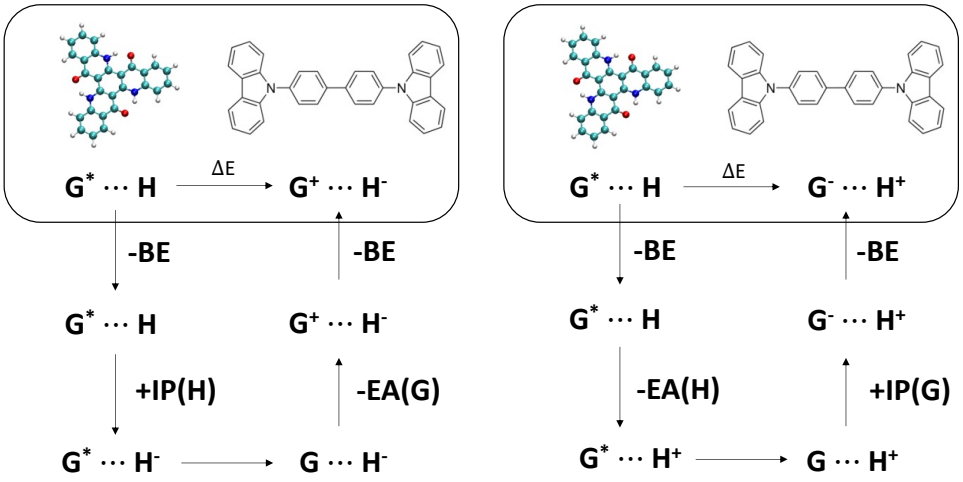

FIGURE 5.7: Left: Thermodynamic cycle for computation of the process in which a host exciton is dissociated to form a host anion and a guest cation. Right: Thermodynamic cycle for computation of the process in which a host exciton is dissociated to form a host cation and a guest anion. (BE: Binding Energy, EA: Electron Affinity, IP: Ionization Potential and G/H: Guest/Host)

- $G^{+/-}$+$H^{+/-} \rightarrow G^{+/-} \cdots H^{+/-}$: The independent charges are bound together.

This cycle makes it possible to calculate the energy change upon formation of the exciton and shed insight into both the driving force for the formation, and its stability. Since the first charge trapping gave a preference for the TQB-TB geometry, the calculations in this section have focused upon exciton formation at the TQB-TB geometry.

Figure 5.8 shows the calculated probability distribution of reaction energy obtained from the thermodynamic cycle for both the singlet (S_1) and triplet (T_1) states of TQB in DPEPO. Figure 5.8a shows the scenario where the hole has already been trapped, while Figure 5.8b shows the case where the electron has been trapped. For Figure 5.8a, the probability distributions shows that the reaction energies for exciton formation is appreciably downhill by 0.8 eV or more. This suggests formation of the exciton on the guest is favourable with a significant energy benefit. The triplet exciton formation process has higher gain because of its lower energy compared to the singlet state. The low nature of the triplet excited state means that higher energy states could still be formed with a favourable energy benefit. As shown in chapter 3 there are another 3 triplet states within 0.5 eV of the T_1 in TQB-TB. In addition, these states all favour the TQB-TA form and therefore formation

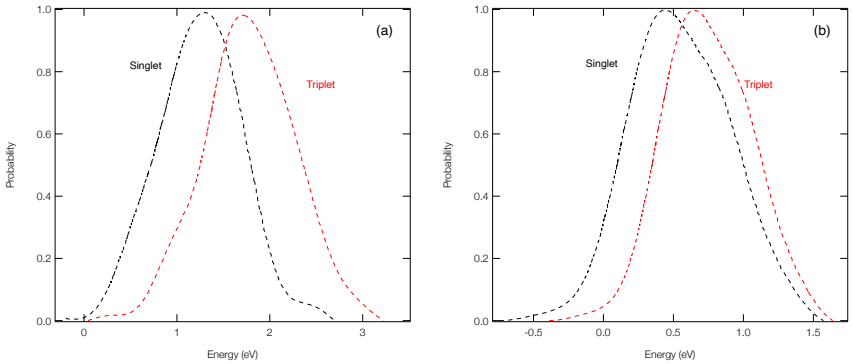

FIGURE 5.8: Left: Thermodynamic cycle for computation of the process in which a DPEPO exciton is dissociated to form a host anion and a guest cation. This shows the case where the hole is trapped first. Right: Thermodynamic cycle for computation of the process in which a DPEPO exciton is dissociated to form a DPEPO cation and a TQB anion. This shows the case where the electron is trapped first.

of these higher lying states could result in significant structural dynamics. It is also worth noting that these states lie higher in energy that the singlet, and could offer a more direct route for triplet harvesting. By inspection of Figure 5.8b, it is noticed that the energy is lower in the association for the $G^* \cdots H \rightarrow G^- \cdots H^+$ approach, compared to the case where the hole is trapped on the guest first. However, even for these the energy benefit is substantial for both the singlet and triplet states.

Figure 5.9 shows the calculated probability distribution of reaction energy obtained from the thermodynamic cycle for both the singlet (S_1) and triplet (T_1) states of TQB in mCBP. Figure 5.9a shows the hole trapped possibility, and Figure 5.9b for electron. It's similar when the host is DPEPO that possibility of electron and hole trapping indicates the excitation reaction energies are decreasing. Also, the lower energy in triplet helps the triplet exciton formation have higher gain. In the meantime, TQB-TA is more favorable at these states, which means the higher lying states will lead structural dynamics.

5.4 Conclusion

Understanding the mechanism of exciton generation during electrical excitation in OLEDs is critical designing new high performing devices. It is clear that the mechanism is very different to the one of excited state formation using interaction with photons. However, despite this there has been surprisingly little work focusing on this process, a fact that this chapter seeks

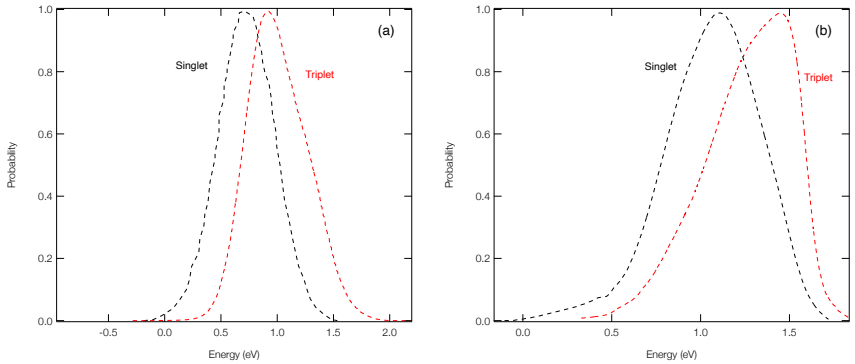

FIGURE 5.9: Left: Thermodynamic cycle for computation of the process in which a mCBP exciton is dissociated to form a mCBP anion and a TQB cation. This shows the case where the hole is trapped first. Right: Thermodynamic cycle for computation of the process in which a mCBP exciton is dissociated to form a mCBP cation and a TQB anion. This shows the case where the electron is trapped first.

to address. In previous chapters we have outlined that it plays an important role in the TADF emitters with ESIPT mechanism. Firstly, the exciton generation could help understand both ESIPT and TADF in a different level. Also, understanding the exciton formation could help us know how it enhance the utilization and external quantum efficiency.

In this chapter we initially study the the electron and hole transfer dynamics, which would represent the first step towards exciton formation in OLEDs. From this it is clear that upon charge trapping the TQB-TB structure is energetically preferred in both the anionic and cationic forms. Therefore we expect that upon charge trapping a geometric relaxation occurs forming the fully relaxed TQB-TB structure. In both cases, the electron and hole transfer rates in each host are similar. This means that there is likely to be no particular preference for electron or hole trapping occurring on the guest first. In both case the transfer from DPEPO to TQB is significantly slows that mCBP and this sluggish kinetics is in close agreement with the poor device performance of OLEDs with DPEPO hosts observed by Adachi *et al.* [54], which is attributed to the poor charge carrier transport capabilities. [175].

In for the second second charge trapping, the insight focuses on the ΔG as the driving force for exciton formation. For DPEPO, the ΔG for the case where the hole is trapped first clear gives rise to a larger free energy change which would likely accelerate the rate compared to electron trapping first. In the case of mCBP, the ΔG is similar in both cases which suggests that there is not one clearly preferred method. However, it is noted that this approach

ignores the effect of the coupling between the guest and host on the rate.

Despite the progress and insight made in this chapter, we have been unable to simulate the rates of exciton formation, *i.e.* the second charge trapping, which would be required to provide the full insight into exciton formation and dynamics. This is very challenging and would require large scale quantum calculations. An alternative route, which should be the focus of future work is the development of kinetic monte carlo models which allow to have more variables and the randomness to provide a more realistic representation of system. Work in this direction is underway.

Chapter 6

Conclusion

Thermally Activated Delayed Fluorescence (TADF) and Excited-State Intramolecular Proton Transfer (ESIPT) are two distinct mechanisms that have revolutionized the field of organic light-emitting materials and hold great promise for applications in optoelectronic devices. TADF exploits the efficient upconversion of triplet excitons into singlet excitons, enabling enhanced electroluminescence efficiency. It has garnered significant attention due to its potential for realizing high-efficiency organic light-emitting diodes (OLEDs) and is being extensively researched. On the other hand, ESIPT is a photophysical process that involves the transfer of a proton in the excited state, leading to a change in the molecular structure and spectral properties. ESIPT materials have been studied for their unique photoluminescence and potential applications in sensing and fluorescence-based technologies. Both TADF and ESIPT are intriguing mechanisms with their own sets of advantages and challenges. TADF offers a route to improve OLED efficiency and is well-understood, whereas ESIPT is more specialized and has niche applications. The choice between these mechanisms depends on the specific requirements of the optoelectronic device and the desired photophysical properties. Further research is needed to optimize and harness the full potential of these mechanisms in practical applications, and their development will continue to shape the landscape of organic electronics and photonics.

In this thesis, we've discussed key properties of the TQB molecule, ESIPT, and TADF. It's essential to vary molecular designs for better TADF materials, not only for efficient emitters but also to understand TADF mechanisms, especially the differences between photo and electrical excitation, which are crucial for device applications. Our work used quantum chemistry and simulations to explore how triplet harvesting works in ESIPT, focusing on TQB as an example.

The simulations and calculations in chapter 3 and 4 indeed helped us understand the mechanism step by step. Although, we have yielded valuable

progress and insights, we have encountered limitations in simulating the rates of exciton formation and the second charge trapping, which are crucial for a comprehensive understanding of exciton formation and dynamics. Simulating these processes presents significant challenges, demanding extensive quantum calculations on a large scale. As an alternative and promising avenue for future research, the development of kinetic Monte Carlo models should take center stage.

In summary, this thesis has contributed to our understanding of these mechanisms and their potential for future applications, emphasizing the importance of diverse molecular designs and the ongoing need for research and innovation in the field of organic electronics. The journey towards more efficient, sustainable, and versatile OLEDs is an ongoing one, and the insights gained in this work will undoubtedly pave the way for future breakthroughs in this exciting field.

Bibliography

[1] J.A. Duffie and W.A. Beckman. "Global distribution of solar radiation". In: *Solar Energy* 80.5 (2006), pp. 623–629.

[2] A. Santos et al. "Application of Response Surface Methodology to Evaluate Photodynamic Inactivation Mediated by Eosin Y and 530 nm LED against Staphylococcus aureus". In: *A. Antibiotics (Basel)* 9(3) (2020), p. 125.

[3] Z. Li et al. "The Development Path of the Lighting Industry in Mainland China: Execution of Energy Conservation and Management on Mercury Emission". In: *Int J Environ Res Public Health* 15(12) (2018), p. 2883.

[4] J. W. ALLEN and R. J. CHERRY. "Space-Charge Currents in Gallium Arsenide". In: *Nature* 189 (1961), pp. 297–298.

[5] N. Holonyak and S. F. Bevacqua. "COHERENT (VISIBLE) LIGHT EMISSION FROM Ga(As1xPx) JUNCTIONS". In: *Applied Physics Letters* 1 (1962), pp. 82–83.

[6] P. Stanish and P. Radovanovic. "Energy Transfer between Conjugated Colloidal Ga_2O_3 and $CdSe/CdS$ *Core/Shell* Nanocrystals for White Light Emitting Applications". In: *Nanomaterials Basel* 6(2) (2016), p. 32.

[7] J. Xiang et al. "Numerical Simulation, Machining and Testing of a Phase Change Heat Sink for high Power LEDs". In: *Materials (Basel)* 12(13) (2019), p. 2193.

[8] J. Cho et al. "White light-emitting diodes: History, progress, and future." In: *Laser Photonics Rev.* 11 (2017), p. 1600147.

[9] A. Nardelli et al. "Assessment of Light Emitting Diodes technology for general lighting: A critical review". In: *Renew. Sustain. Energy Rev.* 75 (2017), pp. 368–379.

[10] Eng J. and Penfold T. J. "Understanding and Designing Thermally Activated Delayed Fluorescence Emitters: Beyond the Energy Gap Approximation". In: *The Chemical Record* 20 (2020), pp. 831–856.

[11] M. Pope, H. P. Kallmann, and P. Magnante. "Electroluminescence in Organic Crystals". In: *The Journal of Chemical Physics* 38 (1963), pp. 2042–2043.

[12] C. W. Tang and S. A. VanSlyke. "Organic electroluminescent diodes". In: *Applied Physics Letters* 51 (1987), pp. 913–915.

[13] M. E. Thompson, S. R. Forrest, and et al. "Highly efficient phosphorescent emission from organic electroluminescent devices". In: *Nature* 395 (1998), pp. 151–154.

[14] H. Uoyama et al. "Highly efficient organic light-emitting diodes from delayed fluorescence". In: *Nature* 492 (2012), pp. 234–238.

[15] R.J. Collins. "Electroluminescent devices". In: *Proceedings of the IEEE* 57.8 (1969), pp. 1361–1374.

[16] D. Yokoyama. "Molecular orientation in small-molecule organic light-emitting diodes". In: *J. Mater. Chem* 21 (2011), p. 19187.

[17] T. Komino et al. "Electroluminescence from completely horizontally oriented dye molecules". In: *Applied Physics Letters* 108 (2016), p. 241106.

[18] Chan S. et al. "Relationship between molecular structure and dipole orientation of thermally activated delayed fluorescent emitters". In: *Organic Electronics* 42 (2017), pp. 337–342.

[19] Edinst blog. "TADF: What is Themally Activated Delayed Fluoresence". In: *edinst.com* 1 (2019), p. 1.

[20] J. Jou et al. "Correction: Approaches for fabricating high efficiency organic light emitting diodes". In: *Journal of Materials Chemistry C* 1 (2015), pp. 2974–3002.

[21] E. Mihajlo, R. Vidisha, and M. Christel. "Timedependent approach to spin-vibronic coupling: Implementation and assessment". In: *The Journal of Chemical Physics* 140(11) (2014), p. 114104.

[22] M. H. Beck et al. "The multiconfiguration time-dependent Hartree (MCTDH) method: a highly efficient algorithm for propagating wavepackets". In: *physrep* 324 (2000), pp. 1–105.

[23] B. F. E. Curchod and T. J. Martínez. "Ab Initio Nonadiabatic Quantum Molecular Dynamics". In: *Chemical Reviews* 118 (2018), pp. 3305–3336.

[24] Penfold T. J., Dias F. B., and Monkman A. P. "The theory of thermally activated delayed fluorescence for organic light emitting diodes". In: *Chem. Commun.* 54 (2018), pp. 3926–3935.

[25] C. Baleizão and M. N. Berberan-Santos. "Thermally activated delayed fluorescence as a cycling process between excited singlet and triplet states: Application to the fullerenes". In: *The Journal of Chemical Physics* 126 (2007), p. 204510.

[26] Huiyuan Cheng et al. "Understanding and minimizing non-radiative recombination losses in perovskite light-emitting diodes". In: *J. Mater. Chem. C* 10 (37 2022), pp. 13590–13610.

[27] R. Delorme and F. Perrin. "Durées de fluorescence des sels d'uranyle solides et de leurs solutions". In: *J. Phys. Radium* 10.55 (1929), pp. 177–186.

[28] G. N. Lewis, D. Lipkin, and T. T. Magel. "Reversible Photochemical Processes in Rigid Media. A Study of the Phosphorescent State". In: *Journal of the American Chemical Society* 63 (1941), pp. 3005–3018.

[29] C. A. Parker and C. G. Hatchard. "Triplet-singlet emission in fluid solutions. Phosphorescence of eosin". In: *Trans. Faraday Soc.* 57 (1961), pp. 1894–1904.

[30] M. Y. Wong and E. Zysman-Colman. "Purely Organic Thermally Activated Delayed Fluorescence Materials for Organic Light-Emitting Diodes". In: *Advanced Materials* 29.22 (2017), p. 1605444.

[31] Z. Yang et al. "Recent advances in organic thermally activated delayed fluorescence materials". In: *Chem. Soc. Rev.* 46 (2017), pp. 915–1016.

[32] F. B. Dias, T. J. Penfold, and A. P. Monkman. "Photophysics of Thermally Activated Delayed Fluorescence Molecules". In: *Methods Appl. Fluoresc.* 5 (2017), p. 012001.

[33] J. R. Kirchhoff et al. "Temperature dependence of luminescence from Cu(NN)2+ systems in fluid solution. Evidence for the participation of two excited states". In: *Inorganic Chemistry* 22 (1983), pp. 2380–2384.

[34] F.B. Dias, T.J. Penfold, and A.P. Monkman. "Photophysics of thermally activated delayed fluorescence molecules". In: *Methods Appl Fluoresc* 9 (2017), 5(1):012001.

[35] T. Ye, Y. Kai, and C. Ting. "Thermally activated delayed fluorescence materials towards the breakthrough of organoelectronics". In: *Advanced materials* 26(47) (2014), pp. 7931–7958.

[36] C. M. Marian. "Spin–orbit coupling and intersystem crossing in molecules". In: *WIREs Computational Molecular Science* 2.2 (2011), pp. 187–203.

[37] M. K. Etherington et al. “Revealing the Spin–Vibronic Coupling Mechanism of Thermally Activated Delayed Fluorescence”. In: *Nat. Commun.* 7 (2016), p. 13680.

[38] F. B. Dias et al. “Triplet Harvesting with 100% Efficiency by Way of Thermally Activated Delayed Fluorescence in Charge Transfer OLED Emitters”. In: *Adv. Mater.* 25 (2013), p. 3707.

[39] P.L. Santos et al. “Engineering the singlet-triplet energy splitting in a TADF molecule”. In: *Journal of Materials Chemistry C* 4 (2016), pp. 3815–3824.

[40] J. S. Ward et al. “The interplay of thermally activated delayed fluorescence (TADF) and room temperature organic phosphorescence in sterically-constrained donor–acceptor charge-transfer molecules”. In: *Chem. Commun.* 52 (12 2016), pp. 2612–2615.

[41] A. Weller. “Zeitschrift für Elektrochemie”. In: *Ber. Bunsen-Ges. Phys. Chem.* 60 (1956), p. 1144.

[42] Y. Frolov and etc. “Luminescence of flavonoid compounds”. In: *Russ. Chem. Bull* 23 (1974), pp. 2279–2281.

[43] M. F. Rode and A. L. Sobolewski. “Effect of Chemical Substituents on the Energetical Landscape of a Molecular Photoswitch: An Ab Initio Study”. In: *The Journal of Physical Chemistry A* 114.44 (2010), pp. 11879–11889.

[44] C. Hsieh, C. Jiang, and P. Chou. “Recent Experimental Advances on Excited-State Intramolecular Proton Coupled Electron Transfer Reaction”. In: *Accounts of Chemical Research* 43.10 (2010), pp. 1364–1374.

[45] H. C. Joshi and L. Antonov. “Excited-State Intramolecular Proton Transfer: A Short Introductory Review”. In: *Molecules* 26.5 (2021).

[46] K. Wu et al. “De Novo Design of Excited-State Intramolecular Proton Transfer Emitters via a Thermally Activated Delayed Fluorescence Channel”. In: *Journal of the American Chemical Society* 140.28 (2018), pp. 8877–8886.

[47] H. Böhnke et al. “Ultrafast dynamics of the ESIPT photoswitch N-(3-pyridinyl)-2-pyridinecarboxamide”. In: *Phys. Chem. Chem. Phys.* 20 (4 2018), pp. 2646–2655.

[48] A. L. Sobolewski and W. Domcke. "Photophysics of intramolecularly hydrogen-bonded aromatic systems: ab initio exploration of the excited-state deactivation mechanisms of salicylic acid". In: *Phys. Chem. Chem. Phys.* 8 (29 2006), pp. 3410–3417.

[49] J. Jankowska and A. L. Sobolewski. "Modern Theoretical Approaches to Modeling the Excited-State Intramolecular Proton Transfer: An Overview". In: *Molecules* 26 (2021), p. 5140.

[50] X. Shang et al. "Optical nonlinearities and transient dynamics of 2-(2′-hydroxyphenyl)benzoxazole studied by single-beam and time-resolved two-color Z-scan techniques". In: *J. Opt. Soc. Am. B* 15 (1998), pp. 854–862.

[51] K. Sakai, M. Ichikawa, and Y Taniguchi. "Photoluminescent mechanism of a proton-transfer laser dye in highly doped polymer films". In: *Chemical Physics Letters* 420 (2006), pp. 405–409.

[52] A. Klymchenko and A. Demchenko. "Electrochromic Modulation of Excited-State Intramolecular Proton Transfer: The New Principle in Design of Fluorescence Sensors". In: *Journal of the American Chemical Society* 124 (2002), pp. 12372–12379.

[53] A. Klymchenko et al. "Fluorescent Probe Based on Intramolecular Proton Transfer for Fast Ratiometric Measurement of Cellular Transmembrane Potential". In: *The Journal of Physical Chemistry B* 110 (2006), pp. 13624–13632.

[54] M. Mamada et al. "Highly Efficient Thermally Activated Delayed Fluorescence from an Excited-State Intramolecular Proton Transfer System". In: *ACS Cent. Sci.* 3 (2017), p. 769.

[55] J. Zhao et al. "Excited State Intramolecular Proton Transfer (ESIPT): From Principal Photophysics to the Development of New Chromophores and Applications in Fluorescent Molecular Probes and Luminescent Materials". In: *Phys. Chem. Chem. Phys.* 14 (2012), p. 8803.

[56] J. Seo, S. Kim, and S. Y. Park. "Strong Solvatochromic Fluorescence From the Intramolecular Charge-Transfer State Created by Excited-State Intramolecular Proton Transfer". In: *J. Am. Chem. Soc.* 126 (2004), p. 11154.

[57] J. E. Kwon and S. Y. Park. "Advanced Organic Optoelectronic Materials: Harnessing Excited-State Intramolecular Proton Transfer (ESIPT) Process". In: *Adv. Mater.* 23 (2011), p. 3615.

[58] S. Park et al. "Imidazole-Based Excited-State Intramolecular Proton-Transfer (ESIPT) Materials: Observation of Thermally Activated Delayed Fluorescence (TDF)". In: *J. Phys. Chem. A* 111 (2007), p. 9649.

[59] V. S. Padalkar and S. Seki. "Excited-State Intramolecular Proton-Transfer (ESIPT)-Inspired Solid State Emitters". In: *Chem. Soc. Rev.* 45 (2016), p. 169.

[60] T.J. Penfold et al. "Excited state dynamics initiated by an electromagnetic field within the Variational Multi-Configurational Gaussian (vMCG) method". In: *Computational and Theoretical Chemistry* 1160 (2019), pp. 24–30.

[61] M. Pápai et al. "How To Excite Nuclear Wavepackets into Electronically Degenerate States in Spin-Vibronic Quantum Dynamics Simulations". In: *Journal of Chemical Theory and Computation* 14.8 (2018), pp. 3967–3974.

[62] M. A. Baldo et al. "Excitonic singlet-triplet ratio in a semiconducting organic thin film". In: *Phys. Rev. B* 60 (20 1999), pp. 14422–14428.

[63] F.A. Berezin and M. Shubin. *The Schrödinger Equation*. Mathematics and its Applications. Springer Netherlands, 2012. ISBN: 9789401131544.

[64] J.E. Subotnik et al. "Constructing diabatic states from adiabatic states: Extending generalized Mulliken–Hush to multiple charge centers with Boys localization". In: *The Journal of chemical physics* 129.24 (2008), p. 244101.

[65] T. Van Voorhis et al. "The diabatic picture of electron transfer, reaction barriers, and molecular dynamics". In: *Annual review of physical chemistry* 61 (2010), pp. 149–170.

[66] J. E. Subotnik et al. "The requisite electronic structure theory to describe photoexcited nonadiabatic dynamics: Nonadiabatic derivative couplings and diabatic electronic couplings". In: *Accounts of chemical research* 48.5 (2015), pp. 1340–1350.

[67] J. E. Subotnik et al. "Predicting Accurate Electronic Excitation Transfer Rates via Marcus Theory with Boys or Edmiston- Ruedenberg Localized Diabatization". In: *The Journal of Physical Chemistry A* 114.33 (2010), pp. 8665–8675.

[68] S. Fatehi, E. Alguire, and J. E Subotnik. "Derivative couplings and analytic gradients for diabatic states, with an implementation for Boys-localized configuration-interaction singles". In: *The Journal of chemical physics* 139.12 (2013), p. 124112.

[69] X. Zhu and D. R Yarkony. "On the Construction of Property Based Diabatizations: Diabolical Singular Points". In: *The Journal of Physical Chemistry A* 119.50 (2015), pp. 12383–12391.

[70] E. Hoyer et al. "Diabatization based on the dipole and quadrupole: The DQ method". In: *The Journal of chemical physics* 141.11 (2014), p. 114104.

[71] C. E. Hoyer et al. "The DQ and DQΦ electronic structure diabatization methods: Validation for general applications". In: *The Journal of chemical physics* 144.19 (2016), p. 194101.

[72] D. Wolfgang, K. Horst, and et al. *Conical intersections: electronic structure, dynamics & spectroscopy*. Vol. 15. World Scientific, 2004.

[73] T. J. Penfold and G. A. Worth. "A model Hamiltonian to simulate the complex photochemistry of benzene II". In: *The Journal of Chemical Physics* 131.6 (2009), p. 064303.

[74] T. J. Penfold et al. "Quantum dynamics study of the competing ultrafast intersystem crossing and internal conversion in the "channel 3" region of benzene". In: *The Journal of Chemical Physics* 137.20 (2012), p. 204310.

[75] G. Capano et al. "A Quantum Dynamics Study of the Ultrafast Relaxation in a Prototypical Cu(I)–Phenanthroline". In: *The Journal of Physical Chemistry A* 118.42 (2014), pp. 9861–9869.

[76] T. J. Penfold and J. Gibson. "The Role of Vibronic Coupling for Intersystem Crossing and Reverse Intersystem Crossing Rates in TADF Molecules". In: *Highly Efficient OLEDs*. John Wiley Sons, Ltd, 2018. Chap. 9, pp. 297–330. ISBN: 9783527691722.

[77] P. Hohenberg and W. Kohn. "Inhomogeneous Electron Gas". In: *Phys. Rev.* 136 (3B Nov. 1964), B864–B871.

[78] W. Kohn and L. J. Sham. "Self-Consistent Equations Including Exchange and Correlation Effects". In: *Phys. Rev.* 140 (4A Nov. 1965), A1133–A1138.

[79] Erich Runge and E. K. U. Gross. "Density-Functional Theory for Time-Dependent Systems". In: *Phys. Rev. Lett.* 52 (12 Mar. 1984), pp. 997–1000.

[80] W. Kohn. "Nobel Lecture: Electronic structure of matter—wave functions and density functionals". In: *Rev. Mod. Phys.* 71 (5 Oct. 1999), pp. 1253–1266.

[81] A. N. Rubtsov, M. I. Katsnelson, and A. I. Lichtenstein. "Dual fermion approach to nonlocal correlations in the Hubbard model". In: *Phys. Rev. B* 77 (3 Jan. 2008), p. 033101.

[82] W. Kohn and N. Rostoker. "Solution of the Schrödinger Equation in Periodic Lattices with an Application to Metallic Lithium". In: *Phys. Rev.* 94 (5 June 1954), pp. 1111–1120.

[83] J. P. Perdew and K. Schmidt. "Jacob's ladder of density functional approximations for the exchange-correlation energy". In: *AIP Conference Proceedings* 577.1 (2001), pp. 1–20.

[84] J. P. Perdew, K. Burke, and M. Ernzerhof. "Generalized Gradient Approximation Made Simple." In: *Physical Review Letters* 77 (1996), pp. 3865–3868.

[85] A D Becke. "Density-functional exchange-energy approximation with correct asymptotic behavior". In: *Phys. Rev. A* 38.6 (1988), pp. 3098–3100.

[86] C. Lee, W. Yang, and R. G. Parr. "Development of the Colle-Salvetti correlation-energy formula into a functional of the electron density". In: *Phys. Rev. B* 37.2 (1988), pp. 785–789.

[87] A. Dreuw, J. L. Weisman, and M. Head-Gordon. "Long-range charge-transfer excited states in time-dependent density functional theory require non-local exchange". In: *The Journal of Chemical Physics* 119 (2003), pp. 2943–2946.

[88] B. Miehlich et al. "Results obtained with the correlation energy density functionals of becke and Lee, Yang and Parr". In: *Chemical Physics Letters* 157.3 (1989), pp. 200–206.

[89] A. D. Becke. "Density-functional thermochemistry. I. The effect of the exchange-only gradient correction". In: *The Journal of Chemical Physics* 96.3 (1998), pp. 2155–2160.

[90] J. P. Perdew, M. Ernzerhof, and K. Burke. "Rationale for mixing exact exchange with density functional approximations". In: *The Journal of Chemical Physics* 105.22 (1998), pp. 9982–9985.

[91] Mark E. Casida. "Time-Dependent Density Functional Response Theory of Molecular Systems: Theory, Computational Methods, and Functionals". In: *Theoretical and Computational Chemistry* 4 (1996), pp. 391–439.

[92] Jamin Ku, Yves Lansac, and Yun Hee Jang. "Time-Dependent Density Functional Theory Study on Benzothiadiazole-Based Low-Band-Gap Fused-Ring Copolymers for Organic Solar Cell Applications". In: *The Journal of Physical Chemistry C* 115.43 (2011), pp. 21508–21516.

[93] M. E. CASIDA. "Time-Dependent Density Functional Response Theory for Molecules". In: *Recent Advances in Density Functional Methods*, pp. 155–192.

[94] S. Hirata and M. Gordon. "Time-dependent density functional theory within the Tamm-Dancoff approximation". In: *Chemical Physics Letters* 314.3-4 (1999), pp. 291–299.

[95] R. A. Marcus. "Chemical and Electrochemical Electron-Transfer Theory". In: *Annu. Rev. Phys. Chem.* 15 (1965), pp. 155–196. DOI: 10.1146/annurev.pc.15.100164.001103.

[96] R. A. Marcus. "On the Theory of Oxidation-Reduction Reactions Involving Electron Transfer. I". In: *J. Chem. Phys.* 24 (1956), pp. 966–978. DOI: 10.1063/1.1742723.

[97] H. Grubmüller et al. "Generalized Verlet Algorithm for Efficient Molecular Dynamics Simulations with Long-range Interactions". In: *Molecular Simulation* 6.1-3 (1991), pp. 121–142.

[98] David Van Der Spoel et al. "GROMACS: Fast, flexible, and free". In: *Journal of Computational Chemistry* 26.16 (2005), pp. 1701–1718.

[99] Arieh Warshel and Michael Levitt. "Theoretical studies of enzymic reactions: dielectric, electrostatic and steric stabilization of the carbonium ion in the reaction of lysozyme." In: *Journal of molecular biology* 103 2 (1976), pp. 227–49.

[100] Marc W. van der Kamp and Adrian J. Mulholland. "Combined Quantum Mechanics/Molecular Mechanics (QM/MM) Methods in Computational Enzymology". In: *Biochemistry* 52.16 (2013), pp. 2708–2728.

[101] P. Bała et al. "Quantum-Classical Molecular Dynamics Simulations of Proton Transfer Processes in Molecular Complexes and in Enzymes". In: *The Journal of Physical Chemistry* 100.7 (1996), pp. 2535–2545.

[102] A. Endo et al. "Thermally Activated Delayed Fluorescence from Sn4+-Porphyrin Complexes and Their Application to Organic Light Emitting Diodes - A Novel Mechanism for Electroluminescence". In: *Adv. Mater.* 21 (2009), p. 4802.

[103] H. Nakanotani et al. "Light Amplification in Molecules Exhibiting Thermally Activated Delayed Fluorescence". In: *Adv. Opt. Mater.* 5 (2017), p. 1700051.

[104] A. J. Kuehne and M. C. Gather. "Organic Lasers: Recent Developments on Materials, Device Geometries, and Fabrication Techniques". In: *Chem. Rev.* 116 (2016), p. 12823.

[105] W. Chang et al. "Spin-Dependent Charge Transfer State Design Rules in Organic Photovoltaics". In: *Nat. Commun.* 6 (2015), p. 6415.

[106] D. M. Freeman et al. "Synthesis and Exciton Dynamics of Donor-Orthogonal Acceptor Conjugated Polymers: Reducing the Singlet–Triplet Energy Gap". In: *J. Am. Chem. Soc.* 139 (2017), p. 11073.

[107] M. Y. Wong and E. Zysman-Colman. "Purely Organic Thermally Activated Delayed Fluorescence Materials for Organic Light-Emitting Diodes". In: *Adv. Mater.* 29 (2017), p. 1605444.

[108] T. Penfold, F. Dias, and A. Monkman. "The Theory of Thermally Activated Delayed Fluorescence for Organic Light Emitting Diodes". In: *Chem. Commun.* 54 (2018), p. 3926.

[109] T. J. Penfold. "On Predicting the Excited-State Properties of Thermally Activated Delayed Fluorescence Emitters". In: *J. Phys. Chem. C* 119 (2015), p. 13535.

[110] Y Hartmut. *Triplet Emitters for OLED Application—Mechanisms of Exciton Trapping and Control of Emission Properties*. Vol. 241. Nov. 2004, pp. 1–26.

[111] T. Hatakeyama et al. "Ultrapure Blue Thermally Activated Delayed Fluorescence Molecules: Efficient HOMO–LUMO Separation by the Multiple Resonance Effect". In: *Adv. Mater.* 28 (2016), p. 2777.

[112] Dirk Veldman, Stefan C. J. Meskers, and René A. J. Janssen. "The energy of charge-transfer states in electron donor-acceptor blends: Insight into the energy losses in organic solar cells". In: *Advanced Functional Materials* 19.13 (2009), pp. 1939–1948.

[113] Wei Zeng, Sumit Mukherjee, and Sankha Chatterjee. "Influence of molecular rigidity on the intersystem crossing rate in organic phosphorescent materials". In: *The Journal of Physical Chemistry C* 123.13 (2019), pp. 7825–7834.

[114] T. Northey and T. Penfold. "The Intersystem Crossing Mechanism of an Ultrapure Blue Organoboron Emitter". In: *Org. Electron.* 59 (2018), p. 45.

[115] T. Penfold et al. "Spin-vibronic Mechanism for Intersystem Crossing". In: *Chem. Rev.* 118 (2018), p. 6975.

[116] J. Gibson, A. Monkman, and T. Penfold. "The Importance of Vibronic Coupling for Efficient Reverse Intersystem Crossing in TADF Molecules". In: *ChemPhysChem* 17 (2016), p. 2956.

[117] J. Gibson and T. Penfold. "Nonadiabatic Coupling Reduces the Activation Energy in Thermally Activated Delayed Fluorescence". In: *Phys. Chem. Chem. Phys.* 19 (2017), p. 8428.

[118] S. Hirata and M. Head-Gordon. "Time-Dependent Density Functional Theory within the Tamm-Dancoff Approximation". In: *Chem. Phys. Lett.* 314 (1999), p. 291.

[119] J. P. Perdew, K. Burke, and M. Ernzerhof. "Generalized Gradient Approximation Made Simple". In: *Phys. Rev. Lett.* 77 (1996), p. 3865.

[120] C. Adamo and V. Barone. "Toward Reliable Density Functional Methods Without Adjustable Parameters: The PBE0 Model". In: *J. Chem. Phys.* 110 (1999), p. 6158.

[121] Y. Shao et al. "Advances in Molecular Quantum Chemistry Contained in the Q-Chem 4 Program Package". In: *Mol. Phys.* 113 (2015), p. 184.

[122] F. Weigend. "Accurate Coulomb-Fitting Basis Sets for H to Rn". In: *Phys. Chem. Chem. Phys.* 8 (2006), p. 1057.

[123] J. Tomasi, B. Mennucci, and R. Cammi. "Quantum Mechanical Continuum Solvation Models". In: *Chem. Rev.* 105 (2005), p. 2999.

[124] R. Cammi et al. "Electronic Excitation Energies of Molecules in Solution: State Specific and Linear Response Methods for Nonequilibrium Continuum Solvation Models". In: *J. Chem. Phys.* 122 (2005), p. 104513.

[125] I. S. Ufimtsev and T. J. Martínez. "Quantum Chemistry on Graphical Processing Units. 1. Strategies for Two-Electron Integral Evaluation". In: *J. Chem. Theory Comput.* 4 (2008), p. 222.

[126] I. S. Ufimtsev and T. J. Martínez. "Quantum Chemistry on Graphical Processing Units. 3. Analytical Energy Gradients, Geometry Optimization, and First Principles Molecular Dynamics". In: *J. Chem. Theory Comput.* 5 (2009), p. 2619.

[127] G. Capano et al. "A Quantum Dynamics Study of the Ultrafast Relaxation in a Prototypical Cu(I)–Phenanthroline". In: *J. Phys. Chem. A* 118 (2014), p. 9861.

[128] J. Eng et al. "Spin-Vibronic Quantum Dynamics for Ultrafast Excited-State Processes". In: *Acc. Chem. Res.* 48 (2015), p. 809.

[129] H.-D. Meyer, F. Gatti, and Eds. Worth G. A. "High Dimensional Quantum Dynamics: Basic Theory, Extensions, and Applications of the MCTDH Method". In: *Wiley-VCH, Weinheim, Germany* 1 (2008).

[130] H. Köuppel, W. Domcke, and L. S. Cederbaum. "Multimode Molecular Dynamics Beyond the Born-Oppenheimer Approximation". In: *Adv. Chem. Phys.* 57 (2007), p. 59.

[131] T. Penfold et al. "Quantum Dynamics Study of the Competing Ultrafast Intersystem Crossing and Internal Conversion in the "Channel 3" Region of Benzene". In: *J. Chem. Phys.* 137 (2012), p. 204310.

[132] H.D. Meyer, U. Manthe, and L. S. Cederbaum. "The Multi-Configurational Time-Dependent Hartree Approach". In: *Chem. Phys. Lett.* 165 (1990), p. 73.

[133] M. H. Beck et al. "The Multiconfiguration Time-Dependent Hartree Method: A Highly Efficient Algorithm for Propagating Wavepackets". In: *Phys. Rep.* 324 (2000), p. 1.

[134] T. Northey, J. Stacey, and T. Penfold. "The Role of Solid State Solvation on the Charge Transfer State of a Thermally Activated Delayed Fluorescence Emitter". In: *J. Mater. Chem. C* 5 (2017), p. 11001.

[135] K. C. Tang et al. "Fine Tuning the Energetics of Excited-State Intramolecular Proton Transfer (ESIPT): White Light Generation in a Single ESIPT System". In: *J. Am. Chem. Soc.* 133 (2011), p. 17738.

[136] R. M. Tarkka, X. Zhang, and S. A. Jenekhe. "Electrically Generated Intramolecular Proton Transfer: Electroluminescence and Stimulated Emission from Polymers". In: *J. Am. Chem. Soc.* 118 (1996), p. 9438.

[137] H. Noda, H. Nakanotani, and C. Adachi. "Highly Efficient Thermally Activated Delayed Fluorescence with Slow Reverse Intersystem Crossing". In: *Chem. Lett.* 48 (2019), p. 126.

[138] P. Dos-Santos. *The Study of Thermally Activated Delayed Fluorescence Mechanism in Mono and Bimolecular Systems*. Durham University: Doctoral Thesis, 2018.

[139] A. Mordzinski and K. Grellmann. "Excited-State Proton-Transfer Reactions in 2-(2'-hydroxyphenyl) benzoxazole. Role of Triplet States". In: *J. Phys. Chem.* 90 (1986), p. 5503.

[140] R. Huang et al. "The Influence of Molecular Conformation on the Photophysics of Organic Room Temperature Phosphorescent Luminophores". In: *J. Mater. Chem. C* 6 (2018), p. 9238.

[141] C. Ganzorig and M. Fujihira. "A Possible Mechanism for Enhanced Electrofluorescence Emission Through Triplet–Triplet Annihilation in Organic Electroluminescent Devices". In: *Appl. Phys. Lett.* 81 (2002), p. 3137.

[142] P. Chen et al. "Delayed Fluorescence in a Solution-Processable Pure Red Molecular Organic Emitter Based on Dithienylbenzothiadiazole: A Joint Optical, Electroluminescence, and Magnetoelectroluminescence Study". In: *ACS Appl. Mater. Interfaces* 7 (2015), p. 2972.

[143] Y. Cao, J. Eng, and T. J. Penfold. "Excited State Intramolecular Proton Transfer Dynamics for Triplet Harvesting in Organic Molecules". In: *The Journal of Physical Chemistry A* 123.13 (2019), pp. 2640–2649.

[144] Y. Long et al. "Excited State Dynamics of Thermally Activated Delayed Fluorescence from an Excited State Intramolecular Proton Transfer System". In: *The journal of physical chemistry letters* 11.9 (2020), pp. 3305–3312.

[145] Hartmut Yersin. "Triplet Emitters for Organic Light-Emitting Diodes: Molecular-Level Tuning of the Triplet-Triplet Annihilation". In: *ChemPhysChem* 15.19 (2014), pp. 4008–4026.

[146] Ye Tao et al. "TADF: A tip for designing efficient organic light-emitting materials". In: *Chemical Communications* 50.27 (2014), pp. 3495–3498.

[147] R. W. Gurney and E. U. Condon. "Quantum Mechanics and Radioactive Disintegration". In: *Phys. Rev.* 33 (Feb. 1929), pp. 127–140.

[148] H.-D. Meyer, U. Manthe, and L. S. Cederbaum. "The Multi-Configurational Time-Dependent Hartree Approach". In: *Chemical Physics Letter* 165 (1990), pp. 73–78.

[149] M. H. Beck et al. "The multiconfiguration time-dependent Hartree method: A highly efficient algorithm for propagating wavepackets." In: *Phys. Rep.* 324 (2000), pp. 1–105.

[150] H. Meyer and G. A. Worth. "Quantum molecular dynamics: propagating wavepackets and density operators using the multiconfiguration time-dependent Hartree method". In: *Theoretical Chemistry Accounts* 109.5 (2003), pp. 251–267.

[151] T. Hwang and C. Wang. "On multiple solutions for Berman's problem". In: *Proceedings of the Royal Society of Edinburgh: Section A Mathematics* 121.3-4 (1992), pp. 219–230.

[152] J. Stephen Binkley, John A. Pople, and Warren J. Hehre. "Self-consistent molecular orbital methods. 21. Small split-valence basis sets for first-row elements". In: *Journal of the American Chemical Society* 102.3 (1980), pp. 939–947.

[153] Mark S. Gordon et al. "Self-consistent molecular-orbital methods. 22. Small split-valence basis sets for second-row elements". In: *Journal of the American Chemical Society* 104.10 (1982), pp. 2797–2803.

[154] W. J. Pietro et al. "Self-consistent molecular orbital methods. 24. Supplemented small split-valence basis sets for second-row elements". In: *Journal of the American Chemical Society* 104.19 (1982), pp. 5039–5048.

[155] K. D. Dobbs and W. J. Hehre. "Molecular orbital theory of the properties of inorganic and organometallic compounds 4. Extended basis sets for third-and fourth-row, main-group elements". In: *Journal of Computational Chemistry* 7.3 (1986), pp. 359–378.

[156] K. D. Dobbs and W. J. Hehre. "Molecular orbital theory of the properties of inorganic and organometallic compounds 5. Extended basis sets for first-row transition metals". In: *Journal of Computational Chemistry* 8.6 (1987), pp. 861–879.

[157] K. D. Dobbs and W. J. Hehre. "Molecular orbital theory of the properties of inorganic and organometallic compounds. 6. Extended basis sets for second-row transition metals". In: *Journal of Computational Chemistry* 8.6 (1987), pp. 880–893.

[158] H. Suzuki and S. Hoshino. "Effects of doping dyes on the electroluminescent characteristics of multilayer organic light-emitting diodes". In: *Journal of Applied Physics* 79.11 (1996), pp. 8816–8822.

[159] F. Nüesch et al. "Doping-Induced Charge Trapping in Organic Light-Emitting Devices". In: *Advanced Functional Materials* 15.2 (2005), pp. 323–330.

[160] Th. Förster. "Zwischenmolekulare Energiewanderung und Fluoreszenz". In: *Annalen der Physik* 437.1-2 (1948), pp. 55–75.

[161] D. L. Dexter. "A Theory of Sensitized Luminescence in Solids". In: *The Journal of Chemical Physics* 21.5 (1953), pp. 836–850.

[162] M. A. Baldo and S. R. Forrest. "Transient analysis of organic electrophosphorescence: I. Transient analysis of triplet energy transfer". In: *Phys. Rev. B* 62 (16 2000), pp. 10958–10966.

[163] E. Francisco, L. Seijo, and L. Pueyo. "The maximum overlap method: A general and efficient scheme for reducing basis sets. Application to the generation of approximate AO's for the 3d transition metal atoms and ions". In: *Journal of Solid State Chemistry* 63.3 (1986), pp. 391–400.

[164] F. Weigend and R. Ahlrichs. "Balanced basis sets of split valence, triple zeta valence and quadruple zeta valence quality for H to Rn: Design and assessment of accuracy". In: *Phys. Chem. Chem. Phys.* 7 (18 2005), pp. 3297–3305.

[165] S. Miertuš, E. Scrocco, and J. Tomasi. "Electrostatic interaction of a solute with a continuum. A direct utilizaion of AB initio molecular potentials for the prevision of solvent effects". In: *Chemical Physics* 55.1 (1981), pp. 117–129.

[166] J. Miertus S. an dTomasi. "Approximate evaluations of the electrostatic free energy and internal energy changes in solution processes". In: *Chemical Physics* 65.2 (1982), pp. 239–245.

[167] J. L. Pascual-ahuir, E. Silla, and I. Tuñon. "GEPOL: An improved description of molecular surfaces. III. A new algorithm for the computation of a solvent-excluding surface". In: *Journal of Computational Chemistry* 15.10 (1994), pp. 1127–1138.

[168] Y. Shao, Z. Gan, and et al. "Advances in molecular quantum chemistry contained in the Q-Chem 4 program package". In: *Molecular Physics* 113.2 (2015), pp. 184–215.

[169] D.A. Case and et al. "Amber 14". In: *University of California, San Francisco* 0.0 (2014), p. 0.

[170] Breneman M. and Wiberg B. "Determining atom-centered monopoles from molecular electrostatic potentials. The need for high sampling density in formamide conformational analysis". In: *Journal of Computational Chemistry* 11.3 (1990), pp. 361–373.

[171] Jonas Sjöqvist et al. "QM/MM-MD simulations of conjugated polyelectrolytes: a study of luminescent conjugated oligothiophenes for use as biophysical probes". In: *Journal of Physical Chemistry Part A: Molecules, Spectroscopy, Kinetics, Environment and General Theory* 118.19 (2014), pp. 3419–3428.

[172] R. A. Marcus. "Electron transfer reactions in chemistry. Theory and experiment". In: *Rev. Mod. Phys.* 65 (3 1993), pp. 599–610.

[173] O. López-Estrada et al. "Reassessment of the Four-Point Approach to the Electron-Transfer Marcus–Hush Theory". In: *ACS Omega* 3.2 (2018), pp. 2130–2140.

[174] O. Braem et al. "A femtosecond fluorescence study of vibrational relaxation and cooling dynamics of UV dyes". In: *Physical Chemistry Chemical Physics* 14.10 (2012), pp. 3513–3519.

[175] M. Liu et al. "Blue thermally activated delayed fluorescence materials based on bis(phenylsulfonyl)benzene derivatives". In: *Chem. Commun.* 51 (91 2015), pp. 16353–16356.

[176] T. Zhu and T. Van Voorhis. "Unraveling the Fate of Host Excitons in Host–Guest Phosphorescent Organic Light-Emitting Diodes". In: *The Journal of Physical Chemistry C* 123.16 (2019), pp. 10311–10318.